DISSERTATION

Processing and Visualization of Peripheral CT-Angiography Datasets

ausgeführt zum Zwecke der Erlagung des akadamischen Grades
eines Doktors der technischen Wissenschaften

unter der Leitung von
Univ.Doz. Dipl.-Ing. Dr.techn. Miloš Šrámek
Institut für Computergraphik und Algorithmen

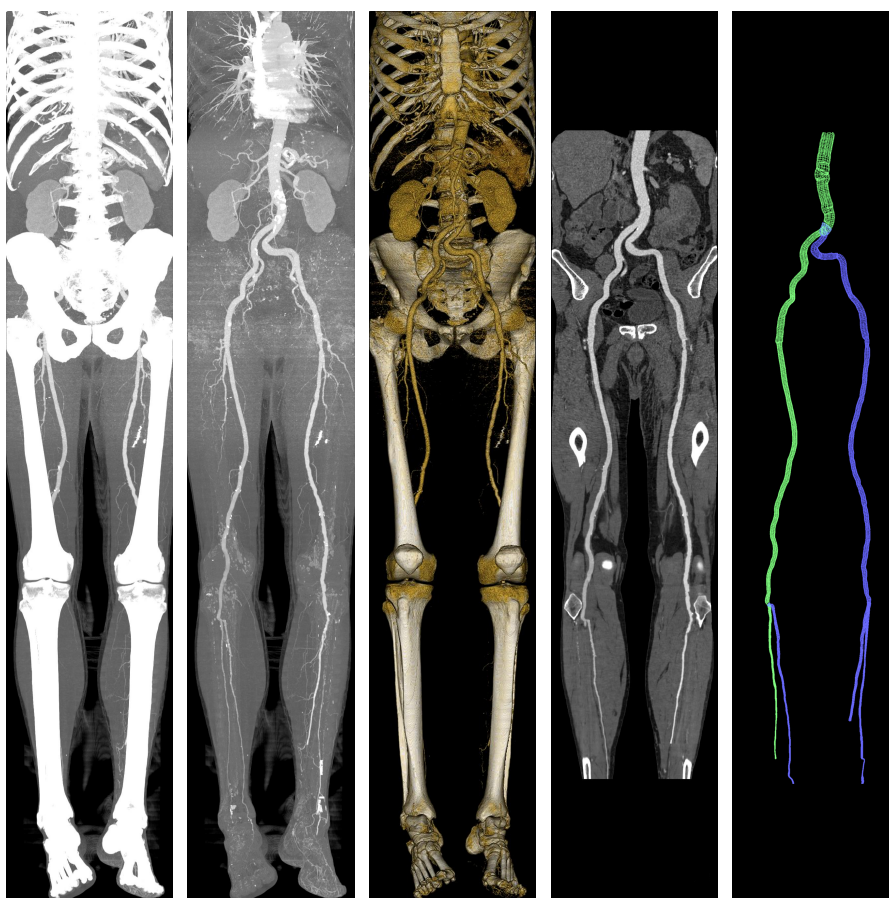eingereicht an der Technischen Universität Wien, Fakultät für Informatik, durch

Dipl.-Ing. Matúš Straka
Matr. Nr. 0227533
Pri Kríži 3
841 02 Bratislava, Slowakei
geboren am 18. März 1978, Bratislava, Slowakei

Wien, im Juli 2006 ....

PROCESSING AND VISUALIZATION OF PERIPHERAL CT-ANGIOGRAPHY DATASETS

PhD Thesis

Matúš Straka

Kommission für Wissenschaftliche Visualisierung
Österreichische Akademie der Wissenschaften
matus.straka@oeaw.ac.at

Abstract

In this thesis, individual steps of a pipeline for processing of the peripheral Computed Tomography Angiography (CTA) datasets are addressed. The peripheral CTA datasets are volumetric datasets representing pathologies in vascularity of the lower extremities in the human body. These pathologies result from various atherosclerotic diseases as e.g. the Peripheral Arterial Occlusive Disease (PAOD) and their early and precise diagnostics significantly contributes to planning of a later interventional radiology treatment.

The diagnostics is based on visualization of the imaged vascular tree, where individual pathologic changes, as plaque, calcifications, stenoses of the vessel lumen and occluded parts of the vessels are visible. CTA has evolved within the recent years into a robust, accurate and cost effective imaging technique for patients with both coronary and arterial diseases. As a result of the CTA scanning, a set of 1200–2000 transverse slices is acquired, depicting vessels enhanced by means of an intravenously injected contrast medium. The number of slices is high and therefore their manual examination is laborious and lengthy. As a remedy, post-processing methods were developed to allow faster and more intuitive visualization of the imaged vascularity. However, simple visualization by means of the traditional techniques as maximum-intensity projection (MIP) or direct volume rendering (DVR) is hampered due to the presence of bones in the dataset, which occlude the vessels. Therefore, a sequence of operations—the processing pipeline—is needed, leading to generation of clinically relevant images which depict unobstructed vessels.

In the first step of the pipeline the dataset is segmented and the tissues are classified, to allow subsequent vessel identification and bone removal. This is a complex task because of high density and spatial variability of the tissues. Traditional image processing techniques do not deliver acceptable results and therefore in the thesis we present new approaches that introduce additional 'anatomic' information into the segmentation and classification process. We propose a probabilistic atlas which enables modeling of spatial and density distributions of vessel and bone tissues in datasets, to allow their improved classification. In the atlas construction the non-rigid thin-plate spline warping and registration of the datasets are applied, to address the high anatomic variability among the patients. The concept of the atlas is further extended by means of the watershed transform, to further improve precision of the registration procedure. Alternatively, we propose and evaluate a technique for vessel enhancement based on Hessian filtering to allow detection and recognition of vessel structures without operator supervision.

In the second step a geometric model of the vessel tree is constructed to derive information about the vessel centerlines. Here, an already available algorithm based on the so-called vessel-tracking, implemented by means of optimal path searching, is exploited with improvements to make the geometric model more precise.

The third step of the processing pipeline—visualization—requires this model, since its results can be significantly influenced by a potential imperfections, bringing in clinically misleading images. To address limitations of the vessel visualization by means of the existing techniques as MIP, CPR or DVR we propose their gen-

eralization in form of a focus & context-based concept called VesselGlyph. VesselGlyph enables to combine intuitively and systematically various visualization techniques to single a image to allow better, more comprehensive and unoccluded view of vessels for the diagnostic purposes.

To support the design and development of the proposed segmentation, modeling and visualization algorithms and to enable their application in the clinical environment, we implemented a set of tools grouped in the AngioVis ToolBox software. Within this application, individual steps of the processing pipeline are accomplished. The toolbox is complemented with additional utilities constituting together a fully-functional medical workstation software which is regularly used to process patient data on a daily basis in the clinical environment.

Kurzfassung

In dieser Arbeit werden die einzelnen Schritte der Bearbeitung von Datenssätzen, die mittels Computer To-mography Angiography (CTA) gewonnen wurden, vorgestellt. Periphäre CTA-Datensätze sind volumetrische Datensätze, die pathologische Veränderungen der Blutgefäße der unteren Extremitäten des menschlichen Körpers darstellen. Diese Veränderungen sind das Ergebnis verschiedener atherosklerotischer Krankheiten wie z.B. der Peripheral Arterial Occlusive Disease (PAOD) und ihre frühe und genaue Diagnose trägt wesentlich zur Planung einer späteren interventionellen radiologischen Behandlung.

Die Diagnose stützt sich auf die Visualisierung des abgebildeten Gefäßbaumes, wo die individuellen pathol-ogischen Veränderungen, solche als Plaque, Verkalkungen, Stenosen des Gefäßdurchgangs und Verstopfungen desselben sichtbar werden. CTA entwickelte sich über die letzten Jahre zu einem robusten, genauen, kosten-effizienten Abbildungsverfahren für Patienten mit sowohl coronaren als auch arteriellen Erkrankungen. Als Folge der CTA-Prozedur entsteht ein Satz von 1200–2000 transversalen Schnittbildern, die die Blutgefäße mit-tels eines intravenös verabreichten Kontrastmittels hervorheben. Die Anzahl der erzeugten Schnittbilder ist sehr hoch und infolgedessen ihre manuelle Untersuchung müheselig und zeitintensiv. Deswegen wurden Nachbear-beitungsmethoden zur schnelleren und intuitiveren Darstellung der abgebildeten Gefäße entwickelt. Einfache Visualisierungen mittels traditionellen Techniken wie Maximum-Intensity Projection (MIP) oder Direct Vol-ume Rendering (DVR) sind jedoch wegen des Vorhandenseins von Knochen im Datensatz, welche die Gefäße verdecken, nicht zielführend. Deswegen ist eine Folge von Operationen, die Bearbeitungspipeline, die zur Erzeugung von klinisch-relevanten Bildern mit unverdeckten Gefäßen führt, notwendig.

Im ersten Schritt der Pipeline wird der Datensatz segmentiert und die Gewebearten darin klassifiziert um eine spätere Gefäßidentifikation und Knochenentfernung zu erlauben. Wegen der hohen Dichte und der räum-lichen Variabilität der Gewebearten ist das eine komplexe Aufgabe. Traditionelle Bildverarbeitungstechniken liefern keine brauchbaren Ergebnisse deswegen stellen wir in dieser Arbeit neue Zugänge, die zusätzliche, 'anatomische' Information in den Segmentierungs- und Klassifizierungsprozeßeinbringen, vor. Wir schlagen einen probabilistischen Atlas vor, der das Modellieren der räumlichen und der Dichteverteilung in einem Daten-satz erlaubt um ihre bessere Klassifizierung zu ermöglichen. Beim Atlasaufbau werden die non-rigid thin-plate spline Warping und die Registrierung der Datensätze angewendet, um der hohen anatomischen Variabilität zwischen Patienten Rechnung zu tragen. Das Atlaskonzept wird weiter durch die Watershed Transform um die Genauigkeit der Registrierungsprozedur zu erhöhen erweitert. Als Alternative schlagen wir vor und evaluieren eine Technik zur Gefäßhervorhebung, die auf Hessscher Filterung basiert, um die Aufdeckung und Erkennung der Gefäßstrukturen ohne Operatorüberwachung zu erlauben.

Im zweiten Schritt wird ein geometrisches Modell des Gefäßbaums konstruiert, der es erlaubt Informationen über die Zentrallinien der Gefäße abzuleiten. Hierzu wird ein schon vorhandener Algorithmus verwendet, der auf dem sogenannten Vessel-Tracking aufbaut, das mittels optimaler Pfadsuche mit Verbesserungen um das

geometrische Modell genauer zu machen implementiert ist.

Der dritte Schritt der Bearbeitungspipeline, die Visualisierung, verlangt ein genaues Modell, da ihre Ergebnisse wesentlich durch ein potenziell ungenaues Modell beeinflußt werden können, was zu klinisch irreführenden Bildern führt. Um die Unzulänglichkeiten der Gefäßvisualisierung mittels herkömmlichen Techniken als MIP, CPR oder DVR zu beseitigen schlagen wir ihre Verallgemeinerung als Focus & Context-Konzept, das wir VesselGlyph nennen, vor. VesselGlyph erlaubt verschiedene Visualisierungstechniken in einem Bild intuitiv und systematisch zu kombinieren um bessere, umfassendere und unverdeckte Gefäßansichten für diagnostischen Zwecke zu erzeugen.

Um das Design und die Entwicklung der vorgeschlagenen Segmentierungs-, Modellierungs- und Visualisierungsalgorithmen zu fördern und ihre Anwendung in klinischer Umgebung zu ermöglichen haben wir einen Satz von Werkzeugen um die AngioVis-ToolBox entwickelt. In dieser Anwendung werden die einzelnen Schritte der Bearbeitungspipeline realisiert. Die Toolbox wird mit zusätzlichen Hilfsprogrammen vervollständigt die zusammen eine vollfunktionsfähige medizinische Arbeitsstationssoftware ergeben die regelmäßig um Patientendaten in einer klinischen Umgebung zu bearbeiten eingesetzt wird.

Acknowledgement

Contents

List of Figures

List of Tables

Preface

In recent years, three-dimensional (3D) visualization of human body in medicine has became a standard diagnostic procedure, mainly in radiology and radiology-supported surgery. This has been made possible due to huge development in the area of 3D (volumetric) imaging techniques, exemplified by computed tomography (CT) and magnetic resonance imaging that allow insight in human body without actually invading it. These imaging techniques have brought—as analytic tools—invaluable clinical advantage.

Patients in developed countries are—due to the lifestyle—affected by civilization diseases that lower the quality of life and contribute to increased mortality. Unhealthy habits as heavy smoking, excessive drinking of alcohol, diet containing too much of fats, carbohydrates and salt, insufficient exercise, stress or innate disabilities as diabetes cause pathologic changes within a cardio-vascular system, especially in higher age. Vascular diseases, as e.g. atherosclerosis are actually the most frequent cause of death in these countries. In their earlier stages, these diseases bring in severe problems like pain in limbs or limited movement of the patients. Later, they are reasons for not healing wounds or infarctions. Early diagnostics and proper clinical intervention—based on visualization and evaluation of imaged vessel tree—can significantly contribute to therapy and thus improve life quality of the patients.

Contemporary medicine is developing pharmaceutical and invasive solutions for atherosclerotic complications and 3D imaging is inseparable part of it. While the 3D scanning concept has opened new diagnostic and treatment possibilities, it has also brought many challenges, mainly in image processing and visualization fields. The general problem is an easy and effective interpretation of the acquired 3D data, because humans are used to interpret only two-dimensional (2D) projections, i.e. information that can be viewed on a plane. The reason for this is probably the fact that the currently available visualization screens, as CRT or LCD monitors, overhead projectors and paper or film printers are all 2D modalities. Therefore, 3D datasets are traditionally post-processed into 2D images for easier interpretation and clinical diagnostic purposes. A post-processing or projection of the acquired 3D data to 2D images that leads to a proper, simple, intuitive, instructive and easily-interpretable display of clinically relevant information is a huge challenge in 3D medical visualization.

Within this thesis we address the problem of processing and visualization of peripheral CT-Angiography (CTA) datasets aimed on diagnostics of atherosclerotic diseases in lower extremities. These datasets represent vessels in patients' lower limbs and their proper visualization is a prerequisite for later interventional-radiology treatments. In this text, which summarizes a four-year-long joint research in field of Computer Graphics and Interventional Radiology, we present the achieved results of novel post-processing and visualization approaches, implemented in a set of dedicated software tools, aimed on their evaluation in a clinical environment.

The ever-increasing quality and resolution of medical imaging modalities favoured by advances in computer hardware and imaging industry prevents any solution to be considered as finished and complete. However, we hope that our work brings insight in selected problems and will be important and applicable also in future.

Chapter 1

Motivation

1.1 Vascular Diseases, Diagnostics and Treatment

Atherosclerosis is a multifactorial chronic inflammatory, degenerative process of large- and medium-sized arteries characterized pathologically by the presence of atherosclerotic plaque. The clinical signs and symptoms of atherosclerosis are generally summarized under the term cardio-vascular disease. Typical cardiovascular diseases are coronary artery disease (angina and myocardial infarction), cerebrovascular disease (stroke), and peripheral arterial occlusive disease. Cardio-vascular diseases are the leading cause of mortality in developed countries. Atherosclerosis [1] manifests itself as pathologic changes of the intimal layer of the arterial wall (see Fig. 1.1a) and is often referred to as 'hardening' of the vessels. This hardening is caused by a formation of atherosclerotic plaque. Pathologically, the atheromatous plaque may consist of three distinct components (refer to Fig. 1.2):

- *A lipid plaque* is the buildup of fatty deposits within the wall of a blood vessel. This focal accumulation of soft material, composed of macrophages, foam cells and sometimes with underlying areas of cholesterol crystals narrows the lumen of the artery. This narrowing of the vessel is called *stenosis* (Fig. 1.1b). During time periods this changes to:

- *A fibrous plaque*—a deposition of tough, rigid collagen inside the vessel wall and around the soft plaque. A fibro-fatty plaque consists of a lipid core and a fibrous cap. This increases the stiffness and decreases
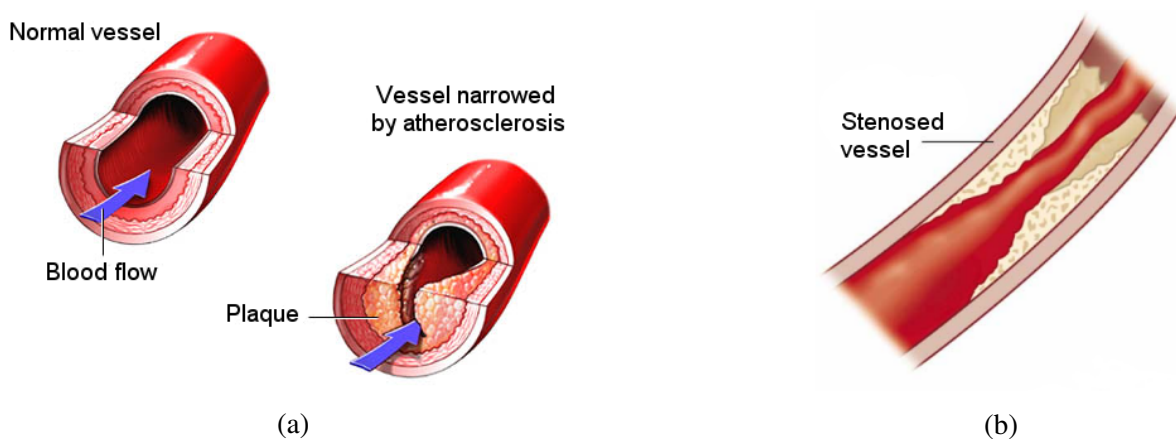
Figure 1.1: *(a) Atherosclerosis. (b) Stenosis - narrowing of the vessel lumen.*

<div align="center">(a)   (b)</div>
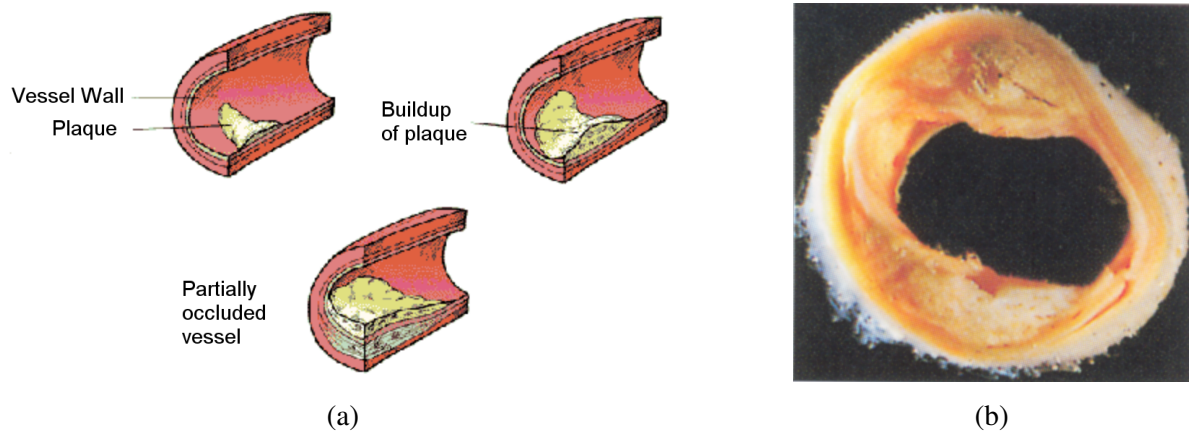
Figure 1.2: *(a) Development of atherosclerotic plaque in vessels. (b) Photograph of a vessel with plaque deposits.*

the elasticity of the artery wall. Later, portions of the plaque of the whole area may transform into:

- *A calcified plaque* characterized by mineral deposition or sometimes even an ossification (formation of bony tissue) that occurs in the thickest parts of the sclerosed vessel wall.

- Depending on the size of an atherosclerotic plaque relative to the vessel lumen, plaque can lead either to luminal narrowing (stenosis) of variable degree or if plaque fills the whole flow lumen, it causes a complete blockage the blood flow in the vessel, what is called *occlusion*.

The presence of hemodynamically significant (approximately 50% diameter) stenoses caused by atherosclerotic plaque results in diminished blood flow to the dependent organs and tissue. At first, diminished blood flow may only be noticeable during increased demand, e.g. during exercising. This is known as angina pectoris in the case of coronary artery disease, and as 'intermittent claudication' when the lower extremity arteries are affected. *Peripheral Arterial Occlusive Disease* (PAOD) is the manifestation of atherosclerosis in the arterial system of lower extremities of the human body ([1], see Fig. 1.3). In the lower limbs, the diminished or completely blocked blood flow results first in the typical symptom of discomfort and pain when walking, which immediately subsides when stopping to walk. This symptom is called 'intermittent claudication' [2]. In general, intermittent claudication has a benign prognosis, and only a small proportion of patients progress to the next stage of PAOD. If the blood flow to the lower extremities is decreased to such an extent that the baseline metabolic demand of lower extremity is threatened, this stage of PAOD is termed 'chronic limb threatening ischemia'. The clinical symptoms of this stage are rest pain (usually of the foot), loss of tissue in the limbs and non-healing wounds. Chronic limb threatening ischemia requires urgent treatment, because of the risk of necrosis and gangrene which requires amputation of the affected limb.

The treatment of PAOD depends on the clinical symptoms (intermittent claudication versus chronic limb threatening ischemia) and the extent and location of flow-limiting atherosclerotic lesions. Therapeutic measures always include reducing the known cardiovascular risk factors, such as hypertension, hyperlipidemia, diabetes, and dietary or smoking habits. The main specific treatment options for PAOD are:

- *Conservative treatment*—controlled exercise training supported by pharmacotherapy,

- *Surgical revascularization* is typically achieved by using a bypass-graft, which connects a healthy segment above a stenotic or occluded segment with a non diseased segment distal to the diseased segment. A bypass graft can be made of a patient's own veins (vein-graft) or synthetic materials (e.g. PTFE-graft),

- *Percutaneous Transluminal Angioplasty (PTA)*—in which a catheter with a small folded balloon is inserted in the vessel. When the catheter is in place, the balloon is hydraulically inflated with very high pressure and it compresses the atheromatous plaque and stretches the artery wall (Fig. 1.4). During this procedure, also expandable wire mesh tube—*a stent*—might be implanted to support the new stretched position of the artery from inside [2]. This technique is used on solitary lesions in large arteries, e.g. the iliac and the femoral arteries. Finally,

- *Amputation* might be needed if complete tissue necrosis and gangrene has developed to prevent septicemia.

The presence of PAOD is usually suggested by the patient's symptoms, and the diagnosis is generally established by clinical means (pulse palpation) and non-invasive diagnostic tests, such as blood pressure measurements (ankle-brachial artery pressure index). The severity of a patient's symptoms also determines if surgical or endovascular revascularization procedure should be contemplated. Once the clinical indication for revascularization has been established, further tests and accurate assessment of the pathologic changes is needed for therapeutic planning.

Planning of a revascularization procedure requires accurate mapping of the disease manifestations. In other words, to asses where the lesions are, what is their length, what is the actual lumen of the diseased vessel, whether the vessel is completely occluded, and if the lesions would be amenable to percutaneous treatment or if a surgical bypass grafting procedure is required. For all those treatment planning decisions a detailed assessment and visualization of the vasculature in patient's body is an absolute prerequisite. As described in Rofsky *et al.* [3] in planning of lower extremity intervention, it is necessary to characterize the inflow and the outflow from a lesion. If the inflow is diseased (because of proximal occlusive disease), a distal arterial reconstruction may be jeopardized. If the outflow is limited, the integrity of a vascular reconstruction might be compromised. Ideally, the arterial reconstruction is performed from an area of normal inflow to an area of normal outflow to by-pass a lesion or set of lesions. In planning treatment for patients with atherosclerotic occlusive arterial disease the most important distinctions are: *(a)* between high-grade stenoses (usually $> 50\%$ narrowing, including occlusions) and lesser grade stenoses (usually $< 50\%$ narrowing) and *(b)* between short- and long-segment occlusions. Those lesions with more than 50% narrowing of vessel are most often hemodynamically significant. Discrimination of the length of the diseased segment stratifies patients who are potentially amenable to a successfull angioplasty procedure ($\leq 10cm$ in length) from those who are less likely to benefit ($> 10cm$ in length). The length, type and site of disease influence the results of angioplasty. In general, the proximal (e.g. iliac artery) and shorter segment ($< 3cm$ in length) lesions yield the best results.

Such highly precise information can be delivered only by direct visualization of the vascularity. Therefore, vessel imaging has become an important part of radiology. Various techniques have been developed to display the vessels and their state, providing the necessary data for therapeutic decision making and treatment planning.

1.2   Vessel Visualization and History

Angiography or arteriography is a medical imaging technique in which an image is produced to visualize the inside (lumen) of blood filled structures, including arteries, veins and the heart chambers. Its name comes from the Greek words *angeion*, 'vessel', and *graphien*, 'to write or record'. An image of the blood vessels is called an angiograph, or more commonly, an angiogram [1]. As the arteries are located deeply in the body, imaging techniques are needed to display them if direct invasion in the body is undesirable.

Imaging of structures within the human body was not always available. It became possible first from the end of the 19th century. As the most important milestone can be considered the year 1895 when Röntgen [4] discovered the X-rays. This new imaging technique allowed visualization of body structures without the actual need to open the body. Right from the start of the X-rays era, cardiac and vascular structures have become a target of this new imaging technique Abrams [5]. As soon as in 1896 Morton [6] created a radiograph and in the same year Haschek with Lindenthal [7] made a first angiogram of a hand of a corpse (in Vienna, Austria), by injection of mercury sulfide. In 1903 Williams [8] published an extensive work about X-rays images of the human heart. A second milestone was the year 1906, when a first X-rays *in vivo* applicable contrast medium (barium sulfate) was introduced and a first contrast-medium filled image of the renal system (kidneys) was created by Völcker [9]. Later in 1924, radiographic imaging of blood vessels was produced for the first time (Brooks [10]). Images like Fig. 1.3b become available. In 1945, first visualization of coronary arteries was executed by Radner [11].

In 1972, computed tomography (CT) scanning was invented by Hounsfield and Cormack, bringing advanced medical imaging on the scene. Practically usable tomography without X-rays—the magnetic resonance imaging (MR, NMR or MRI)—was developed later, in year 1980 (Mattson and Simon [12]). In 1986, helical CT imaging appeared (first manufactured by Toshiba, Japan) what allowed scanning of entire volumes. Spiral CT had brought a renaissance for CT and lead the way to significant developments like CT-Angiography (CTA). First papers about MR-Angiography (MRA) and its application appeared in the early 1990's and MRA become clinically available to allow non-invasive imaging of the blood vessels without radiation or contrast medium injection. Ultrasound vessel imaging was also developed in that time and is applied as complement to the above mentioned techniques.

The evolution of angiography was also motivated and supported by development of invasive surgical techniques that allowed operations treating cardio-vascular problems, as cardiac catheterization (first vessel catheterization on Forsmann in 1929, first cardiac catheterization by Cournand and Richards in 1941), coronary angioplasty (Gruentzig in 1977), balloon angioplasty (Gruentzig, Myler and Hanna in 1977) and by needs of these treatment techniques.

1.3 Vessel Imaging Basics

As a result of evolutionary changes through the last hundred years three vascular imaging techniques have evolved as the modalities of choice:

- *Digital Subtraction Angiography* (DSA) is an invasive procedure, which requires catheterization of the arterial system, usually via the common femoral artery. An angiographic catheter is placed with its tip in the abdominal aorta, and short bolus of iodinated radiographic contrast medium is injected to opacify the dependent arterial system. The principle of digital subtraction angiography is first to obtain a digital image before the contrast medium is injected (mask image), and then obtain a sequence of images (frames) while the contrast bolus is rapidly passing through the arteries. A DSA image is generated by subtracting the mask image from the frames obtained with contrast medium, which results in the exclusive display of the arterial flow channels in the final image (Fig. 1.5, Fig. 1.7a). Due to its features, DSA provides high-resolution and high-contrast 2D pictures of very high diagnostic quality. DSA is therefore considered the reference standard for new vascular imaging modalities.

- *Computed Tomography Angiography* (CTA) has evolved from the traditional X-rays computed tomography. Its name comes from from Greek words *tomos* - 'slice' and *graphien* - 'to write or record', because the result of CT imaging are (axial) slices from the object (Fig. 1.8). This is achieved by rotating the X-rays source and detectors around the object (Fig. 1.6), recording the individual cross-attenuations. The slice images are then reconstructed from raw X-rays attenuation measurements by so called *tomographic reconstruction*, mathematically based on *Radon's transformation* [13, 14]. With the development of fast CT scanners, the scan times have decreased substantially, which has allowed to scan a particular anatomic region of the body while contrast medium is injected intravenously at the same time. The resulting bright vascular opacification combined with high-spatial resolution CT acquisition gave rise to so called CT-Angiography, or CTA. Modern CTA has evolved within the last years into an accurate, robust, and cost effective non-invasive imaging technique in patients with coronary or arterial diseases, thanks to the advent of helical multi-slice CT scanners which allow fast and precise 3D medical imaging of a human body. Current state-of-the-art 16- and 64-channel CT scanners allow acquisition of a set of transverse images representing the whole area of interest in less than 30 seconds. With a simultaneous use of contrast medium, the produced images are well-suited for angiographic purposes and due to the better contrast resolution of CT when compared to conventional angiography, contrast medium needs not be injected directly into the arterial system, but only into an arm vein, *intravenously*. CTA is thus much less invasive and less harmful for the patient. A CTA dataset of the lower extremity arterial tree (*peripheral CTA*) consists of approximately 1200–2000 images 512×512 pixels each, with 4096 levels of grey and resolution below 1mm^3 is produced. Within such dataset, vessels manifest densities that are different to those of the surrounding tissue, due to the contrast-medium enhancement of blood. As the number of transverse slices is very high, the radiologic interpretation of CTA dataset is laborious and lengthy and dedicated post-processing tools that generate a small set of easily interpretable images are typically used.

- *Magnetic Resonance Angiography* (MRA) is a variant of (nuclear) magnetic resonance imaging (MR, NMR, MRI) with special settings of parameters to allow visualization of blood in vessels. MRI is a non-invasive technique, in which properties of various materials in strong magnetic fields are employed. In medical MRI, the relaxation properties of excited hydrogen nuclei in water are most frequently measured. When the object being imaged is placed in a uniform magnetic field of high strength, the spins of the atomic nuclei with non-zero spin numbers within the tissue all align in one of two opposite directions: parallel to the magnetic field or anti-parallel. Only one in a million nuclei align themselves with the magnetic field. Yet, the vast quantity of nuclei in a small volume sum to produce a detectable change in field. The tissue is then briefly exposed to pulses of electromagnetic energy—radio-frequency (RF) pulses—in a plane perpendicular to the magnetic field, causing some of the magnetically aligned hydrogen nuclei to assume a temporary non-aligned high-energy state. In order to selectively image different voxels (volume elements) of the tissue in question, orthogonal magnetic gradients are applied. Images can be created from the acquired data using the discrete Fourier transform. The contrast in MRI is connected with time constants involved in relaxation processes that establish equilibrium following RF excitation. As the high-energy nuclei relax and realign, they emit energy at rates which are recorded to provide information about their environment. Image contrast is created by using a selection of image acquisition parameters. Common magnetic field strengths range 0.3-3 T (Tesla), although research instruments range as high as 20 T, and commercial suppliers are investing in 7 T platforms. Typical resolution is about 1 mm^3, research models head towards $1\ \mu\text{m}^3$. If time constant-weighted images do not prove

adequate information, additional enhancement by contrast medium can be exploited.

As stated above, to emphasize vessel tissue in the images a contrast medium injection might be employed. The media type depends on the imaging modality [2]. For X-rays modalities (DSA, CTA, . . .) contrast media that are hyperdense (cause higher attenuation of X-rays) are used. Currently used angiography contrast agents are based on iodine. The chemical base of these agents is a benzene ring with three atoms of iodine. Contrast media can be categorized into ionic or non-ionic compounds. Ionic agents were developed first but are generally not used for CTA as the non-ionic compounds have less side effects. The X-rays attenuation effect depends on the amount of iodine delivered. In the case of MRA, the vessels can be enhanced by injection of paramagnetic contrast agent, usually with a gadolinium compound (gadolinium is a rare earth metal from the group of actinoids).

In the clinical environment, all three of the above described imaging modalities are used for the evaluation of patients with peripheral arterial occlusive disease. Each of them has its own advantages and disadvantages. The general trend, fueled by the ongoing technical developments in both CT and MRA, is to replace diagnostic catheter angiography (DSA) completely with non-invasive CTA or MRA. Ideally, catheter-based studies should be limited to those patients who also undergo percutaneous treatment such as balloon angioplasty or stenting at the same time.

In the next chapters, we will focus on image post-processing of peripheral CTA data and visualization peripheral arterial occlusive disease. There have been two main reasons for our devotion to this kind of data:

1. In comparison with DSA, CTA provides 3D datasets, what opens new possibilities in processing and diagnostics. Compared to MRA, the spatial resolution of the CTA data is currently higher and the acquisition is simpler. Modern state-of-the art 16- and even 64-channel CT scanners are increasingly available in many hospitals and private practice settings. The scanning process is also significantly faster in the case of CT (seconds versus minutes).

2. We were also interested in assessing the clinical potential and practical usability of the CTA data or, in other words, 'to see what one can get out from CTA data for clinical purposes'.

The environment for this research was an interdisciplinary cooperation between clinical and computer graphics experts from the Medical University Of Vienna / Vienna General Hospital, Austria, the Institute of Computer Graphics and Algorithms—Vienna University Of Technology, Austria and the Commission for Scientific Visualization—Austrian Academy of Sciences, Vienna, Austria, later extended also by a cooperation with the Department of Radiology, Stanford University Medical Center—Stanford, California, USA. Our work was partially supported by the Austrian Science Fund (Fonds zur Förderung der wissenschaftlichen Forschung—FWF) within the grant No. P-15217 and FWF-TRP grant No. L291-N04. The goal of our work was to develop and evaluate computer graphics tools aimed at processing and visualization of the peripheral arterial tree in patients with peripheral arterial occlusive disease, imaged with CTA.

The achievements presented in this work build on and extend the results of previous work, notably of those, performed in the preparation period of this interdisciplinary AngioVis project (Kanitsar *et al.* [15], [16]). Our goal was to address the particular challenges of processing and visualization of peripheral CTA data, because this—as discussed in next chapters—is not only a direct implementation of known approaches and algorithms. In contrary, we focused our research on details that hampered routine application of the previously developed vessel processing & visualization algorithms and thus lower extremity CTA in general in daily clinical practice, where visualization is the true bottleneck of this new diagnostic imaging test. And as so often, 'the devil is hidden in the details'.

Figure 1.3: *Lower-extremities vessels significantly affected by PAOD, causing irregular lumen narrowing. (a) A maximum-intensity projection image of pCTA data after bone editing. (b) X-rays arteriography of a femoral artery. (Catheter injecting contrast media is also visible.)*
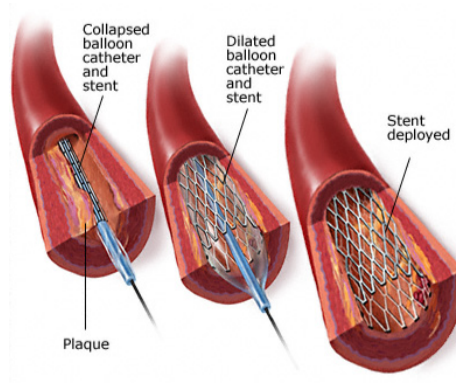
Figure 1.4: *Percutaneous Transluminal Angioplasty (PTA): first a catheter with compressed balloon and stent is inserted in the vessel; secondly, balloon is pressurized and the vessel is expanded; thirdly, expanded stent prevents the vessel to recoil and maintains the new diameter.*
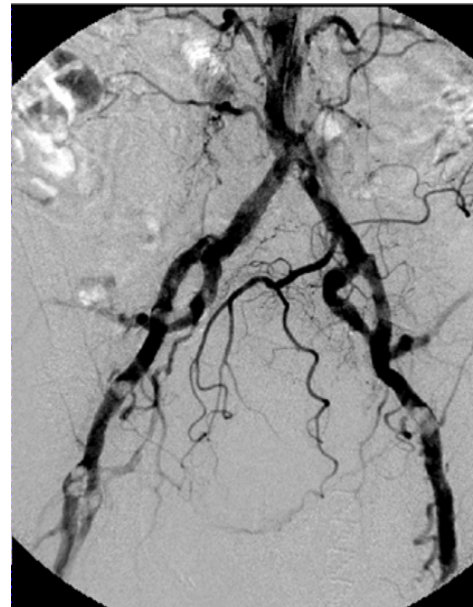
Figure 1.5: *Digital Subtraction Angiography (DSA) images of lower-extremities arteries. Dark structures is the contrast-medium enhanced blood vessel.*
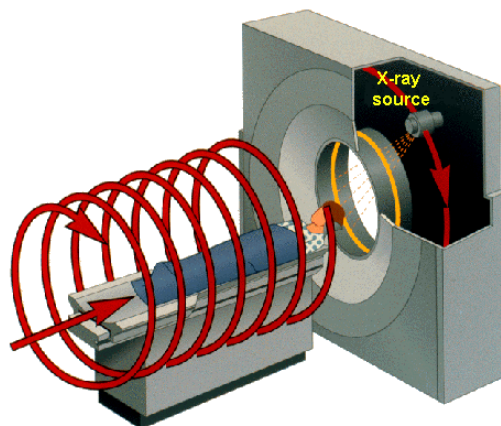
Figure 1.6: *Principle of (helical) CT scanning in medicine.*
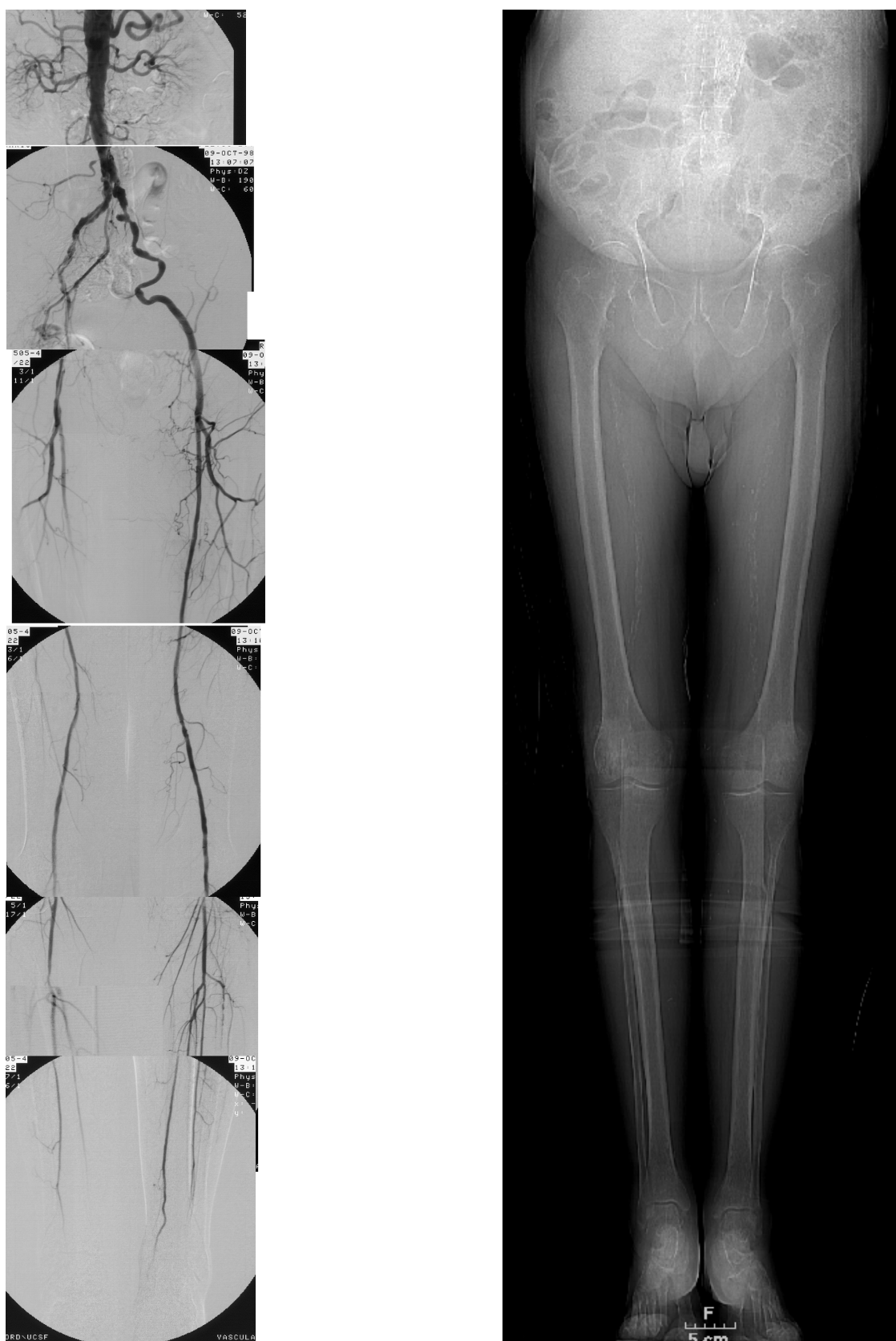
Figure 1.7: *(a) Reconstructed full-size digital-subtraction angiogram (DSA) of a patient. (b) Standard 2D radiographic image of a patient without contrast medium, thus the vessels are not visible. Used e.g. for pre-scan alignment of a patient position in CTA.*
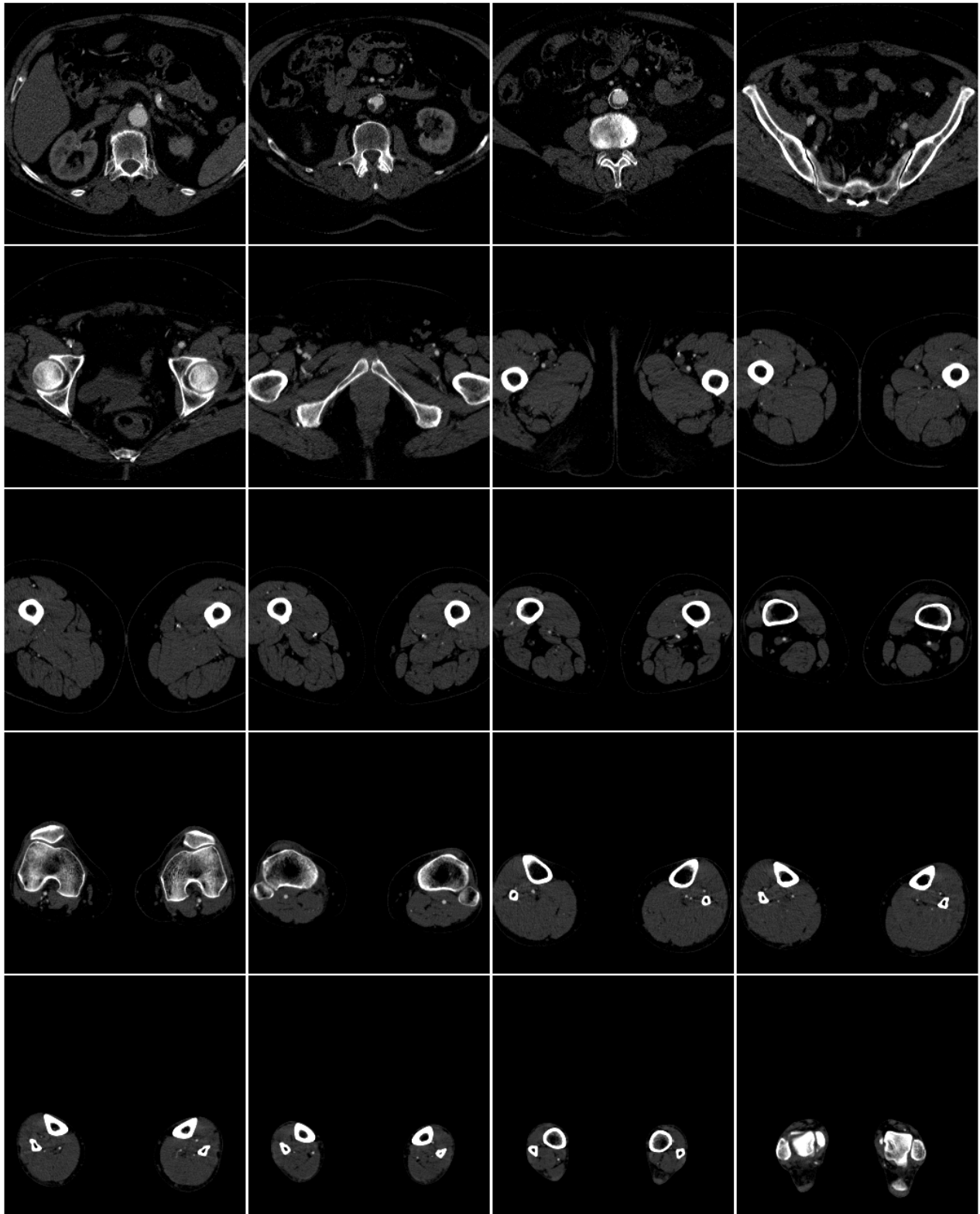
Figure 1.8: *Sample slices from lower-extremities peripheral CT-Angiography dataset (top left to bottom right: from abdomen, through pelvis, thighs, knees, calves to ankle area). The images show axial view of the patients' body. Vessels are visible as smaller bright circular objects due to the contrast-medium enhancement of blood. The largest and brightest structures are bone tissue.*

Chapter 2

Peripheral CT-Angiography Datasets

Peripheral CTA (pCTA) data are CTA scans of the lower extremity inflow- (aortoiliac) and infrainguinal runoff-vessels (femoro-popliteal and crural arteries), sometimes referred to as *'run-offs'*. Accurate imaging of the lower extremity arterial tree is a prerequisite for treatment planning in patients with Peripheral Arterial Occlusive Disease (PAOD), as explained in Chapter 1. Before we discuss the processing and visualization issues further, the input data needs to be described in detail, as its properties significantly affect and determine the applicable approaches.

2.1 Scanning Process

Peripheral CTA data are acquired using helical, multiple detector row, 4-, 16-, (or recently also 64-) channel CT scanners (Fig. 1.6, Fig. 2.1 and Fig. 2.2). The scanning procedure takes only about 20 to 45 seconds and during this time the patient table of the scanner is translated through the gantry of the scanner. Intravenous contrast medium is injected at the same time to opacify the arterial system. The specific *acquisition parameters*, such as tube voltage (120 kV) and amperage (150-350 mA), the gantry rotation speed (usually 0.5s of a full 360° gantry rotation), the table increment (table translation/360° of gantry rotation) and the *contrast-agent injection parameters* (injection flow rate [mL/s], and injection duration [s]) are prescribed in a *scanning protocol*.

Scanning protocols may vary slightly between scanners. The *reconstruction parameters* for a peripheral CTA include the reconstruction field of view (FOV, usually between 220mm and 280mm), the reconstruction kernel (usually a 'soft', or smooth kernel), the section thickness (typically 1.25 to 2.0mm), and the reconstruction interval or section spacing (usually $\leq$ 1mm). The minimal section thickness is limited by the size of the detector elements. The interpolation algorithms used for the reconstruction of transverse images from the volumetric (helical) CT acquisition allow that the z-position of a reconstructed transverse image can be chosen arbitrarily. In the setting of CTA, the section spacing is usually chosen smaller than the section thickness, resulting in a 50% to 20% 'overlap' of the data[1]. The spatial resolution, speed and noise parameters in helical scanners depend heavily on the selected number and combination of detectors and channels (Fig. 2.4 and Fig. 2.5).

---

[1] As the dataset is not acquired directly as a 3D volume, but as a stack of 2D slices, there exists two quatities describing the longitudinal resolution of the dataset. *Inter-slice distance* or *pitch* defines the distance of two consecutive planes of scanning. *Slice thickness* or *collimation* defines the thickness of each slice (as the scanned slice is not infinitely thin, see later in the text). These two values are not necessarily the same. If the inter-slice distance is smaller than the slice thickness (what is typical), the scanned slices represent overlapping volumes. For 3D dataset building, usually the inter-slice distance is taken, but in special cases it might be necessary to reconstruct the volume differently.

The resulting data is a set of 1200–2000 transverse axial slices (Fig. 1.8). The within-slice spatial resolution is typically <1 mm^3, whereas the through-plane resolution is usually lower. This is because the datasets are usually not isotropic. In other words, the size of a *voxel* (volume element) is different in x,y and z coordinate direction. This influences the processing of the data and needs to be taken into account. The size of transverse images is usually 512×512 pixels and the density information is represented by 12-bit gray-scale scalar values. The data are usually represented as 16-bit integers on the current digital computers which, together with the above mentioned number of transverse slices, results in a dataset size around 600–1000 MB. Currently it is a significant amount of data that is not easy to process and visualize at interactive frame-rates or when real-time manipulation is required.

The density (the attenuation of X-rays) for a given tissue in pCTA data is measured in Hounsfield units (HU). The basic range of the HU measure is defined as: -1000 HU is the density of air and 0 HU is the density of water. Because the attenuation of X-rays in CT images is rather constant for the given type of tissue, we can give a general overview of typical densities in CTA dataset, as described in Tab. 2.1. Within these values, *soft*

Figure 2.1: *Peripheral CT-Angiography imaging procedure in clinical environment.*
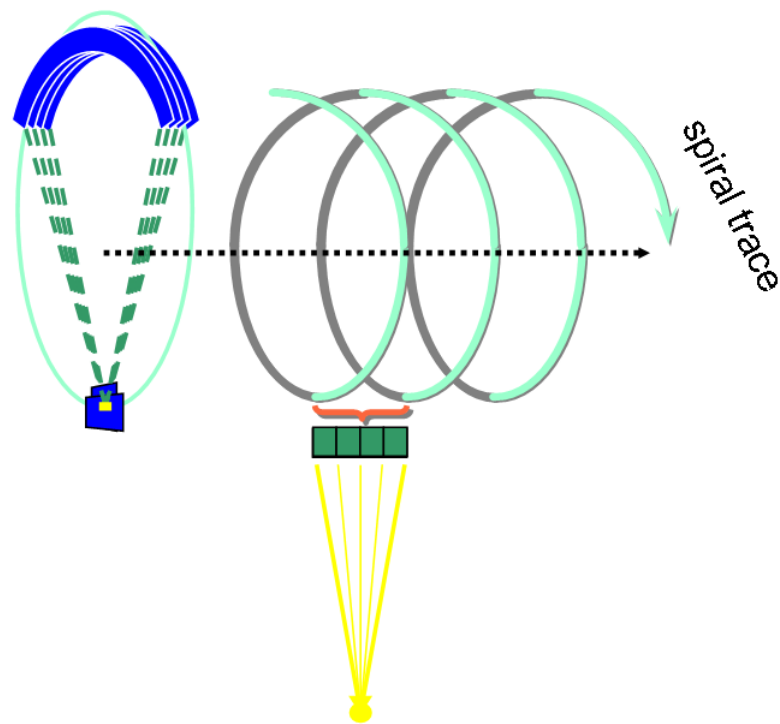
Figure 2.2: *Spiral CT scanning principle. The X-rays source and oppositely mounted detectors in rows perform two motions: 1. rotation around the axis, 2. longitudinal movement along the axis. In this way, a large anatomic volume can be scanned rapidly.*

tissue generally include muscles, ligaments, fat and most of the organs (liver, kidneys, etc.) Fat tissue has slightly negative values on the Hounsfield scale (-100HU to -10HU), lung tissue has also negative attenuation values, because it contains air (-500HU to -950HU). The *'contrast-agent enhanced vessel tissue'* is in reality the contrast-agent enhanced blood, because the normal vessel wall is too thin to be resolved with current CT scanners and its density properties are similar to the soft tissue. *Trabecular* or *cancellous bone* is a sponge-like organization of thin (below CT resolution) bony lamellae. This porous bone is located inside of the ends of long bones or inside the bodies of vertebrae. Due to its sponginess, it cannot be assessed correctly within the standard pCTA scanning protocol and the acquired result is only the average density in the given volume due to partial volume effect (see further). *Compact* or *cortical bone* is much denser and is located in the outer walls of bony structures, close to the surface. It manifests much higher attenuation of X-rays than cancellous bone, due to higher concentration of calcium. Cortical bone manifests the highest attenuation of X-rays in the human body (except for metallic implants). The density and CT attenuation of 'soft' (i.e. non-calcified) or calcified atherosclerotic plaque overlaps substantially with the above mentioned density categories. Soft plaque consists mainly of fibrofatty tissue and manifests density values equal to that of soft tissue. Calcifications, due to higher concentration of calcium posses densities in the range of cortical or sometimes trabecular bone. Occlusions, which completely block the flow of contrast-agent enhanced blood are indistinguishable from surrounding soft tissue, because the plaque/thrombus within the occluded vessel lumen has the same density. From Tab. 2.1 arises that density ranges for various tissues partially overlap (mainly vessel and bone tissue). Fig. 2.3 depicts this situation. This attribute of pCTA data, together with close vicinity of anatomic structures hampers easy

Tissue	Approx. density [HU]
Air	-1000
Water	0
Soft tissue (Muscles, Fat)	-200 to 200
Contrast-agent enhanced blood	150 to 500
Trabecular bone	200 to 500
Compact/cortical bone	500 to 2000
Metal (metallic implants)	>3000
Thrombus	65 to 85
Soft plaque	0 to 200
Calcified plaque	500 to 1000

Table 2.1: *X-rays attenuation in various materials/tissues in CT images.*

processing and analysis, as the objects cannot be recognized solely on their density properties. This aspect is discussed in detail later in Chapter 3. The scanning process is not an ideal measurement. As can be expected, the resolution of the scanner is finite and size of an imaged element is not infinitely small. The size of scanning element depends on the scanning parameters as prescribed in the scanning protocol, but generally the scanning renders volume ~ 1 mm^3 to one voxel of the data. Moreover, the scanning is a finite physical process and tomographic reconstruction is approximated by finite set of mathematical operations within a discrete domain, therefore the sampling of a CT scanner is not sequence of infinitely fast and tiny measurements. The sampling event can be better described as a function that weights attenuation of X-rays within the scanned element to an averaged density value in given voxel. This phenomenon causes spatial low-pass filtering (or blurring) of the scanned volume and is generally called *partial volume effect* (PVE). It results in averaging of attenuation values of different tissues in areas where they border or are in contact. In the image a less abrupt density change—not fully corresponding to reality— is then presented. This feature of the scanning process might be modeled by convolution of the hypothetical original volume with a low-pass filter, e.g. with a Gaussian filter. The parameter σ of the Gaussian filter is then determined by the properties of the scanner (*point-spread function*) and the scanning protocol. The PVE influences and limits proper acquisition of small or thin anatomical structures, their processing and visualization. Structures like porous bone or tiny vessels are significantly blurred in the pCTA data.

Scanning artifacts other than PVE may be also present. The typical source of scanning artifacts is the presence of metallic implants in patient's body. These might be metallic stents, orthopedic implants such as hip or knee joint prosthesis. Due to exceedingly high attenuation of X-rays in metals the data cannot be reconstructed properly, what results in typical 'starry' artifacts in CT. Other type of artifacts might come from a spatial misalignment of X-rays source and detector rows. This shift then causes errors in tomographic reconstruction. The spatial misalignment is mainly caused by high-speed movements during the scanning (detector and source rotation, etc.) and resulting vibration. In the latest CT scanner models this problem is solved by auto-calibration of the units before each scanning.
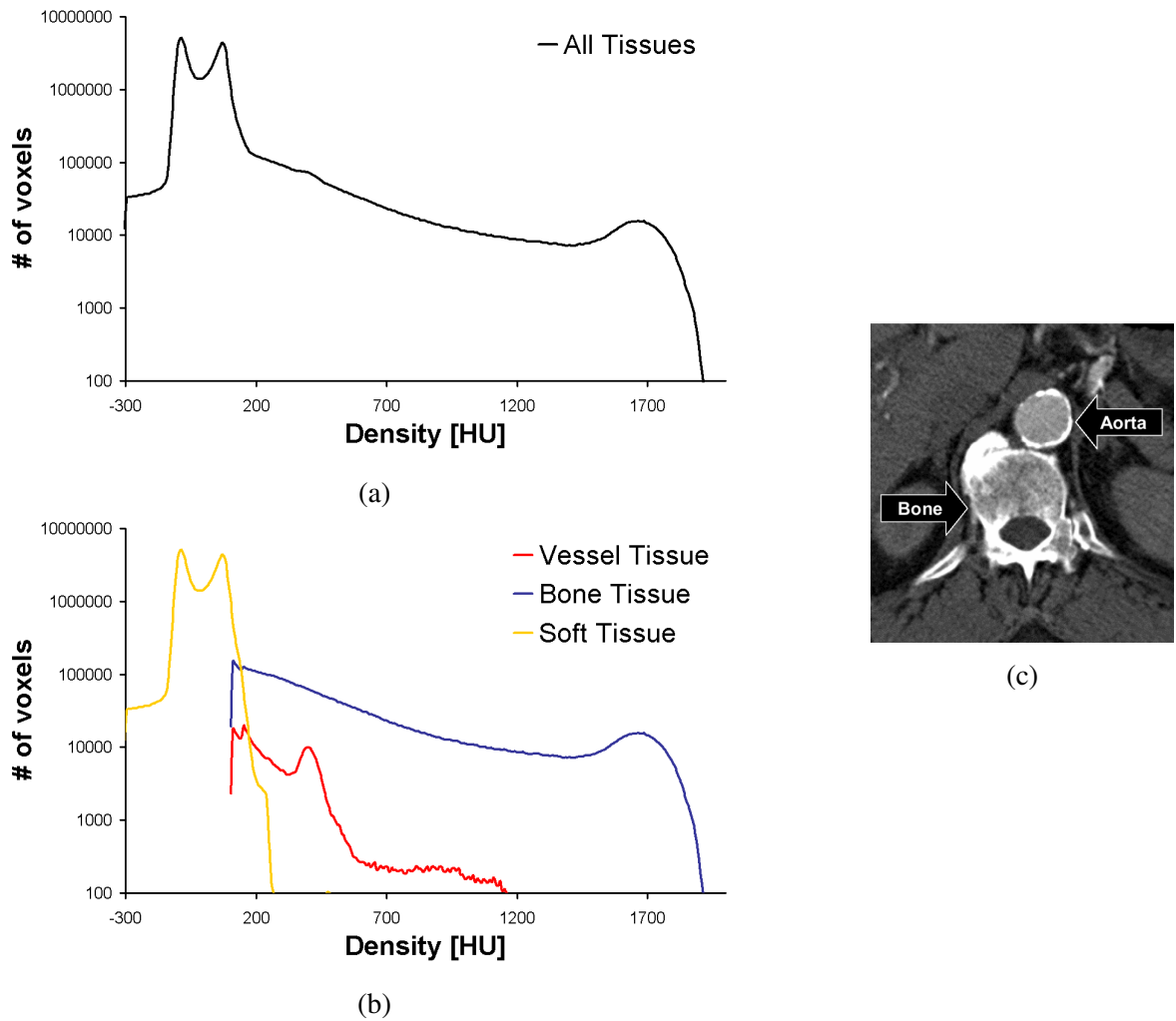
Figure 2.3: *Density histograms for tissues in pCTA data. (a) Histogram for unsegmented data. (b) Tissue histograms in a segmented dataset. Overlapping of density regions for various tissues can be observed. (c) A transverse slice from pCTA dataset at the level of the infrarenal aorta. Density range similarity between vessel (aorta) and bone tissue (vertebra) can be observed.*

2.2 Imaged Anatomy

Peripheral CTA data images the anatomy of lower extremities in the human body (Fig. 2.6, 2.7). Vessels (in our case arteries) in lower limbs are hierarchically organized in a *vessel tree*[2]. Certain structures within this tree are important for clinical assessment of the vascular diseases. The main vessel paths are the major conducting arteries which transport blood to periphery (as opposed to the shorter nutrient vessels that feed e.g. the muscle tissues), hence the focus is mostly on them, as described below. A normal anatomic lower extremity arterial

---

[2] The vessel tree of a healthy human is a real *tree* in a topological sense of its meaning, i.e. a structure that has a stem and branches but does not constitute *structural loops*. On the other hand, the vessel tree of a patient with PAOD has (or potentially in future might have) *by-passes* that circumvent occluded vessel segments. In a model of a vessel tree with by-passes the structural loops might occur, therefore a classical tree becomes inappropriate modeling. We suggest to model the anatomic vessel tree by means of an *oriented graph*, where nodes of the graph are the bifurcation points and oriented edges of the graph are the vessel segments with given direction of blood flow. In the following text, when discussing modeled vessel tree, we will always mean the oriented graph model, unless otherwise specified.

1 detector row   **8-34 rows**   **16-40 rows**

1 channel   **4 channels**   **8 channels**
16 channels
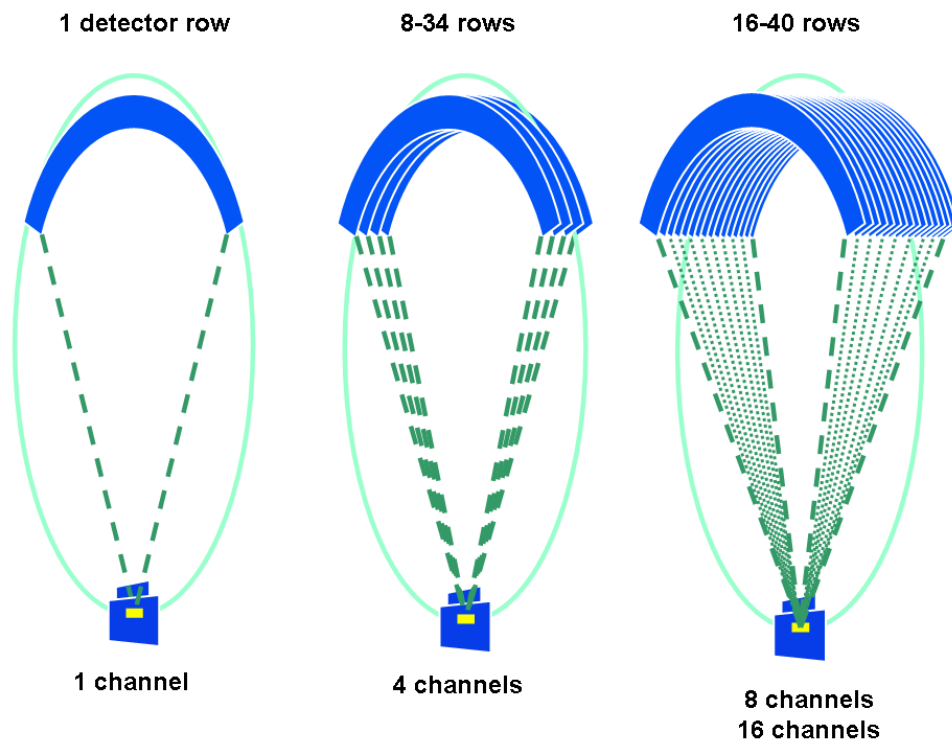
Figure 2.4: *Multiple-detector row CT scanning principle. According to the type of CT scanner, the X-rays detectors are arranged in a single or multiple rows. The cone-shape beam of X-rays excites several rows at once.*

4x1,25mm   4x2,50mm

4x3,75mm   4x5,00mm
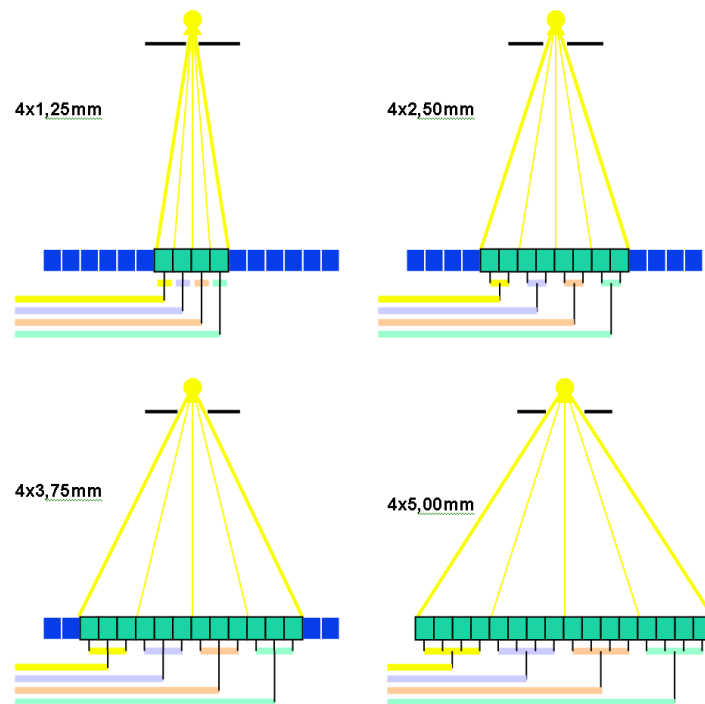
Figure 2.5: *Multi-channel CT scanning principle. The detectors arranged in rows are organized to channels. The number of detector rows in one channel defines the slice collimation parameter, the longitudinal spatial resolution of the data and influences the amount of used radiation and noise parameters of the scanning.*
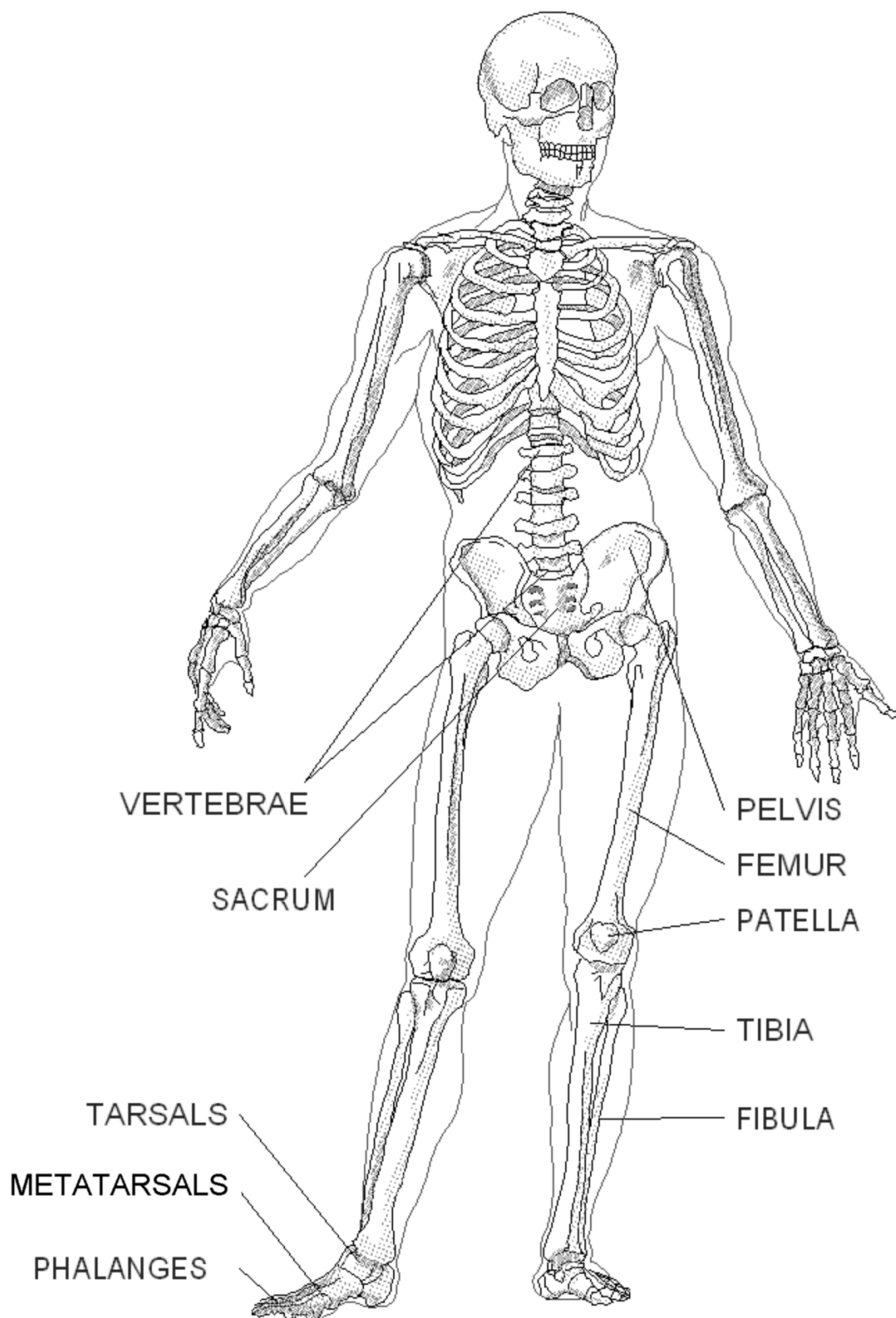
Figure 2.6: *Bone anatomy of the human lower extremities.*
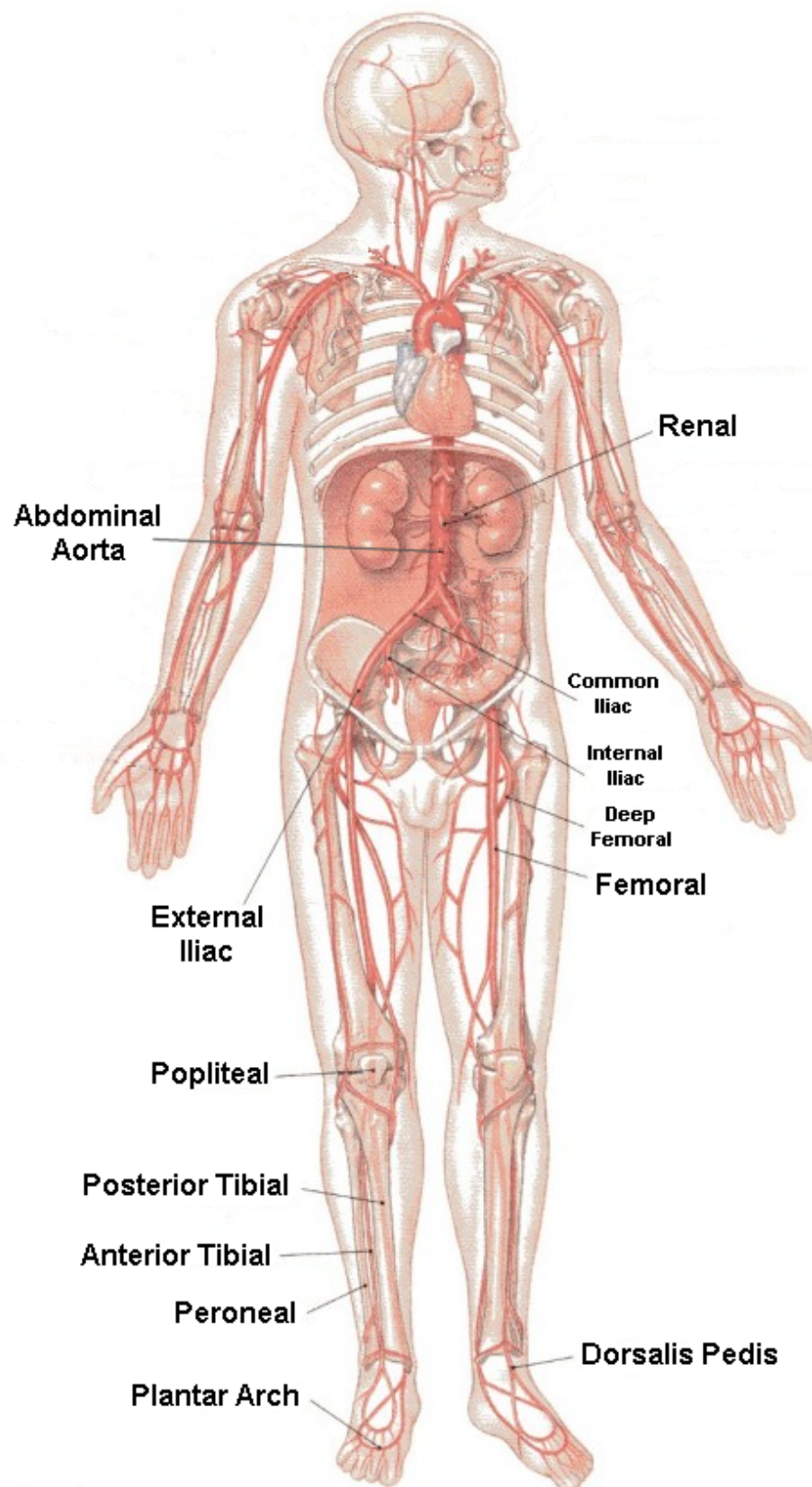
Figure 2.7: *Anatomy of the human lower extremities arteries.*

tree as seen on Fig. 2.7 begins with its stem in the abdominal aorta. In successive divisions, the vessel tree divides into smaller and smaller branches. The point of division is called *a bifurcation point*. The portion of a vessel between two successive bifurcation points we call a *vessel segment*. The path between two selected locations in the vessel tree (e.g. starting in abdominal aorta and ending in one of the small pedal vessels in the end of a limb) we call a *vessel path*. There are a limited number of vessel paths that are clinically relevant in the setting of PAOD. Generally speaking, the clinicians are interested to see the six paths in pCTA data, originating in abdominal aorta and leading to distant ends of:

- Anterio-tibial arteries (ATA), left and right,
- Posterio-tibial arteries (PTA), left and right, and
- Peroneal arteries (PA), left and right.

In addition to these six main conducting arterial tracks, in which the lumen should be shown, other clinical information in the image might be important. Smaller nutrient vessels (most obvious in the thigh area) branching off the femoral artery are called *collateral vessels*. These vessels feed the surrounding muscles, but if the conducting vessel is significantly narrowed (usually $\geq 50\%$ diameter) or occluded they may enlarge and serve as alternative flow channels to supply blood to the segments distal to the diseased vessel portion. Prominent collateral vessels signalize hemodynamically significant stenoses of the conducting arteries. Therefore, the display of the collateral circulation, if present, is clinically relevant as well.

2.3 Data Processing Pipeline

To generate clinically useful images that allow convenient visual assessment of PAOD, the input pCTA data need to be post-processed to extract and display the clinically relevant information. A processing pipeline providing such images typically consists of the following steps (Fig. 2.8):

- Peripheral CTA data acquisition (scanning),
- 3D volume reconstruction from 2D axial slices,
- Data pre-processing—masking of unimportant objects in the data (e.g. scanner table or cover sheets), suppression of noise, etc.,
- Tissue segmentation (bone, vessel, soft tissue labeling),
- Vessel tree extraction and modeling,
- Data resampling and image generation,
- Image storage in a clinical Picture Archiving and Communication System (PACS), and
- Image interpretation for diagnostic and treatment planning purposes.

Within the following chapters, details of the most important of these steps are addressed.

2.4 Features of the Datasets

At this point it is useful to summarize the key properties of the structures contained in pCTA data with respect to further image processing. Regarding the density properties:

- The tissue densities in pCTA can be considered partially ordered:
$$D(soft\ tissue) \leq D(blood) \leq D(cortical\ bone),$$

Scanning

**Reconstruction and
pre-processing**

Segmentation

Visualization

**Vessel Tree
Extraction**

**PACS
Storage**

**Image
interpretation**
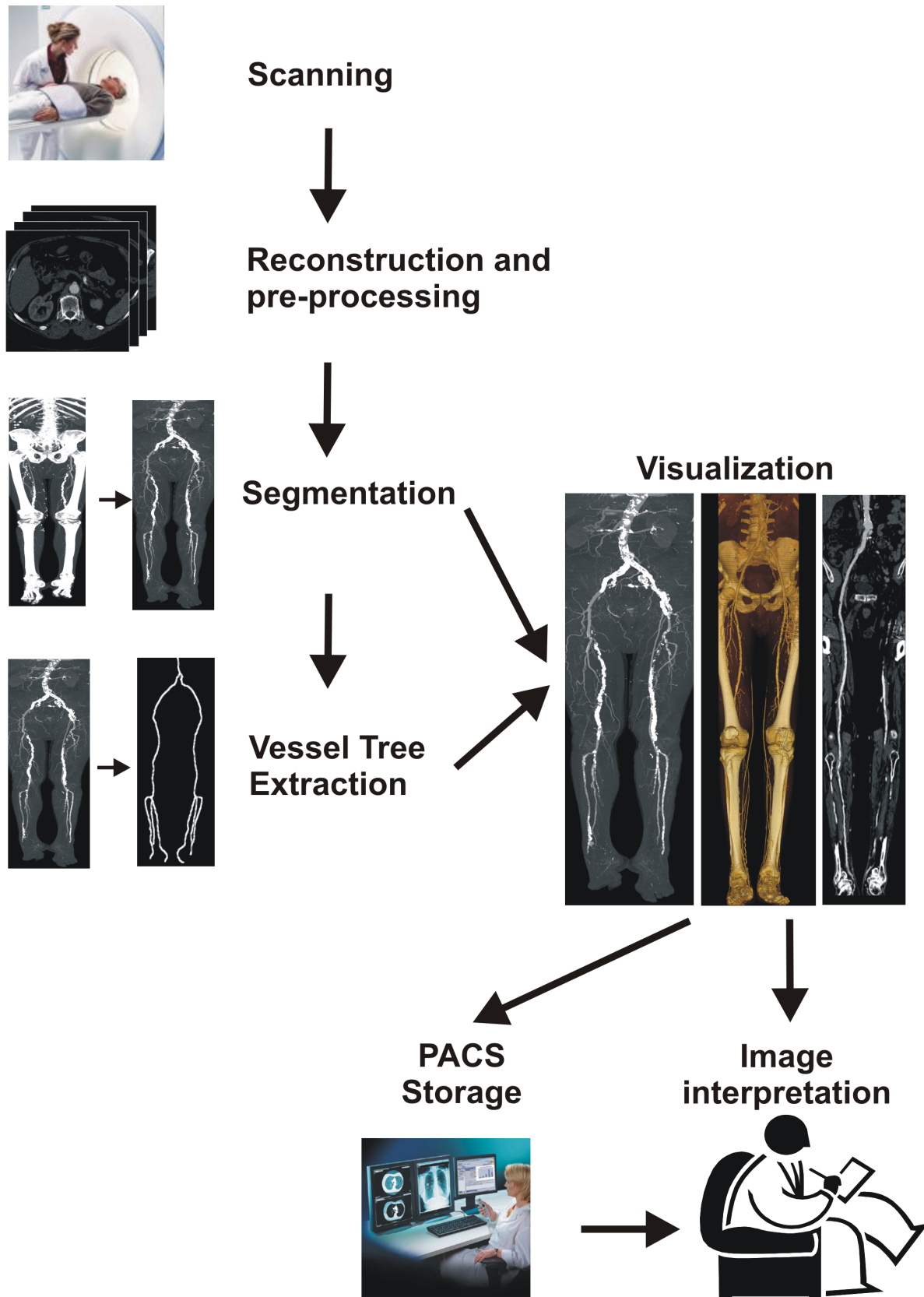
Figure 2.8: *Peripheral CT-Angiography data processing pipeline.*

- Contrast-agent enhanced blood manifests similar density properties as trabecular bone:

  $D(blood) \approx D(trabecular\ bone),$

- 'Soft' (non-calcified) plaque and occluded vessels have a density ranges similar to that of soft tissue, and

- Calcifications exhibit the same density properties as trabecular or cortical bone.

Shape information could be also taken into account:

- Vessel segments generally have the shape of a curved cylinder[3] due to hydrostatic pressure within. In cut-planes perpendicular to their axis therofore circular cross-sections are detectable (unless the vessel is very significantly diseased),

- The main vessel paths (down to ankle area) consist of nearly straight or only minimally curved vessel segments. On the other hand, vessels near and below the ankle, as well as collateral vessels exhibit significantly greater curvature and abrupt changes in direction. To some extent, abrupt directional changes are also observed in the conducting arteries in the region of the popliteo-tibial bifurcation,

- Vessels might run close to a bone or even get in contact with bone tissue. This can be seen in areas of:
  - abdominal aorta and bodies of vertebral bodies, typically in locations close to the aortic bifurcation,
  - internal iliac arteries where the vessels often touch the pelvic bones,
  - tibial and peroneal arteries (below the knee), where the arteries might be in contact with the tibia bone and the fibula over a length of several centimeters, and
  - the vessels in and below the ankle area (e.g. the dorsalis pedis artery) also often touches the tarsal bones.

The characteristic differences between bony structures and contrast-agent enhanced blood which might be exploited for differentiating these tissues from each other are:

- Bone tissue comprises of rather large structures, which are found in typical locations and are constantly spatially organized. Bones have very high density variability, depending on the type of bone tissue (cortical/trabecular), age of the patient and pathologic changes in the body (e.g. osteoporosis). The shape of bones is quite similar in a larger scale, but very variable at a closer look. The bones differ in length, curvature and shape, mainly in the area of the joints. On the other hand,

- Vessel tissue consists of rather small structures with the shape of curved cylinders, organized in a tree-like hierarchy. The general anatomic hierarchy of the vessel tree is anatomical quite constant, but again, individual variation is significant. The variability of individual vessel trees is also heavily influenced by the presence of vascular disease.

The above listed properties can be exploited for identification of vessel structures in the dataset. Nevertheless, such identification is not easy and straightforward. Several limitations, which are not immediately obvious, cause that the pCTA data differs from other CTA data (cerebral, coronary, etc.) and hamper the application of known processing techniques to pCTA data. E.g., in CTA runoffs the bones and vessels are present in close vicinity, which causes that vessels are not the brightest structures in the data, often not even locally (refer to Section 3.6 and the following subsections for more detailed explanation of this feature, limitations it causes and solutions for overcoming it).

---

[3]In the literature, many terms and synonyms are used to describe the curved cylindrical shape of the vessels—cylindrical, tubular, curvilinear shapes, etc. In our work, we will use the term *cylinder*, *curved cylinder* and *cylindrical* to describe this shape. The terms *tube* and *tubular* will be used only when referring to hollow cylindrical structures. The reason for this lies in a fact that vessels filled with contrast-agent enhanced blood show cylindrical (solid) shape in the pCTA data and not tubular (hollow) shape, even when vessels themselves are tubes and not cylinders.

In the next chapters, we analyze the existing approaches aimed on processing of CTA data and present modifications or suggest completely new approaches to achieve output that aids in advanced and precise PAOD diagnostics and treatment planning.

Chapter 3

Segmentation and Classification

3.1 Introduction

Segmentation and data classification (S&C) are often executed tasks in medical data processing. There, these refer to partitioning of the datasets into distinct regions, representing different organs or tissues. The goal is to introduce additional information to the dataset which can be later used in modeling and visualization steps[1]. Additionally, properties of the objects (size, volume, difference to previous examination, etc.) can be then assessed and quantified.

Generally, S&C refer to an assignment of information to the elements of the dataset, e.g. of probability of the examined element to be particular tissue. The information is usually assigned through labeling of the elements of the primary dataset. Single-, multiple- binary labels or continuous probabilities can be set. Binary labels telling relation to one or multiple tissues might be assigned, indicating 0.0 or 1.0 probability of the element to represent the given tissue. Assignment to multiple tissue types can be useful on borders or in areas where the truth is unknown (e.g. border of a lesion/tumor). Continuous probabilities can indicate either partial relation of the given voxel to tissue type (in this case the sum of probabilities is always 1.0) or the certainty of presence for given tissue type.

The complexity of S&C processes depends on the type of data, used modality, image quality, presence of noise and artifacts. For majority of medical datasets the S&C is not an easy task. The data typically manifest insufficient contrast, spatial distortions, intra- and inter-patient variability. This altogether significantly hampers adequate identification and separation of individual tissues or structures. A simple and reliable segmentation for medical data have been the subject of research of recent twenty years, but none of the presented approaches proved to be universally applicable. Usually, techniques tailored to individual modalities are designed and developed to allow application of 3D imaging in various specialized branches of medicine.

---

[1]The terms *segmentation* and *classification* are not always clearly used in the literature. In image processing, the segmentation is defined as a process of dividing the data to homogeneous regions (objects) and classification as a process that determines the class or type of particular regions. In further text, we use a slightly extended concept: we define *segmentation* as a division of the data to regions that belong to individual objects (these regions are not necessarily homogeneous) and *classification* as a process of determination to what tissue particular regions belong.

3.2   Segmentation and Classification of pCTA Datasets

The goal of S&C in pCTA is the labeling of contrast-agent enhanced blood, bone and soft tissues in the datasets for the purpose of: i) unoccluded visualization of vessel structures by simple visualization techniques (e.g. maximum-intensity projection, see Chapter 5), and ii) creating a reliable basis for vessel tree model extraction (Chapter 4). The modeled vessel tree model is then used for higher level analysis (computer aided diagnostics, etc.)

Improper, unreliable segmentation or classification results in clinically unusable images where the objects' details, important for diagnostics, might be absent or, on the other side, unreal structures might appear. An example of the former case is an incorrectly identified vessel—if identified as bone, it might disappear from the images with out-segmented bones. An example of the latter case is a part of bone identified as a vessel—impression of calcification deposits is then created. For the images to have good clinical value, the S&C must be precise—in the case of pCTA data with current resolution this means segmentation with precision down to a single voxel.

Practically, the S&C of the pCTA data can be reduced to S&C of vessel or bony structures. As the soft tissue is generally less dense then vessels and bones, it can be easily identified by e.g. thresholding or suppressed by transfer functions in a rendering stage. In certain cases, the projected soft tissue might cast a 'shadow' or 'outline' which can serve as a useful anatomic context in the images (for details on focus&context visualization refer to Chapter 5). Therefore, there is a need to differentiate only between vessel and bone tissues.

The bone and vessel tissues cannot be easily separated from each other by means of thresholding or region growing algorithms. Due to close spatial vicinity and overlapping density ranges (refer to Fig. 2.3) such methods do not deliver acceptable results. Therefore either manual, user-driven approaches or more complex segmentation algorithms must be applied.

3.3   Related Work

Even that vessel S&C is a subject of research for long time, the literature is quite sparse on the problem of peripheral CTA data segmentation, compared with segmentation of other types of CTA data (thoracic, abdominal, cerebral . . .). The size of the datasets, together with the fact that the limbs are less diagnostically important organs as e.g. brain, heart or liver can probably explain this situation. In most of the works, only partial problems were solved, not presenting globally applicable approach—as with actual imaging modalities there is probably none. Thus, in this section we give an overview of algorithms that are just partial solutions or similar in approach. It is impossible to review all segmentation and classification techniques, since it can be the subject of voluminous books and monographes [17], [18].

Starting with the most trivial methods, global thresholding (Weeks *et al.* [19], James *et al.* [20]) is the simplest statistical segmentation technique, where pixels are classified based on their intensity values. However, choosing the right density threshold is difficult and even with optimal threshold setting the segmentation often merges similar objects. Introduction of advanced techniques for intensity thresholding as expectation-maximization (EM) methods (Dempster *et al.* [21], Redner and Walker [22]) or usage of Bayesian formulation to derive the threshold (Duda and Hart [23]) did not fully solve this problem. Other statistical approaches include maximum-likelihood methods or non-parametric methods like k-nearest neighbors (k-NN) (Duda and Hart [23], Cooper *et al.* [24]), all with similarly suboptimal results. Alternatively manual, operator-assisted seg-

mentation with thresholding, morphologic and connected component analysis can be provided (e.g. Schiemann *et al.* [25]).

Observation that relying on density values have not brought acceptable results, the segmentation problem was reformulated as deformable model concept, trying to fit existing borders in the data to the model and geometrically describe this property, while keeping several constraints. Among these, remarkable results were achieved by snakes (Kass *et al.* [26]). The problem of snakes—the need to be initialized close to a real contour—was addressed by Cohen and Cohen [27] in the concept of balloons, by introducing inflatory forces. Later, due the another drawback of snakes and balloons—not being able to provide topological changes—this approach was complementary reformulated to level-sets (Caselles *et al.* [28], Malladi *et al.* [29]), utilizing front propagation techniques. The problem of initialization of level sets-based approaches was addressed by the bubbles algorithm (Tek and Kimia [30]). Bubbles were reported to be very effective in segmenting images with small structures (e.g. vascular structures), which render manual initialization impractical. However, practical use of bubbles requires tuning of parameters and appropriate domain-dependent stopping time (for the fronts) to be selected by the user. Other solution for handling topological events were addressed by adaptable snakes (McInerney and Terzopoulos [31], [32]). Caselles [33] and Kichenassamy [34] proposed geodesic active contours to tackle the convergence issue. Application to medical datasets was proved e.g. in the work of Niessen *et al.* [35]. All these models have the disadvantage of being able to take almost any arbitrary (smooth) shape without being constrained on the overall shape that is characteristic for a particular object type. This problem was addressed in work of Cootes and Taylor [36], [37], where they proposed a Point Distribution Model (PDM) as a polygon with fixed number of labeled points. These points create landmarks for point-to-point correspondence in a training set. Such description allows derivation of an 'average' model with variability. This Active Shape Model (ASM) then involves searching of a shape in a range of valid modifications.

Another class of techniques for segmentation is region growing and region merging, where initialized seeds grow by annexing 'similar' voxels. The similarity is defined by a statistical test (Beveridge *et al.* [38]). Region growing is typically followed by a region merging where small regions are grouped into larger ones using a statistical test again. Region growing often suffers from similar problems as the thresholding approaches. Seeded region growing (Adams and Bischof [39]) improved the traditional region growing by introducing 'a competition' between growing regions by ordering all candidate 'growth' voxels according some suitability criteria. It starts with a set of seeds and in each step of the algorithm one voxel is added to one of the growing regions. If a voxel adjoins two different regions, it is annexed by the more similar one. This process is repeated until all voxels have been allocated to one of the regions. The global competition ensures that the growth of regions near weak or diffused edges is delayed until other regions have had a chance to reach this area. In this way, it remarkably improves performance of the traditional region growing methods. However, seeded region growing does not incorporate any geometrical information and hence can 'leak' through narrow gaps or weak edges. It also does not allow for recovery from errors, i.e. once a seed 'leaks out' of the region (object) it is supposed to capture, it cannot be pushed back into the region.

Region competition approach proposed by Zhu and Yuille [40] combined the geometrical features of deformable models and the statistical nature of region growing, by using a combination of statistical and smoothing forces for seed growth. It also introduced a local competition between regions when they contact each other, by trading voxels that result in decrease of energy, thus allowing recovery from errors. As a result of competition between two adjacent regions, the local deformations of their boundary are based on a single smoothing term for the boundary and a competition between two statistical forces. Region competition implements a

back-and-forth competition between adjacent regions, which is continued to convergence. After convergence, two adjacent regions are merged if it leads to a decrease of energy; in this case the competition resumes and is continued until a final convergence is reached, resulting in the final segmentation. Region competition is a powerful technique that works well in a wide variety of images, including ones with diffused or weak edges. However, as described in Sebastian [41], this method needs improvement in at least two areas: curvature computation is not reliable due to discrete representation and boundaries can move either by an entire voxel or not at all. It is also dependent on initialization. If the seeds are set asymmetrically (one seed close to object border and other much further), the first seed tends to 'leak through' a border. Moreover, the method did not allow to split once merged regions, another aspect needed for error recovery.

Region-based segmentation methods such as region growing make use of homogeneity of inner regions in images. These methods may lead to noisy boundaries and holes inside the object because they do not consider boundary information explicitly. Markov-Random-Field (MRF) models have been used in segmentation applications for a long time (Hurn *et al.* [42], Choi *et al.* [43], Held *et al.* [44]). MRF models are probabilistic models that use the correlation between voxels in a neighbourhood to attribute pixels to different objects and background. MRF models produce better segmentation results because the pixel's attribute is decided not only by itself, but also by the statistic information in its neighbourhood. The main drawback in the use of MRF models is that the process of achieving the maximum a posterior (MAP) estimation of the object region can be computationally expensive. Geman and Geman [45] employed the Gibbs sampler to create an energy function that can be easily minimized to avoid the formidable computational burden of the MAP estimation. They also attempted to consider both the boundary and the region information during segmentation. However, in presented works (Geman and Geman [45], Derin and Cole [46], Lakshmanan and Derin [47]) the segmentation performance was limited by the fact that the pairwise Gibbs prior model contains only incomplete boundary information. In the work of Chan [48], [49] and Chen with Metaxas [50] this was solved by construction a new energy function for the high order Gibbs prior model.

Watershed transform (WT) (Vincent and Soille [51]) is a morphological gradient-based technique which can be intuitively described in 2D as follows: View the gradient image as a height map, and gradually 'immerse it in water', with water leaking through the minimum gradient points and rising uniformly and globally across the image. Place a 'dam' when two distinct bodies of water (catchment basins) meet and continue the process until water has all the points in the image. The dams provide the final segmentation. This can be interpreted in the image domain as the growth of seeds placed on the minima of the image gradient-height map at a time proportional to their height, that finally converges on the crest lines of the gradient map. WT is a powerful approach especially where local gradients cannot be defined, e.g. at diffused edges. A typical problem of watershed techniques is the problem of oversegmentation, what makes application of watersheds in medical data processing difficult. Often, artificial markers or 'sinks' are used (Grau *et al.* [52]).

3.3.1   Bone Segmentation Techniques

During the years, several approaches were proposed to segment or extract bones from CT data. Ahmad *et al.* [53] applied simple thresholding to extract femoral bone for the purpose of hip endoprosthesis modeling. Fiebich *et al.* [54] used thresholding and volume growing to segment bone in chest CT, where distance between bones and the vasculature was substantial. Kwan *et al.* [55] used artificial intelligence approach to detect gaps and narrow tissue bands to segment vertebrae from CT images. Kang *et al.* [56] applied thresholding, region

growing, morphological operations and closed-contour analysis complemented with operator intervention to segment hip joint, knee joint and skull. Yao *et al.* [57] exploited the idea of contour-tracing. By having seed-points close to real edges, they detected the gradient maximum and traced the edge in close neighbourhood. In areas where two bone structures were close, they ignored structures having dissimilar normal vector of the contour. Sebastian *et al.* [41] employed deformable models, region growing, local and global region competition for segmentation of carpal bones in hand CT data. Wang *et al.* [58] relied on similarity between CT slices. They parameterized the bone-contour (first slice segmented automatically) by the means of Fourier descriptors and then neighbouring slices were statistically compared in the Fourier descriptor space. Behiels at *et al.* [59] derived image features based on ASM and PDM as introduced by Cootes and Taylor [36]. Using a set of valid shapes, they extracted femur head in 2D radiographic images. In the work of Snel *et al.* [60] 3D deformable surfaces were used to extract edges of carpal bones. The deformable surface worked with binary images— thresholding and morphologic operations were used for CT data. Descoteaux *et al.* [61] suggested to use the Hessian matrix to detect planar structures and thus detect the sinus bone in skull for the purpose of pituitary surgery.

3.3.2 Vessel Segmentation Techniques

Vessels are structures of high interest in human body. Therefore, processing of medical data often focuses on their segmentation. The general challenge is that vessels in datasets do not posses constant or homogeneous densities, but rather form a shape that could be isolated by its local density difference. For this reason, many segmentation algorithms try to introduce 'shape' information at the expense of simple thresholding or gradient information utilization. Because many vessel 'segmentation' algorithms fall rather in a class of *vessel model extraction techniques*, they will be discussed in Chapter 4. Here, we review only plain segmentation techniques. A very good review of vessel segmentation can be find in review work of Kirbas and Quek [62]. Because of certain similarity among CT and MR data, we review methods proposed for both modalities.

Line filtering methods have constituted the very first algorithms used for analysis of MRA data (Marchal [63]). Later, anisotropic and dispersion filters were proposed for MRA enhancement (Gerig [64], Chen and Hale [65], Du and Parker [66]), Orkisz *et al.* [67]) and in the recent works of Westin [68] and Sun and Parker [69]. More about model-based filtering can be found in Section 3.6.

For simpler cases, mathematical morphology approaches were also proposed for the vessel segmentation problem. Hysteresis thresholding was first performed by Gerig [70]. Yan *et al.* [71] applied difference of density and gradient image followed by morphologic operations in head CT to extract blood vessels and ring of Willis. Kawata *et al.* [72] used thresholding, connected component analysis and smoothing to extract vessels from CT data.

Watersheds methods were employed by Passat *et al.* [73] for segmentation of specific venous structures and as a preliminary step in work of Kobashi [74]. Grey-scale skeletonization was used by Yim [75]) to segment vascular structures containing subvoxel-sized vessels.

Region growing methods are based on the hypothesis that vessels can be reconstructed from a seed point by iteratively adding voxels belonging to the vascular network. This approach was exploited by e.g. Cline [76], Klose *et al.* [77] and others. Beier *et al.* [78] implemented a system where user interaction and region growing were used to extract aortic stents in CT data.

Deformable models are used in vessel segmentation methods in order to determine vessel axes and or vessel

walls. These models are designed to evolve under external and internal constraints such as vessel shape and intensity criteria. A level-set approach was proposed by Lorigo *et al.* [79] to segment vessel axes before segmenting their radius. Deformable models have been also mixed with model-based segmentation (e.g. Frangi *et al.* [80]). Auer *et al.* [81] reconstructed stenosed artery from high-resolution MRI data by application of snakes, which initialization was based on thresholds. Verdonck *et al.* [82] incorporated dynamic programming for optimization of deformable models to extract borders of vessels in 3D data.

Statistical analysis methods are designed to find vascular structures by using different statistical distributions to model both enhanced blood and background. An expectation-maximization is generally used to classify each voxel of the processed angiographic image. In Chung [83], a Maxwell-Gaussian mixture density is used to model the background signal distribution while a uniform distribution is used for blood. Noble and Wilson [84] applied Gaussian approximation of the density histograms in a hierarchical way to segment vessels from TOF MRA data. In Sabry Hassouna [85] MRA data are processed as a mixture of one Rayleigh and two normal distributions.

According to our experience, most of the presented approaches are neither directly suitable for vessel segmentation in pCTA datasets, nor for bone identification. Therefore, we focused on alternative approaches, namely probabilistic atlases (with support of watersheds) and model-based segmentation. Our conviction is that small-area density or gradient information is not sufficient in segmentation of pCTA data and therefore some kind of external knowledge has to be introduced in the segmentation, allowing the algorithm to 'recognize' the sought structures. The datasets have to be 'understood', so e.g. information whether the given object can be a vessel is needed. A decision about the potential vessel objects—similar to as how human operators do decisions about the objects—must be done, based on multiple parameters as are density, size, shape, orientation and location. Alternatively, this decision can be done for other objects, e.g. bones.

3.4 Probabilistic Atlas for pCTA Data Segmentation

As the pCTA data are complex datasets (they contain a lot of different anatomy) and the objects within are of similar size and density ranges, it is often very difficult to distinguish between these objects. Hence, objects might be sufficiently precisely recognized only if additional information is taken into account (location, shape, etc.) Such information can be stored in an atlas, holding typical representatives of objects of interest, with their average parameters values and potential variabilities. Using such an atlas it is possible to distinguish valid and invalid variations of the particular objects. For this, datasets being classified need to be first scaled, aligned and registered to the atlas data space before executing the comparison. The higher variability of the examined objects, the more complex and difficult is the registration step, if reliable results are expected. Segmentation by means of deformable models and atlases is usually applied when it is not possible to identify objects of interest solely on the density data. In this sense, they represent a complement to the density-based techniques, which in a preprocessing step provide the low-level features for the subsequent atlas matching [86, 87].

Recently, significant effort has been directed towards the development of deformable templates—typically for segmentation of human brains ([88], [89]) and rich literature has been compiled on brain probabilistic atlases ([90], [91], [92], [93]). For example, Iosifescu *et al.* [94] differentiated between brain white and gray matter and cerebrospinal fluid in a first stage by a classification algorithm based on interactive selection of representative samples for each tissue. In the second stage, the segmented dataset is elastically deformed to an atlas [95], in order to measure the volumes of small brain structures. The deformation itself is defined by the maximization

of a local similarity structure, leading to a multi-resolution FEM solution. As the results of deformable atlases were promising, there were approaches to extend the atlas approach also to the other regions of human body. Ga *et al.* [96] proposed segmentation of liver and kidneys using a deformable surface model. Park *et al.* [97] described a probabilistic atlas aimed on abdominal area. In their work, thin-plate-splines were used as non-rigid warp and the approx. 40 control points were manually defined by a human operator. Mutual information was used as a similarity measure. The various abdominal organs were then modeled by means of Gaussian distribution and Bayesian inference combined with MRF was used for segmentation of unknown datasets.

A more general approach was proposed by Warfield *et al.* [98]. The adaptive, template moderated, spatially varying statistical classification (ATM-SVC) technique combined matching to an anatomical atlas with density-based classification in an iterative loop. Its aim was to propose a general purpose technique for segmentation in different anatomy areas and was tested, among others, on segmentation of knee cartilage from MRI data. First, a template of normal anatomy is build by an operator-driven manual or semiautomatic technique. Subsequently, it is converted to a set of distance maps, each indicating locations where bones and cartilage are likely to be found. For each unknown dataset its statistical density model is formed by manual selection of representative voxels for each tissue type. The iterative loop starts by a rigid transformation of the unknown data to the template space. Then, co-registered distance and density probability data are classified by K-nearest neighbor classifiers. In the loop, both the unknown dataset and the template are matched by an elastic matching procedure, which leads to improved tissue classification. The loop usually converges in three to five iterations.

As the tissue segmentation in pCTA data is a challenging and still unsolved task, we have proposed a probabilistic atlas solution [99]. The idea of the atlas aimed on segmentation of bones in pCTA data came from discussions with skilled radiologists. It seems inevitable to incorporate in the segmentation process some pre-knowledge that comprises information about patient anatomy, because methods based only on density and gradient analysis simply cannot cope with the diversity of pCTA data. Similar to a human radiologist, the computer also must utilize spatial anatomic knowledge and be aware of what kind of tissue could be in processed in given areas. This idea leads us to a goal to construct an atlas comprising spatial probability existence information about given tissue type. It is also encouraged by anatomic diversity of the processed datasets that may appear similar on the first sight, but are not on closer look.

In anatomic atlases, spatial position of organs in body is depicted, as the body is rather constant considering the spatial organization. Given organs usually appear on known spatial positions, with minor modifications. Also for anatomy in lower limbs, one can recognize typical spatial patterns. Not only the skeleton is similar among the patients, also the position of main vessel courses is approximately known. But the spatial variations of a skeleton are much smaller than of a vessel tree; bones also suffer less pathologic changes. Therefore we focused ourselves on atlas-based segmentation of bone tissue[2].

The main assumption is that if density/gradient information alone is not sufficient for reliable bone segmentation, it can be complemented with information of spatial location. So, we proposed to create an anatomical atlas aimed on segmentation of lower-extremities bones. In such atlas, following information is stored: the typical density of bony tissue in a given spatial point (possibly with allowed variations) and the probability for a bone tissue to be present in particular location. As an output of comparison between the unknown data and the atlas, the value describing joined probability of being 'bone density' in 'bone area' will come out.

In order to build and use such an atlas, it is necessary to deal with the following issues:

---

[2]When bones will be identified, vessels will remain the brightest structures in the dataset, making it easier to segment them by means of e.g. thresholding.

- the spatial variability of the processed datasets, caused mainly by different positions of the patients during scanning,

- anatomic differences among patients, mainly due to body proportions, gender and age,

- the different scanners and scanning protocols used, resulting in differences in data sampling, and

- extraction, storage and interpretation of appropriate information for a given tissue type.

Usage of non-rigid transformations (e.g. thin-plate spline warping) can help to solve the first three issues. A solution to the last one can be based on the idea of having statistics of the possible densities in the given spatial point, as well as on representing the probability of presence of certain tissues in this position. This idea is based on the observation that the densities change heavily in the global extent, but just slightly in the local range, and there exists a statistic measure of presence of the given type of tissue in the given spatial range. This spatial statistic measure can be transformed to a distance field which better represents the probability of tissue presence also in the areas where there is no relevant information. Distance transformations (DT) and distance fields (DF), arrays holding distance to certain object of interests (Borgefors [100]) represent a powerful means to encode knowledge about spatial relationships in both planar and volumetric scenes. For example, DT stands in the background of a fully automatic scheme proposed for brain segmentation in MR scans by Brummer [101]. There, data voxels are classified first according to a probabilistic density model. Since in MR data different tissues occupy the same spectral space, in the second step only those regions are classified as brain, which have at least a certain distance from the skin surface. The necessary DF is obtained by skin identification by thresholding and a DT. Zeng *et al* [102] proposed a technique for identification of the brain cortex, which takes advantage of the fact that the cortex is a layer approximately 3 mm thick. DTs are in this case used to measure the distance between the inner and outer cortex surface.

The presented probabilistic atlas method consists of two independent steps: first, we have to construct the atlas (Section 3.4.1) and second, we have to use the information stored in the atlas for segmentation goals (Section 3.4.6).

3.4.1   Atlas Construction

The probability atlas (Fig. 3.1) stores for each voxel information regarding the *Average Bone Density*, *Average Distance* to bone surface and the distance variance. As an auxiliary information necessary when adding new datasets (records) it also stores the total number of added records (*Record Count*) and the number of records, for which the voxel was identified as a bone voxel (*Bone Count*).

The atlas's *Reference Frame*, which defines its dimensions, sampling rate and a set of landmarks for registration is given by the first inserted record. Having at disposal this reference frame, one can easily add new records and compute the necessary information. An input record for each new dataset to be added to the atlas consists of the original density volume, a manually segmented bone mask and a set of landmarks, which define its correspondence with the reference frame. Currently, the landmarks are set manually by a simple interactive utility and pairwise correspond to those set in the reference frame. The density data was segmented by means of the semiautomatic utility ISEG [103], which is based on interactive thresholding, connected component analysis and application of morphologic and logic operations. When adding a new record to the atlas, both the density and mask volumes are warped by means of the thin-plate spline transform (TPS) to the reference space. However, since the manual landmark setting proved to be not precise enough, their position is optimized first with the help of a mutual information-based cost function (Section 3.4.4). In the next step, the atlas average
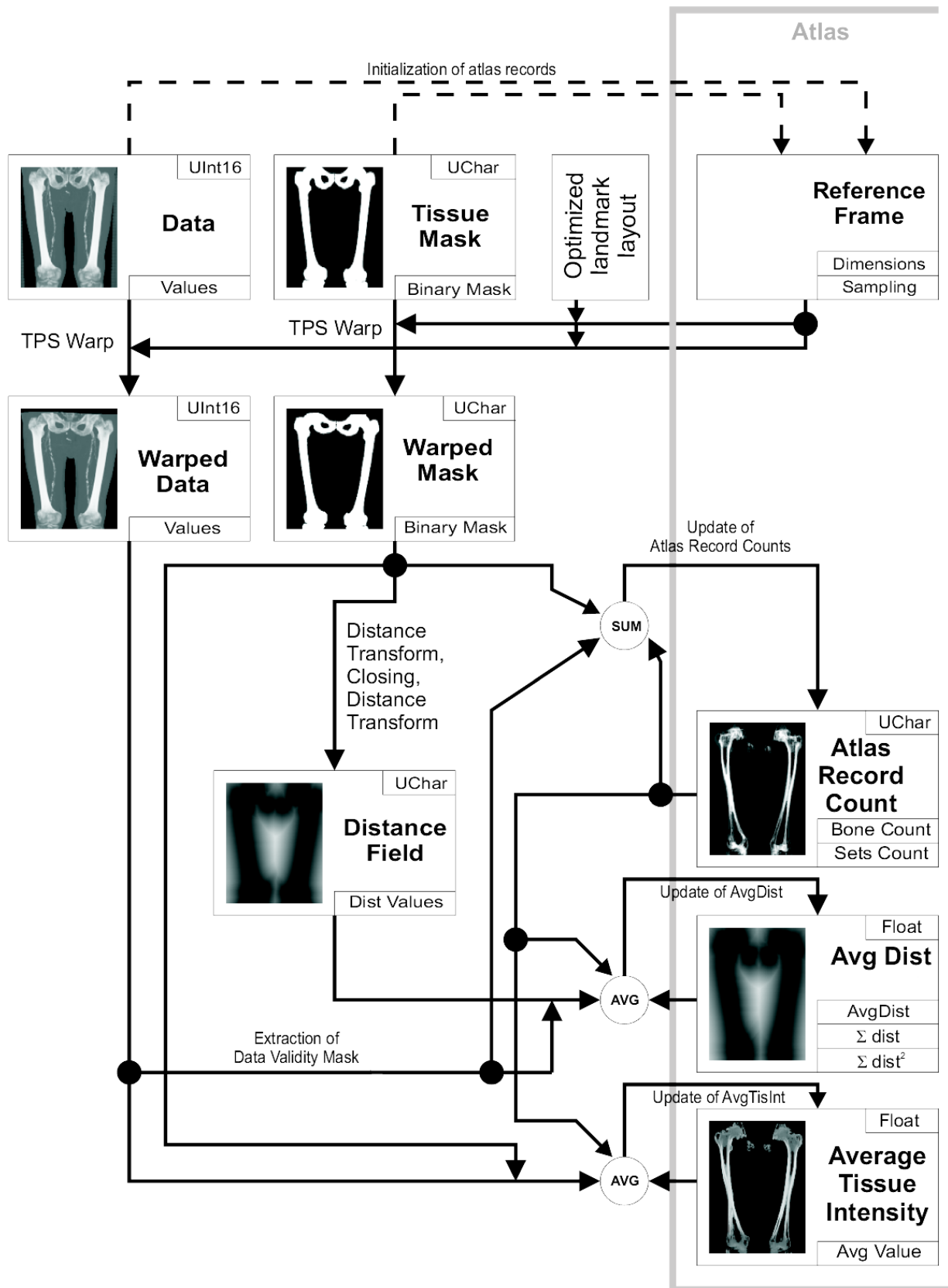
Figure 3.1: *Construction of the probability atlas for bone segmentation in pCTA datasets.*

bone density and average distance volumes are updated, using the warped density and mask volumes and the atlas record and bone count volumes. The distance volume of the processed record is computed from the mask volume transformed by the 345-chamfer-distance transform [100]. Prior to the distance transform, the bone mask is subjected to morphologic closing in order to fill-in bone holes which belong to areas filled by bone marrow. A distance transform based closing [104] is used with closing distance equal to 16, what seems to be reasonable value for given datasets. Since in the segmentation phase we take advantage not only of the mean distance, but also of its variance, we store in the atlas also a sum of squared distances for each voxel.

3.4.2   Dataset Warping and Registration

As the position of the patients in the dataset vary significantly and the shape of human skeleton also varies (due to age, gender, height, weight, etc.), for construction of the atlas and also for later atlas usage registration of the datasets must be executed. Registration is a task, where objects and their shapes among datasets are aligned. The registration consists of these steps:

- *Definition or detection of corresponding points* in the template and registered dataset. These points (landmarks) are given explicitly (manually by the operator) or can be derived automatically. They represent important anatomical information (features) that match after registration.
- *Warping* of the registered dataset to the space of the template dataset (or vice versa). The warping is an interpolation process in which we align the set of landmarks and volume inbetween is deformed. The deformation between the landmarks is ruled by certain criteria, e.g. can be based on physical model of bending of real materials with limited compressibility or stiffness, etc.

Eventually, the process can be complemented with:

- *Evaluation of similarity* between the registered and template dataset, possibly with optimization. The similarity measurement depends on the type of template and registered image (same/different modality, difference in brightness/contrast, etc.) The measurement should indicate a possible misalignment and dissimilarity of the two registered datasets and should serve as cost function for registration optimization.

According to the evaluated similarity, the count or the position of the landmarks might be modified to optimize the registration. In case of the proposed atlas dataset, the landmarks are defined manually by the operator. They represent important anatomical points (joints). With the defined set of landmarks, thin-plate spline warping is executed to register the dataset and atlas.

3.4.3   Thin-plate Spline Transform

Thin-plate spline transform (TPS) is an elegant algebraic expression of the dependence of the physical bending energy of a thin metal plate on point constraints. Its extension to 3D space allows modeling of shape deformation changes in 3D datasets (Fig. 3.2). The TPS transform is defined by n control points $[X_i, Y_i, Z_i]$ [105]:

$$x = a_0 + a_1 X + a_2 Y + a_3 Z + \sum_{i=1}^{n} F_i r_i^2 \ln r_i^2 \tag{3.1}$$

$$y = b_0 + b_1 X + b_2 Y + b_3 Z + \sum_{i=1}^{n} G_i r_i^2 \ln r_i^2 \tag{3.2}$$

$$z = c_0 + c_1 X + c_2 Y + c_3 Z + \sum_{i=1}^{n} H_i r_i^2 \ln r_i^2, \tag{3.3}$$

where $[X, Y, Z]$ and $[x, y, z]$ are points in source and target data space respectively, and $r_i^2 = (X - X_i)^2 + (Y - Y_i)^2 + (Z - Z_i)^2$. The TPS parameters can be determined if the coordinates of at least four corresponding points are known. When solving for the transform parameters a_i, b_i, c_i, F_i, G_i and H_i for the given point pairs, the following constraints must be also taken into account:

$$\sum_{i=1}^{n} F_i = 0 \qquad \sum_{i=1}^{n} G_i = 0 \qquad \sum_{i=1}^{n} H_i = 0$$
$$\sum_{i=1}^{n} X_i F_i = 0 \qquad \sum_{i=1}^{n} Y_i F_i = 0 \qquad \sum_{i=1}^{n} Z_i F_i = 0$$
$$\sum_{i=1}^{n} X_i G_i = 0 \qquad \sum_{i=1}^{n} Y_i G_i = 0 \qquad \sum_{i=1}^{n} Z_i G_i = 0 \tag{3.4}$$
$$\sum_{i=1}^{n} X_i H_i = 0 \qquad \sum_{i=1}^{n} Y_i H_i = 0 \qquad \sum_{i=1}^{n} Z_i H_i = 0$$

These constraints ensure that the volume splines remain stable under application of point loads (Fig. 3.2).

(a)   (b)
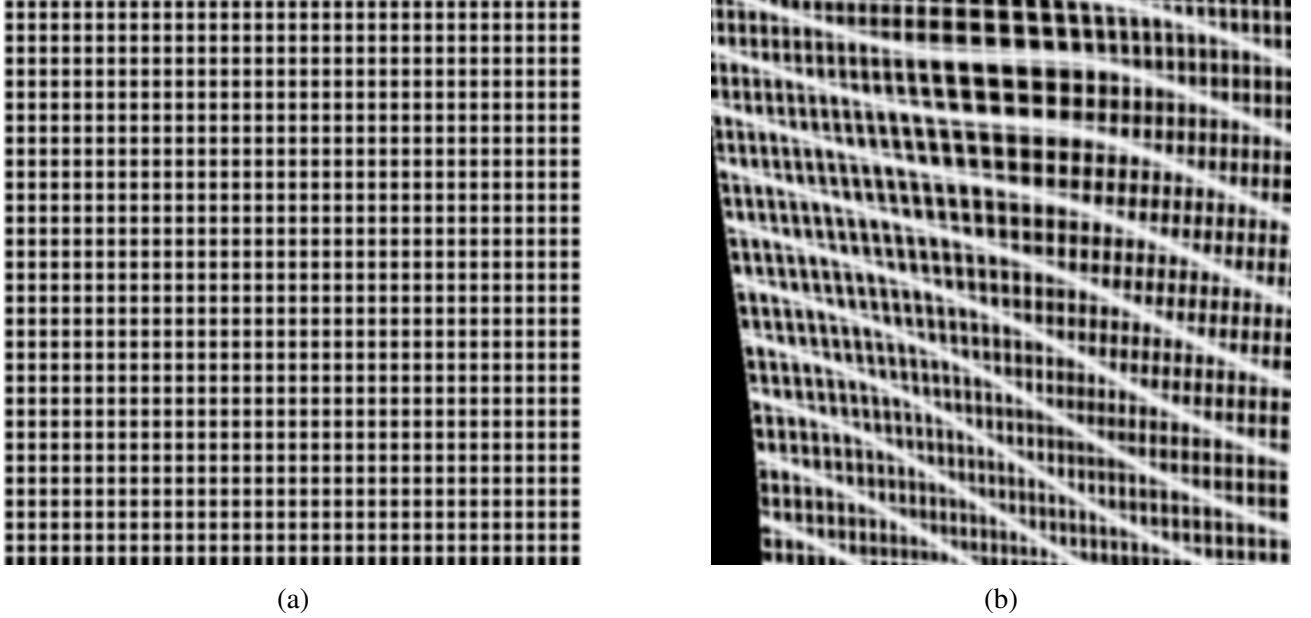
Figure 3.2: *A typical result of the thin-plate-spline warp. (a) A 2D slice through a 3D grid filled with three orthogonal sets of planes, (b) a 2D slice through the warped grid. The third set of planes is not visible in (a).*

3.4.4 Optimization of the Non-rigid Transformation

According to our experience, it is impossible to define appropriate location of the control point pairs only by manual specification of the landmarks. Manual specification usually results only in suboptimal data correspondence after the transformation (Fig. 3.3a). Hence there is a need to optimize the position of the control points in the datasets. A higher number of landmarks that could ensure better initial registration would negatively influence the speed of computations and manual definition of them would be very laborious.

The optimization procedure implemented in the proposed atlas is based on maximizing the mutual information of the transformed and reference datasets. The mutual information I_{AB} represents a measure of the mutual

correspondence of two data sets A and B, by reflecting the number of relevant graphic elements that coincide in both volumes:

$$I_{AB} = \sum_i \sum_j p(a_i, b_j) \log \frac{p(a_i, b_j)}{p(a_i)p(b_j)}, \tag{3.5}$$

where $p(\cdot)$ is the density probability in images A and B respectively and $p(\cdot, \cdot)$ is the probability for the combination of given densities to appear in the corresponding locations in both datasets. All aforementioned probabilities are approximated by means of either 1D histograms or 2D scatterplots. The advantage of the mutual information-based measure is that it abstracts from actual densities and uses only probabilities—thus is not influenced by variable contrast and brightness of the dataset, even does not require the datasets to be of the same modality.

By maximizing the value of I we maximize the above mentioned correspondence between the transformed and reference dataset. Due to the high variability of human body properties we apply Eq. 3.5 only to the subset of the data defined by the bone mask. This decision stems from the observation of larger 'similarity' between human skeletons than between whole human bodies.

A straightforward implementation of the optimization method led to unsatisfactory results. The mutual information function has many local minima because of the 'nearly binary' character of both registered images (caused by data masking through the bone selection mask). To overcome this shortcoming, we have filtered the data by a low-pass Gaussian filter.

In cost optimization it is necessary to evaluate the optimized function many times. Since the computational complexity of the TPS transform is linear both in the number of voxels and the number of control points, one pass of the transformation for a full-sized dataset can take a considerable amount of time and the duration of the optimization would become a problem. Fortunately, sub-sampled datasets and scaled coordinates of landmarks proved to be meaningful and delivered good and stable results in an acceptable time.

The results acquired by the optimized TPS transform on sub-sampled datasets are, although not ideal (Fig. 3.3b), still much better in comparison with unoptimized ones (Fig. 3.3a).

| (a) | (b) |

Figure 3.3: *An overlaid cross-section of warped datasets (a) before and (b) after the optimization.*

3.4.5 Probability Models Derived from the Atlas

The data gathered in the atlas and providing information on average tissue density and average distance to bone surface cannot be used directly for the segmentation of unknown datasets.

Firstly, the information derived from the atlas is specific to the CTA scans of lower extremities. Central parts of long bones are characterized by high tissue density. Therefore bone-tissue histograms of 2D transversal

slices depend on the slice position (Fig. 3.4). This leads to the idea to exploit this dependency for bone tissue segmentation by means of the analysis of spatially dependent histograms. For each slice of the average bone density volume a histogram is built (binned to 256 density levels) and approximated by a modified Gaussian distribution:

$$p_I = \begin{cases} e^{\frac{-(I-\bar{I})^2}{2\sigma^2}} & \text{if } I \leq \bar{I} \\ 1 & \text{otherwise} \end{cases} \tag{3.6}$$

where $\bar{I}$ and σ are mean bone density and its standard deviation within the slice. I is the density of a voxel of the same slice. This formula assumes that bone is the most dense tissue and therefore all voxels with density above the bone average are assigned probability 1.0. Fig. 3.5b shows this probability for all voxels in a transversal slice of one of the datasets used for atlas construction. In comparison to the unmodified image density (Fig. 3.5a), we observe significant enhancement of bone structures and their spatially homogeneous density distribution.

Probability p_I is, however, not sufficient for bone identification in an unknown dataset. It does not eliminate the problem of those no-bone tissues misclassified as bones, which share the same spectral space with bones. A similar situation occurs in brain segmentation, where brain and non-brain tissues share the same density space in a similar way. As a solution, Evans [106] proposed to build a probability atlas by manual segmentation and rigid registration of brains of more than 300 healthy individuals. By averaging binary masks of tissues of interest a probability map was obtained, which was subsequently used in classification as the Bayesian prior. Our situation is different because we currently do not have the sufficient number of datasets in the atlas and also because of the higher variability of bone shapes. Therefore, instead of deriving the presence probability directly from the averaged binary masks, we derive it from the average of distance maps. This significantly blurs the bone masks and thus makes the classification tool less sensitive to the insufficient number of datasets in the atlas (Fig. 3.5c). From the averaged distance map $\bar{D}$ and its standard deviation σ we derive the spatial presence probability (Fig. 3.5d) in point X by

$$p_D(X) = e^{-\frac{\bar{D}(X)^2}{2\sigma(X)^2}}. \tag{3.7}$$

In classification of unknown datasets, we merge both probability measures p_I and p_D into a joint probability $p_{joint} = p_I p_D$, which, after thresholding, results in the final bone mask.

3.4.6 Bone Segmentation Using the Atlas

Segmentation of an unknown dataset by means of the information provided by the atlas requires several steps (see Fig. 3.6).

First, it is necessary to transform the unknown data to the reference atlas frame. Similarly to the atlas construction, we interactively define the set of landmarks, pairwise corresponding to those used for construction of the atlas. Once the transformation is defined, the unknown dataset is transformed to the atlas space and the probabilities p_I and p_D are computed according to Section 3.4.5. Finally, the bone mask is obtained by thresholding the joint probability p_{joint} at level 0.2.

Similarly to the atlas construction, the manually set landmarks result in an insufficient correlation of the dataset to the atlas. However, in this case we do not have the necessary bone masks, which were obtained interactively in the case of atlas construction. Instead, we approximately identify the bone tissue by thresholding the density at a fixed threshold value. We use this mask for optimization of the transformation, in spite of the

| (a) | (b) | (c) |
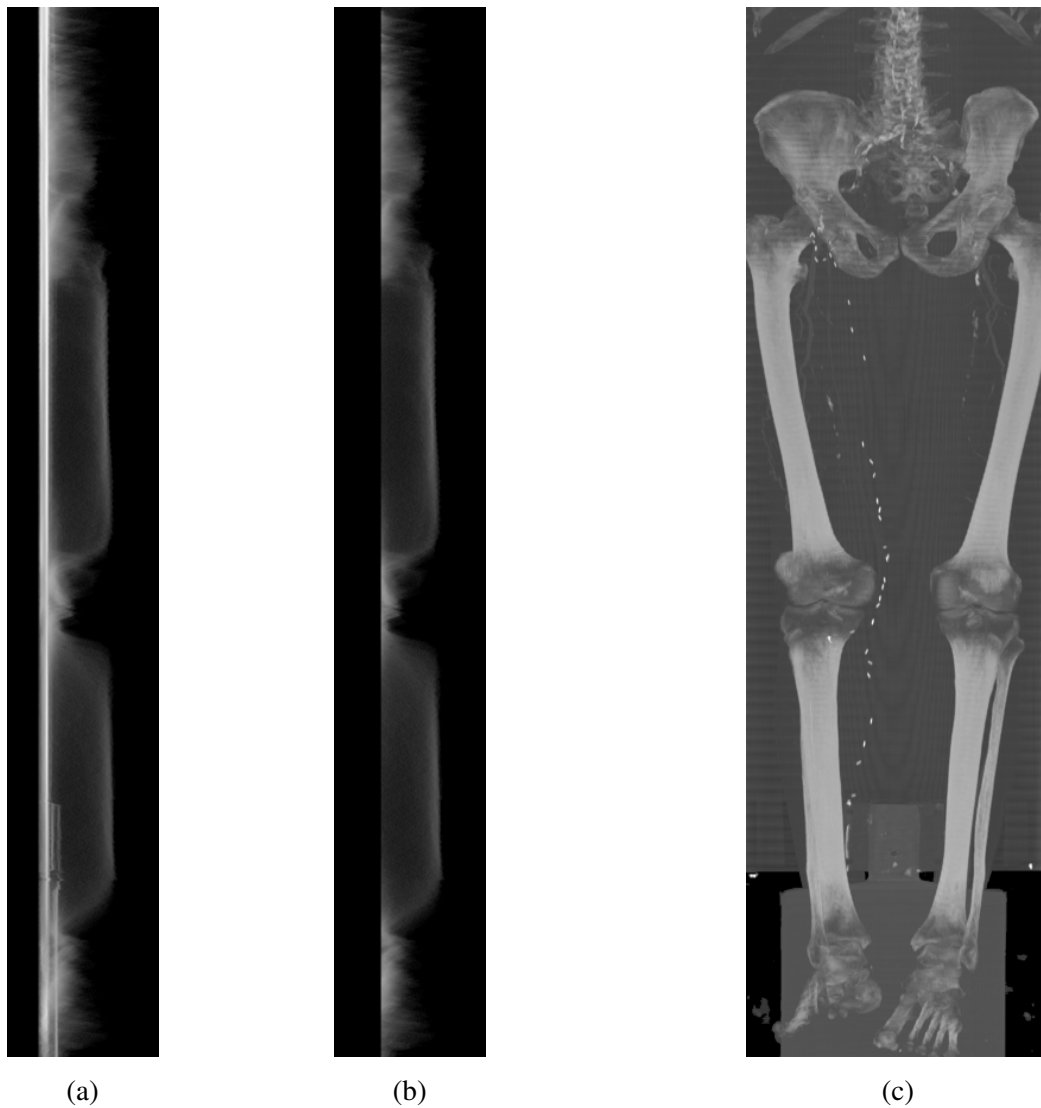
Figure 3.4: *Dependency of density histograms on the slice position. Each row in (a) and (b) shows the histogram of the corresponding slice in a dataset, the MIP of which is presented in (c). (a) shows histograms of all body tissues while (b) only those of segmented bones. (In the histogram, the vertical coordinate is the slice number, the horizontal coordinate refers to density values and brightness in a given point tells the number of voxels in dataset with the given density).*

fact that also no-bone tissues are selected. Since these tissues occupy significantly less space than bones, their influence is suppressed by downscaling the mask and by Gaussian blurring.

3.4.7 Implementation and Results

The algorithm was implemented on an AMD Athlon 1.6 GHz CPU workstation with 2GB of RAM. The addition of a new dataset to the atlas takes about 7 minutes and the segmentation of an unknown patient dataset takes a comparable amount of time. A major problem of the current implementation is its very high memory requirement since for each data voxel ≈ 20 bytes of additional information have to be added. This causes an initially 300–600 MB dataset to grow easily to over 2 GB of needed memory space, which results in memory management problems (the operation system limited us to 2GB address space per task) and rapidly deteriorated

(a)

(b)

(c)

(d)
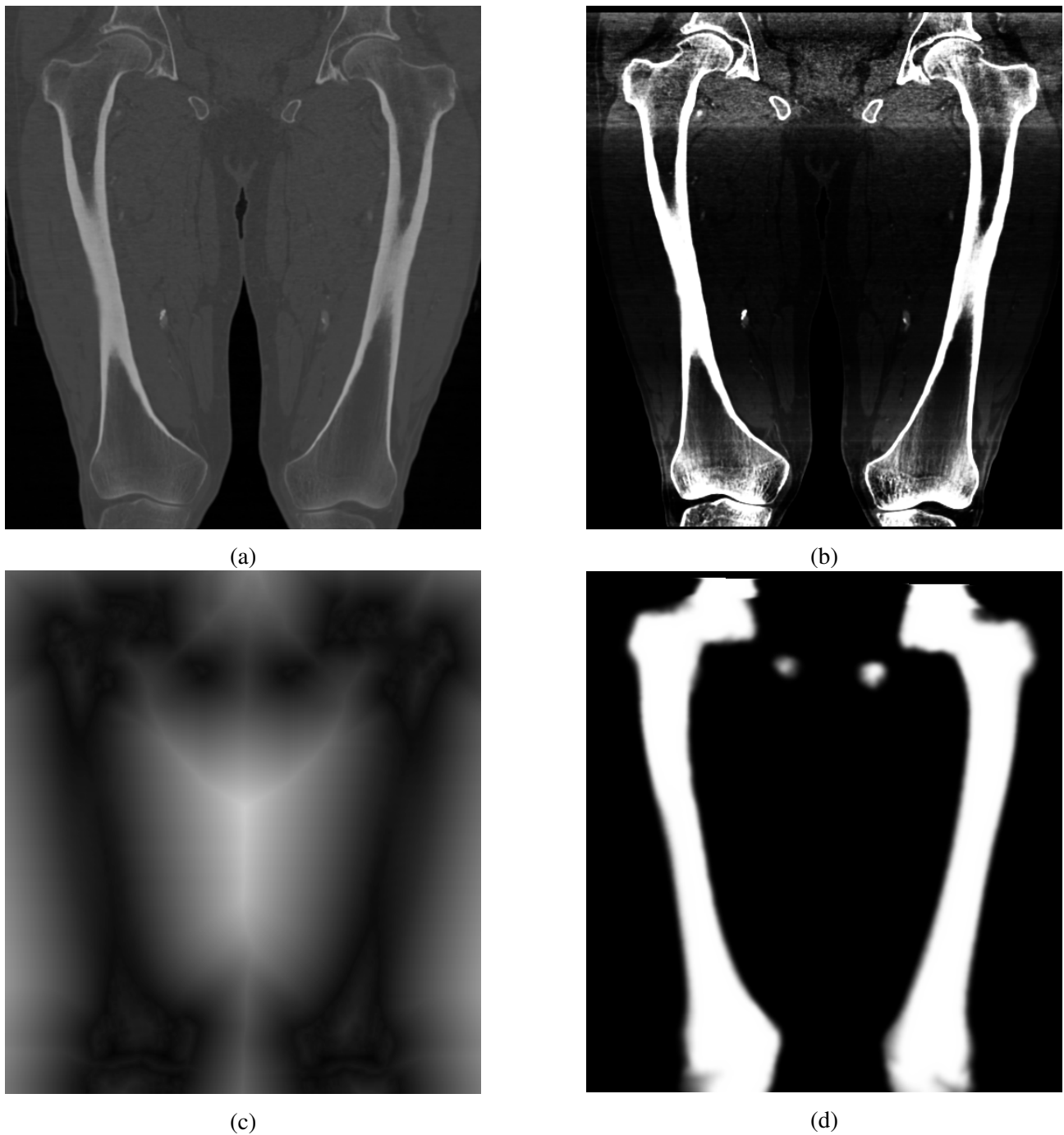
Figure 3.5: *A transversal slice of: (a) the original dataset, (b) probability of bone presence based on the density, (c) distance field showing distance to the average bone surface and (d) spatial probability of the bone tissue.*

the performance of the whole application.

In the future, this problem could be solved by implementing some type of run-time data compression. A CTA dataset typically comprises substantial parts of the data representing uninteresting background (air and parts of the tomograph), which can be easily identified by a low threshold value. A modified version of the run-length encoding scheme, compressing only the background regions at both ends of each scanline, was used
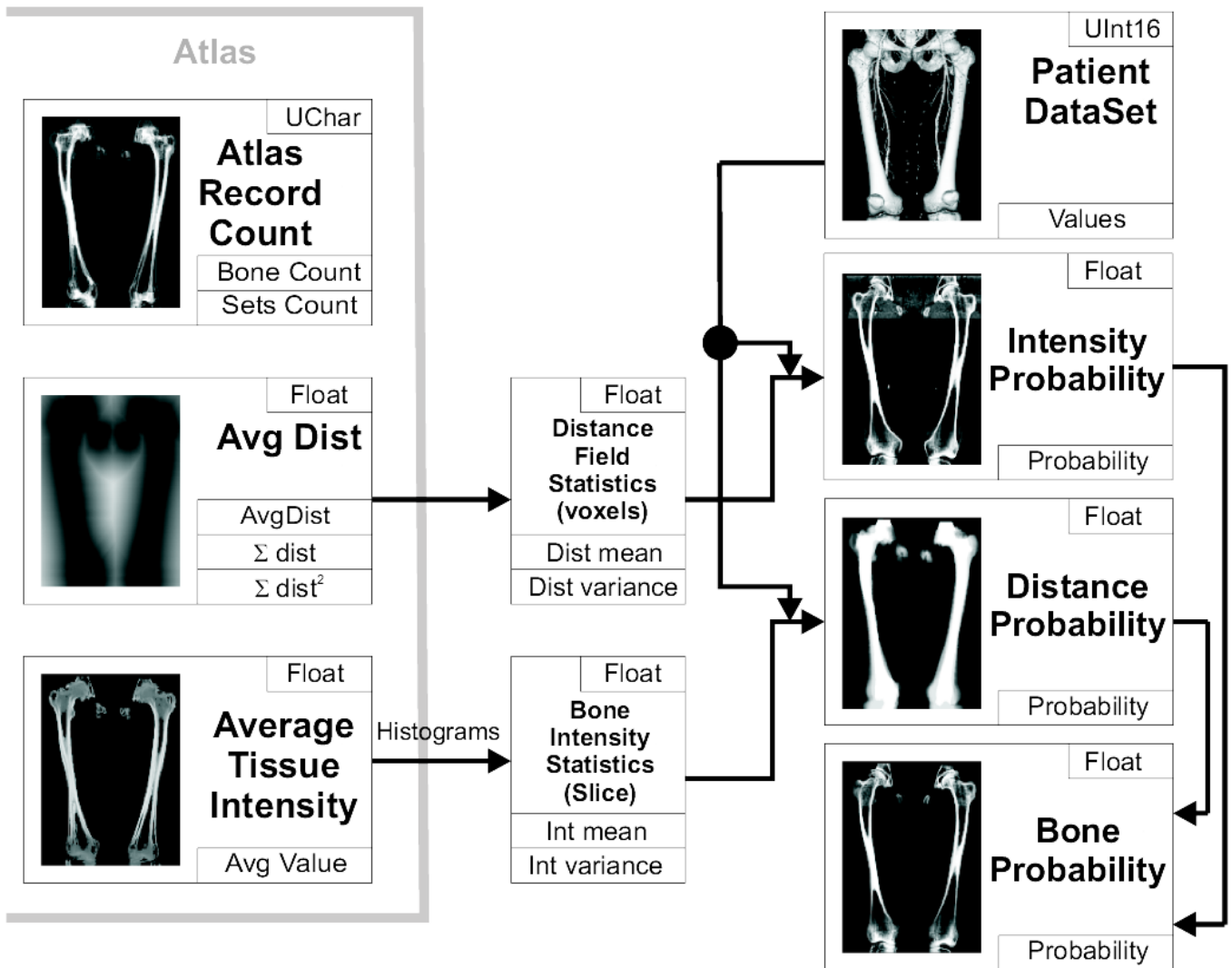
Figure 3.6: *Application of the probability atlas for bone segmentation in pCTA datasets*

for this purpose in the aforementioned segmentation tool [103], saving up to 40% of memory space and could be applied here, too.

Fig. 3.7 shows results of the actual test implementation. Here, only a part of the whole space captured by a CTA-based PAOD study was used to ease and speed up the development. In areas where the bone anatomy does not vary significantly, we get very accurate results. Bone tissue is marked with very high probability, whereas vessels with contrast agent and calcifications are filtered out. On the other side, in regions with significant anatomical variability (Fig. 3.7a), we do not get satisfactory segmentation yet. We partially attribute this to the currently insufficient number of records in the atlas and partially to the low number of control points used to define the TPS warping, rendering it to be not flexible enough.

3.4.8   Conclusion

In this section, we presented an atlas-based approach for segmentation of vascularity of pCTA data. Our assumption that volume elements representing various tissues can be classified by their location and density properties proved to be true in majority. The results of our study show that in case the objects prove suffi-

(a)   (b)   (c)
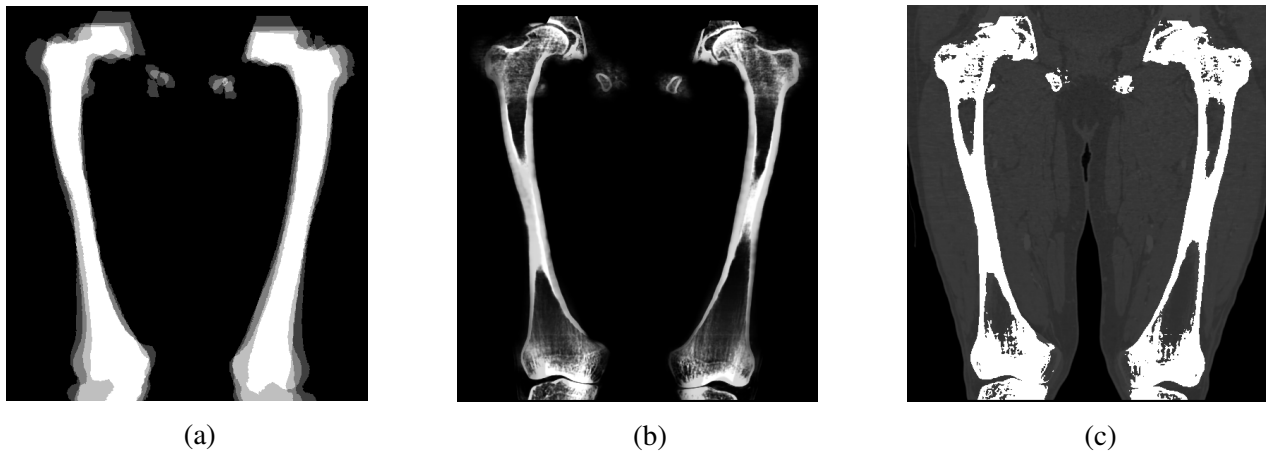
Figure 3.7: *(a) Uncertainty caused by anatomic differences, which are not captured by the TPS transform. Compare the good overlap of the transformed bone masks in the central part of the bone and the not so good one at joints. (b) The joint probability, (c) bone mask obtained from (b) by thresholding.*

cient spatial or density distance they can be identified by the means of probabilistic atlas, requiring only minor operator intervention.

On the other hand, the tissue identification was not complete. We have identified two problems:

- First, in certain areas of patients' bodies the anatomical difference is very high. E.g. the trabecular bone has highly variable density in the knee area. It seems difficult to model the density profile in those areas, what makes this estimation less reliable. Inserting more samples in the atlas might partially solve this problem, but the density distribution needs also to be modeled with a more complex function, to reflect the more potentiall more complex model of density distributions in given anatomic location. Alternatively, if object borders could be detected, then just partial labeling of data would suffice for the identification, as 'the recognizable' part of the object would be identified and this information would be distributed on the whole object to achieve segmentation. And

- Second, the bone shape variability among the patients is also very high. Simple registration with low number of landmarks leads only to an approximate alignment, not capturing smaller anatomical differences. In case these differences are larger then distance of the two distinctive tissues (bone vs. vessel) then the atlas classification fails. This issue can be solved by more precise registration employing higher number of landmarks. The drawbacks are then the higher computational costs and more extensive operator intervention. The number of necessary landmarks depends on required quality and complexity of objects' shape and is a research task of itself.

The first problem could be partially addressed by incorporating a technique that extracts borders of objects. One of the possible approaches—the watershed transform—is described in next section.

Other inherent problem of the atlas approach—if applied to pCTA data—is its computational complexity, leading to several hours long computation on actual PCs (Pentium IV 2GHz, 2GB RAM). The time requirements can be mostly attributed to the TPS warping applied to such large datasets. As other warping methods are comparatively complex, we see a possible solution in a more powerful computer and parallelisation of the task, e.g. on multi-processor cluster, etc.

3.5   Probabilistic Atlas Combined with Watershed Transform

As described in Subsection 3.4.8, the segmentation based on a probabilistic atlas fails in areas, where spatial variability is very large. This problem could be addressed, if regions' (closed) borders could be identified. Thus, having a reliable classification for only a part of a region this information can be extenden over the whole region. The influence of high spatial variability would be then suppressed, as only the 'constant' parts of an object will be identified, distributing later this classification over the whole object. Such border information is derived by evaluation of gradient-magnitude maxima in the data and one of such techniques is also the watershed transform.

Watershed Transform (WT) is a morphological gradient-based technique whose basic principle was described in Subsection 3.3. Two basic classifications of the watershed algorithm implementation exist: *shortest topological distance*, based on paths of steepest descent terminating in local minima (Meyer [107]) and *immersion algorithms* (Vincent and Soille [51]). WT is able to segment unknown datasets, locating objects' borders in areas of gradient-magnitude maxima. Thus, homogeneous areas are separated. The WT is known to work also in areas, where only weak edges appear. Its main drawback is the problem of oversegmentation. This problem can partially suppressed by 'preflooding', by hierarchy of watersheds or other post-processing and merging of the regions (Meyer and Beucher [108], Lotufo and Silva [109], Beucher [110]).

Due to the local gradient-magnitude maxima properties, the WT tend to group voxels that morphologically belong together. In this way, the algorithm does not depend on density values. The size of regions and its borders depends on actual data and noise within. To select proper size of the regions and therefore to select only relevant borders various techniques were proposed. In Šrámek *et al.* [111] the authors suggested to low-pass filter the data (e.g. by means of a Gaussian filter) and thus reduce the number of unimportant details, resulting in reduced number of regions. The disadvantage of this approach is that the borders of the regions shift (due to the nature of low-pass filtering) and become imprecise. Hierarchical merging of regions has been suggested as a solution in this case. Alternatively, regions can be merged based on their statistical attributes (e.g. mean value, variation, etc.); eventually both techniques can be combined.

By combination of results of the probabilistic atlas with the regions acquired through WT, more precise segmentation can be achieved. Individual voxels can be labeled by the atlas and then whole regions containing these pixels can be labeled also. Thus, also other voxels that belong morphologically to the given object, but failed to be classified in the previous step can be correctly identified.

On the other way round, an atlas can help in solving the oversegmentation problem, where the merging of adjacent regions is the main challenge. With application of the atlas described in Section 3.4, it is possible to find out which regions belong to the same object.

In [112], we suggested to combine the probabilistic atlas and regions acquired through WT, to overcome the problem of imprecise segmentation that resulted from application of atlas with low number of landmarks.

3.5.1   Extension of Atlas Segmentation by Watershed Transform

First, a watershed transform of the particular dataset must be computed. In our case, the simple hierarchical merging (based on Gaussian filtering) led either to omitting of important details (in case when the top of the hierarchy was heavily filtered) or the oversegmentation was not suppressed enough. Therefore, we included region merging based on the density mean-value difference. We merged regions that differed no more than 10 HU (Fig. 3.8b) in several iterations (consecutively increasing the threshold from 1HU to 10HU). Next,

<center>(a)   (b)   (c)</center>
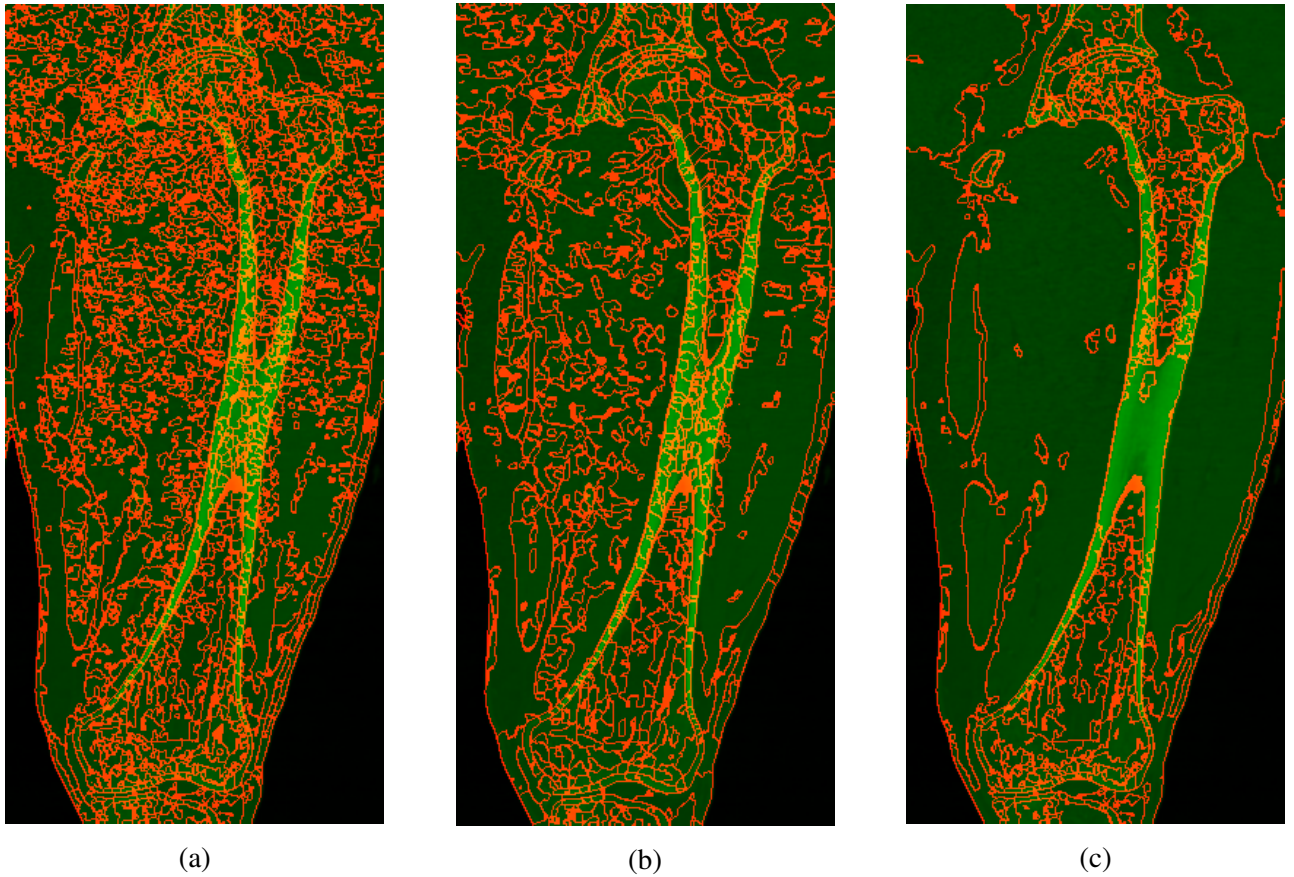
Figure 3.8: *Watershed transform and merging of the segmented regions. (A cut-out from vertical slice of a 3D data in area of a hip-joint). (a) Oversegmentation is characteristic for a plain watershed transform. (b) Suppression of oversegmentation by merging of regions based on mean-density similarity. (c) Suppression of oversegmentation achieved by combination of mean-density similarity and hierarchical merge.*

we applied the hierarchical merging, which kept the region borders at their original, not-filtered position but decreased the number of regions (Fig. 3.8c).

Then, to improve the results acquired by application of the probabilistic atlas approach we incorporated edge information obtained with the 3D watershed transform into the final bone classification. In each watershed region we computed the number of voxels, which were labeled as bone in the probabilistic mask. If the number of labeled voxels in a region exceeded a specified threshold (e.g. 10%), we labeled the whole region as bone (Fig. 3.10).

These results are satisfying if we need to identify objects for e.g. surface-shaded visualization (Fig. 3.11a). The fact that the borderlines follow the areas of the gradient-magnitude maxima can cause that due to PVE there might be residual voxels not identified as bone in the datasets and in case of maximum-intensity-projection (MIP) this might cause artifacts (Fig. 3.9c). Therefore, we dilated the bone in final stage, with a $5\times5\times5$ structuring element (Fig. 3.9d).

3.5.2 Implementation and Results

The presented technique shows a way to segment bone tissue in CTA datasets more precisely. Compared to simple threshold-/gradient-based algorithm it delivers much better results (Fig. 3.11). To apply the aforementioned
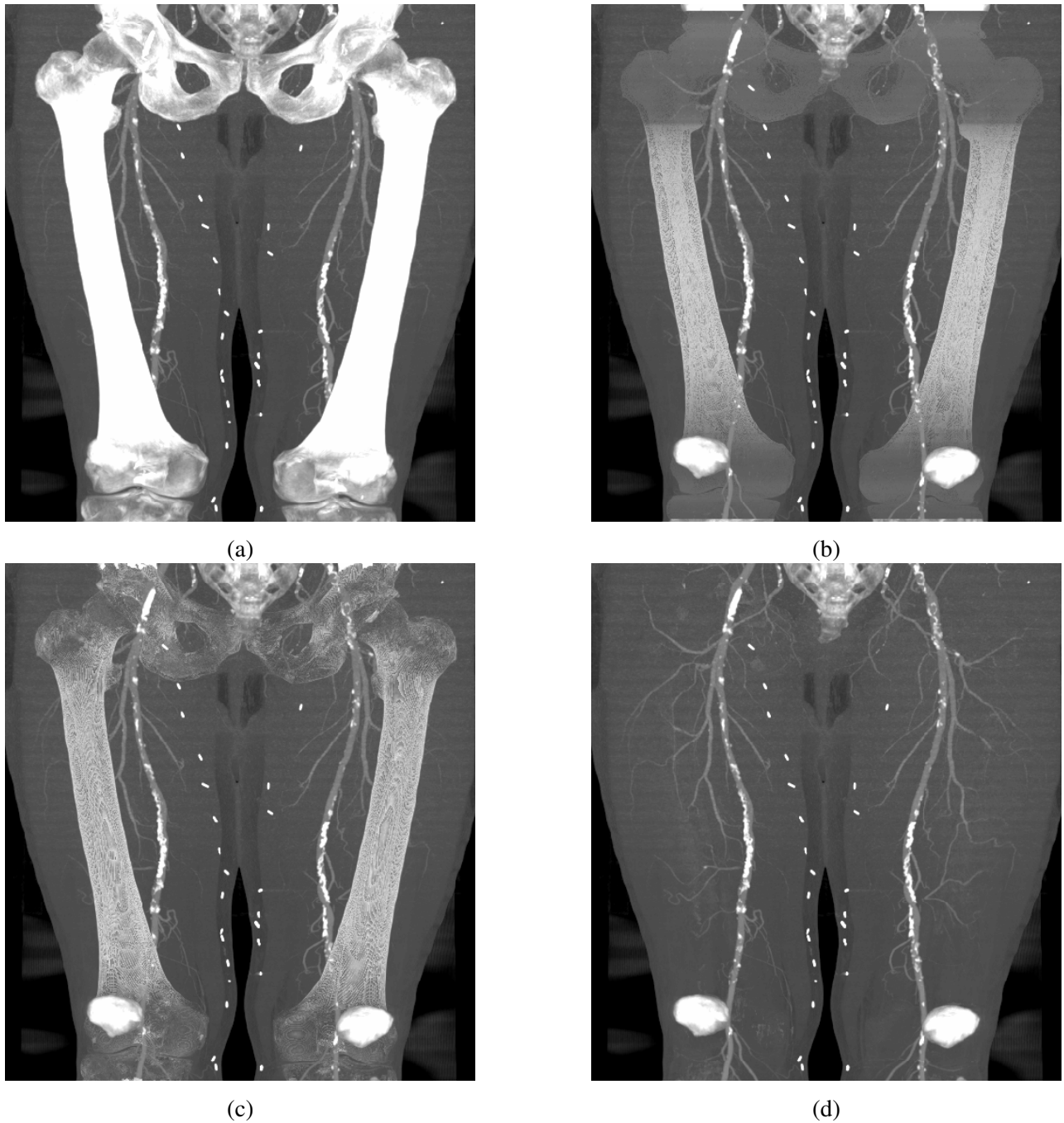
Figure 3.9:   *Application of watershed transform combined with the probabilistic atlas for segmentation. (a) Maximum-intensity projection (MIP) of the dataset, (b) MIP of the dataset where the bone tissue was partially out-masked by probabilistic atlas segmentation, (c) MIP of the dataset where the bone tissue was out-masked by means of the probabilistic atlas combined with watersheds, and (d) MIP of the dataset where the bone tissue was out-masked by application of probabilistic atlas, watershed transform and bone mask dilation. (The patella and sacro-coccygeal bone were not modeled.)*

technique, first building of a density probability atlas is needed (Section 3.4). Region growing with threshold is used to separate different object in the probability volume. In parallel, 3D watershed transform is applied to the unknown dataset to obtain edge information. In the end, watershed regions are classified according obtained

(a)   (b)   (b)
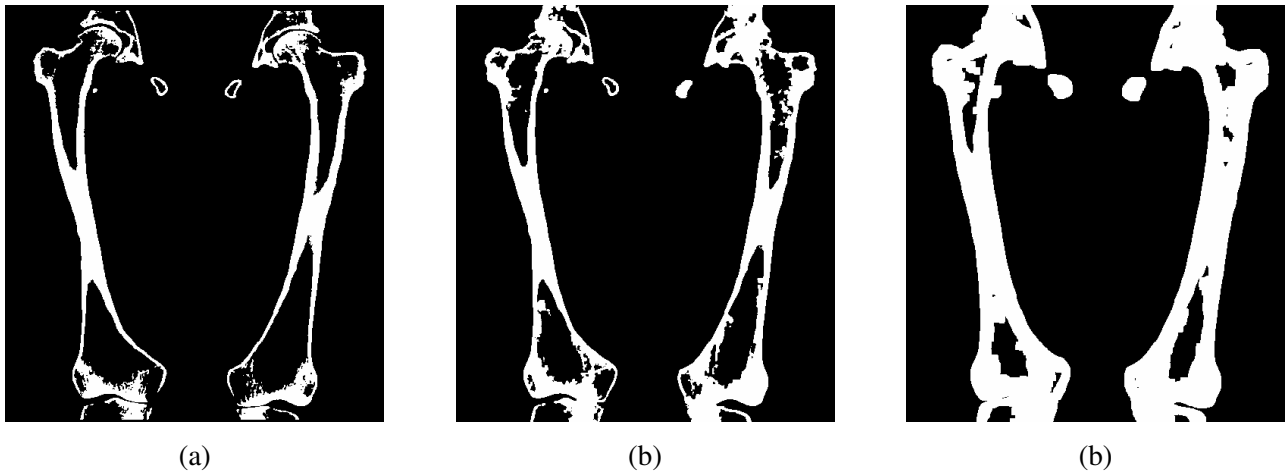
Figure 3.10: *Bone tissue masks (vertical slices from mask volumes). (a) Bone tissue mask acquired by application of probabilistic atlas; (b) Bone tissue mask acquired by extending of (a) by watershed transform regions; (c) Bone tissue mask acquired by morphologic dilation of (b).*

bone mask. Determination of algorithm constants is quite self-explaining and straightforward. The threshold for region growing should express a probability in volume resulting from atlas application. The higher value, the lower is the probability that the region growing will grow to incoherent objects, but also some voxels remain unlabeled, therefore missing in final mask. In our case, values approx. 0.7–0.8 for the probability proved to be suitable. The threshold determination for watershed region classification according the bone mask is even simpler. In a fact, even region with only one voxel labeled as bone can be considered as bone region. To be on a safe side, we used threshold about 10%. Need to be mentioned that both thresholds are partially tied together, so when choosing lower region growing threshold one should consider higher value for region classification. But these values are not crucial for algorithm results. Parameters of 3D watershed transform (kernel size of the Gaussian filter, levels of hierarchy, threshold for watershed region mean-value merging) are determined depending on the input data and required precision [6]. The aforementioned methods were implemented on a PC workstation with 1,6GHz CPU and 2GB of RAM. Processing of a 512×256×512 voxel dataset needed 90 seconds for watershed labeling, 5–6 minutes to create an object map and 4–5 minutes to process density similarity merging of regions. Other tasks were computed in a time comparable with data loading/saving time (4–5 seconds for loading, 15–20 seconds for saving.) The memory requirements were approx. 150MB for the dataset and additional 600 MB (gradient image, object map) for processing. An example of achieved segmentation results is presented in Fig. 3.11. The difference between mask obtained with probability atlas and mask extended with 3D watershed transform is not visible in MIP images (Fig. 3.9). However, there is visible difference in the knee area in Fig. 3.10a and Fig. 3.10b (compare areas of trabecular bone).

3.5.3   Conclusion

In this section, we presented an extension to the probabilistic atlas approach, by combining it with the watershed transform. As the results show, the segmentation is more precise. Classification of voxels inside the watershed regions through the probabilistic atlas and the extending this segmentation to all regions' voxels makes the segmentation step more reliable.

However, implementation of the proposed algorithm in clinical environment is hampered due to two draw-

| (a) | (b) |
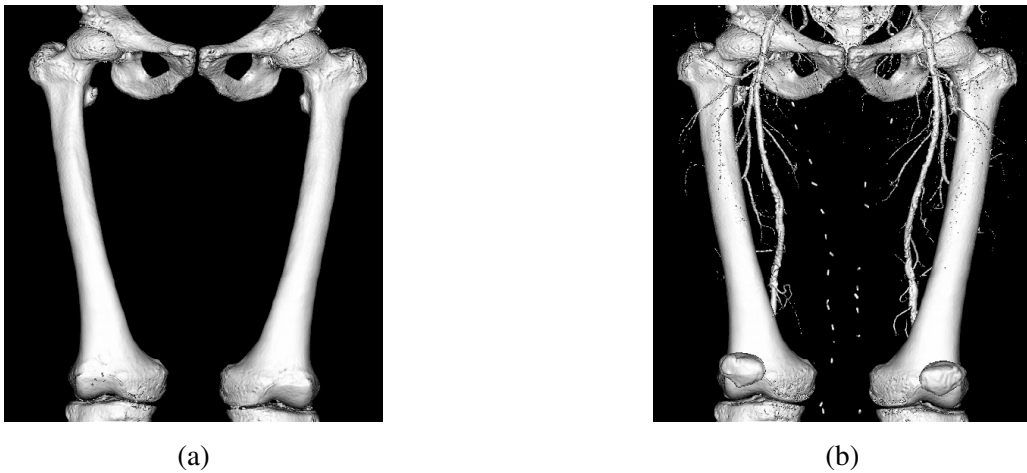
Figure 3.11: *Atlas+watershed vs. plain segmentation. (a) Bone segmentation by means of probabilistic atlas combined with watershed transform, (b) Bone segmentation by means of plain thresholding (th = 200 HU).*

backs:

- The first is the speed of the proposed technique and its memory requirement. The watershed transform of a full-sized dataset takes ≈60 min on our 1,6GHz CPU workstation. Also the post-processing of watershed regions and their merging is a heavy computational burden. Therefore, the proposed technique is more a proof-of-a-concept then a really applicable approach,

- The second is segmentation of different tissues that lie in very close vicinity. The combination of atlas and watershed transform solved the problem of identification of tissues in areas, where their density or spatial properties vary significantly. On the other side, is has less effect on problem of segmentation of various tissues that posses the same density range and the same spatial location (e.g. in popliteal area). Due to the very high spatial variability in this area and similar density properties of the objects the atlas becomes imprecise and application of watershed transform does not help, as the individual regions (not only voxels) are misclassified in the atlas stage.

To overcome this, a measure distinguishing vessel and non-vessel tissue, regardless of its location and density is needed. A well-known approach providing such information is enhancement of cylindrical structures, described in next section.

3.6   Enhancement of Cylindrical Structures

The results achieved in our previous research and also the results achieved by others led us to an idea, that the S&C of the pCTA data cannot be based on individual voxels or regions. Voxels or unstructured regions do not exhibit features attributes for determination of their type. Therefore, some pre-knowledge has to be brought in the S&C process, for the computer to 'understand' the data. This challenge was partially addressed in the proposed atlas approach, where the deformable atlas contained information where the bone tissue 'can appear'. Due to the highly complex shape of the bones and joints and also due to significant density and spatial difference, the achieved results were suboptimal.

A complementary approach is to detect the vessel tissue, not the bone tissue. Reviewing the tissue properties described in Section 2.4, it can be observed that the vessel tree hierarchy is highly variable in space; but on the other hand, the shape of the vessel segments is quite simple; basically these are curved cylinders of various

diameter (if not taking the bifurcations into account, for simplicity reasons). Then, for vessel identification algorithms for *enhancement of cylindrical structures* can be used. These segment (or more properly: *amplify*) structures in the dataset based on their shape, rather than on their density properties. Such methods typically evaluate directional distribution of voxels with similar densities in 3D space by means of statistical and matrix computations.

Eigensystem analysis-based Segmentation and Classification

Eigensystem analysis-based methods take advantage of the observation that objects of particular shapes prove distinct density changes in different directions (for a selected scale). Namely:

- *Planar structures* or *sheet-like tissues* manifest small density changes in two directions (directions defined by the orientation vectors of the plane) and significant density change in the third direction (direction parallel to the normal vector of the plane)
- *Cylindrical structures* show small density change in the direction of the cylinder axis and significant density change in other two directions (perpendicular to cylinder axis—in the direction of vectors defining the cross-section plane of the cylinder)
- *Spherical structures* or *blobs* show significant difference in density in all three directions.

If there are only small density changes in all three directions, homogeneous areas are detected. The small density changes are then given only by noise. Algorithms evaluating such density changes are typically based on eigensystem analysis of a matrix whose elements are determined by density changes in directions given by the coordinate system. Two similar mathematical concepts are used: Hessian Matrix and Structure Tensor filtering.

Hessian Matrix-based Enhancement of Cylindrical Structures

The Hessian matrix-based enhancement of cylindrical structures was investigated in the work of Sato *et al.* [113], where the approach was proposed for enhancement of vessels in MR datasets. The results were thresholded for further processing. This approach was also integrated in the work of Frangi *et al.* [114] where the results were directly visualized, in Krissian *et al.* [115] where the resulting height ridges were traversed and evaluated and in Lorenz *et al.* [116] where the results underwent active contour segmentation. The basics of this algorithms are the following:

Lets have a 3D volumetric data I and second partial derivative of the Gaussian function G in coordinate directions i and j in a given point p_0. Then, by convolution of it with the data we get function H_{ij}:

$$H_{ij}(p_0) = \frac{\partial^2 G(p_0, \sigma)}{\partial i \partial j} * I(p_0), \tag{3.8}$$

where

$$G(p_0, \sigma) = \frac{1}{\sigma\sqrt{2\pi}} e^{-\frac{p_0^2}{2\sigma^2}}. \tag{3.9}$$

Following, the Hessian Matrix is defined as:

$$H(p_0) = \begin{pmatrix} H_{xx}(p_0) & H_{xy}(p_0) & H_{xz}(p_0) \\ H_{xy}(p_0) & H_{yy}(p_0) & H_{zz}(p_0) \\ H_{xz}(p_0) & H_{yz}(p_0) & H_{zz}(p_0) \end{pmatrix}. \tag{3.10}$$
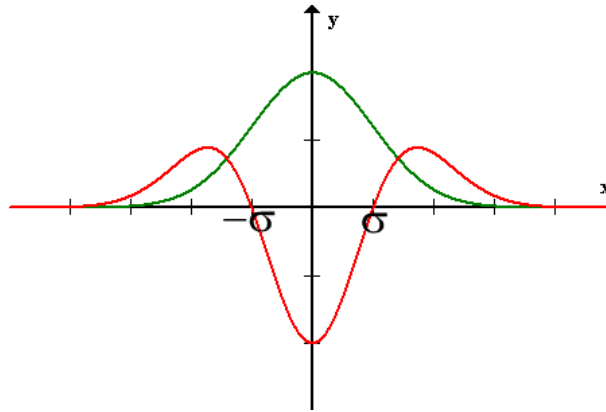
Figure 3.12: *Gaussian function (green) and its second-order derivative (red) for given parameter σ. The second-order derivative is used in the Hessian matrix-based methods as a convolution kernel for detection of structures of size σ.*

The above mentioned defines the Hessian Matrix as a matrix of convolutions of the original data I with second-order derivatives of the Gaussian function with parameter σ. The second order derivative of the Gaussian is a 'Mexican-hat' shaped function (Fig. 3.12). After convolution of the data with this function, objects of size close to σ are enhanced, whereas objects of other sizes are suppressed (Fig. 3.13a, b and c).

In eigensystem decomposition of the H matrix, the eigenvalues then represent the density change in directions given by eigenvectors of the matrix. Hence, by analyzing the eigenvalue magnitudes and their mutual relationship, the type of an object can be derived with the help of eigenvectors and their orientation in the original coordinate system. Considering λ_1, λ_2, λ_3 to be the eigenvalues of the matrix H with $|\lambda_1| \geq |\lambda_2| \geq |\lambda_3|$ and e_1, e_2, e_3 to be the corresponding eigenvectors, information about structure types can be derived, as denoted in Tab. 3.1. The shape enhancement is then achieved by comparison of these eigenvalues. We define

λ_1	λ_2	λ_3	Structure Type
+H	+H	+H	Bright blob-like structure
+H	+H	±L	Bright cylinder-like structure, e_3 is axis of the cylinder
+H	±L	±L	Bright sheet-like structure, e_1 is normal vector of the plane
-H	-H	-H	Dark blob-like structure
-H	-H	±L	Dark cylinder-like structure, e_3 is axis of the cylinder
-H	±L	±L	Dark sheet-like structure, e_1 is normal vector of the plane
±L	±L	±L	Homogeneous (noisy) area

Table 3.1: *Type of structures identified in data by eigenvalue analysis. $|\lambda_1| \geq |\lambda_2| \geq |\lambda_3|$ are the matrix eigenvalues and and e_1, e_2 and e_3 are eigenvectors corresponding to the eigenvalues. +H denotes large positive eigenvalue, -H large negative eigenvalue and ±L small eigenvalue. What is 'large' and 'small' depends on type of data and its contrast.*

$$N = \sqrt{\lambda_1^2 + \lambda_2^2 + \lambda_3^2} \qquad (3.11)$$

as a 'norm' of the eigenvalues, i.e. describing the contrast of the structures, distinquishing noise and regular
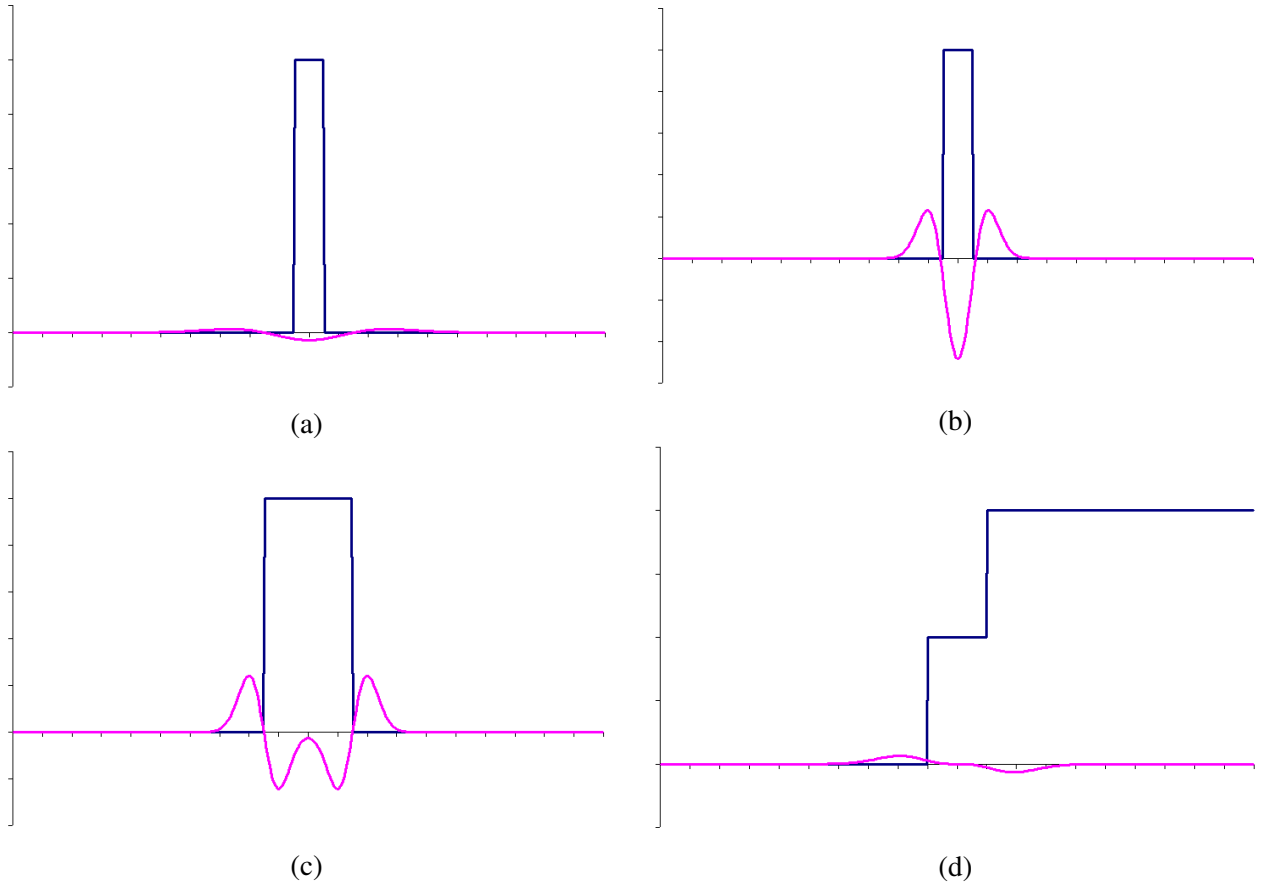
Figure 3.13: *Enhancement of cylindrical structures by means of the Hessian matrix-based filtering. Black: box function simulating vessel cross-section density profile, magenta: filter response (convolution of original data with second-order kernel). (a) If filter size σ is much larger then the object, enhancement is small; (b) maximum enhancement is achieved when filter σ and object size are equal; (c) if object size is larger then the filter σ, enhancement diminishes again. (d) Application of the filtering on a staircase function (simulating a vessel bordering both with soft tissue and bone). Even if the object size and filter size σ are similar, the enhancement is low and has variable sign.*

objects, and

$$C = \frac{|\lambda_2|}{|\lambda_1|} \tag{3.12}$$

as a measure of cylindricity of structures in the data. C is close to 1 for cylindrical structures and close to 0 for non-cylindrical objects. (The ratio $|\lambda_2|/|\lambda_1|$ remains always limited, as $|\lambda_1| \geq |\lambda_2|$). In the work of Sato [113] and Frangi [114] also modified measures for cylindricity were proposed, resulting in better enhancement for their MRA data.

To enhance cylindrical objects of various size, filtering in multiple scales must be employed (the scale-space approach [117]). The output of individual multi-scale stages must be normalized, as for different scales the level of enhancement if a function of σ.

Proof: assume $p_0 = 0$, object density $D = 1$ for $p \in (-\sigma, \sigma)$ and $D = 0$ for $p \notin (-\sigma, \sigma)$, thus we integrate the Hessian function over an interval $(-\sigma, \sigma)$:

$$H_{ij}(p_0) = \frac{\partial^2 G(p_0, \sigma)}{\partial i \partial j} * I(p_0) = \int\limits_p \frac{\partial^2 G(p - p_0, \sigma)}{\partial i \partial j} I(p) \mathrm{d}p = \left[\frac{1}{\sigma\sqrt{2\pi}} e^{-\frac{(p-p_0)^2}{2\sigma^2}} \left(-\frac{p - p_0}{\sigma^2} \right) \right]_{-\sigma}^{\sigma} = -\frac{2}{\sigma^2\sqrt{2\pi}} e^{-\frac{1}{2}}.$$

The results of the multi-scale filtering therefore have to be weighted by σ^2 to be comparable in magnitude. This concept was extended by Lindeberg [118], [119]: if ϱ is the response resulting from Hessian filtering and ϱ_σ is the response with application of σ, then the 'normalized' response ϱ is derived by:

$$\varrho = \sigma^\gamma \varrho_\sigma. \tag{3.13}$$

The parameter γ needs to be tuned to achieve best results or can be used to prefer particular scales.

Structure Tensor-based Enhancement of Cylindrical Structures

Structure tensor was introduced to volumetric data processing by Knutsson [120] and later studied in Hladùvka [121]. For 3D volume data I it is defined as:

$$H(p_0) = \int\limits_p w(p - p_0) \begin{pmatrix} \frac{\partial I(p)}{\partial x}\frac{\partial I(p)}{\partial x} & \frac{\partial I(p)}{\partial x}\frac{\partial I(p)}{\partial y} & \frac{\partial I(p)}{\partial x}\frac{\partial I(p)}{\partial z} \\ \frac{\partial I(p)}{\partial x}\frac{\partial I(p)}{\partial y} & \frac{\partial I(p)}{\partial y}\frac{\partial I(p)}{\partial y} & \frac{\partial I(p)}{\partial y}\frac{\partial I(p)}{\partial z} \\ \frac{\partial I(p)}{\partial x}\frac{\partial I(p)}{\partial z} & \frac{\partial I(p)}{\partial y}\frac{\partial I(p)}{\partial z} & \frac{\partial I(p)}{\partial z}\frac{\partial I(p)}{\partial z} \end{pmatrix} \mathrm{d}p, \tag{3.14}$$

where $\frac{\partial I(p)}{\partial x}$, $\frac{\partial I(p)}{\partial y}$ and $\frac{\partial I(p)}{\partial z}$ can be approximated by e.g. convolution of the data I with the first order derivative of the Gaussian function:

$$\frac{\partial I(p)}{\partial x_i} = \frac{\partial G(p, \sigma_d)}{\partial x_i} * I \tag{3.15}$$

if G is defined by Eq. 3.9. The σ_d is defined by the noise-reduction properties and is usually small.

The Structure tensor itself is a matrix of integrated border information. Elements of the matrix incorporate information about the gradient value combinations in individual directions weighted by some scale-space selecting function $w(\cdot)$. Thus, it integrates the border presence information. Important is the weighting function $w(\cdot)$ as it defines the how the border information is weighted. For processing of volumetric datasets, it can be defined e.g. by the standard Gaussian function:

$$w(p - p_0) = G(p - p_0, \sigma_w), \tag{3.16}$$

where the σ_w parameter steers the area over which is the border information integrated (the scale-space) and generally is equal to the size of objects to be identified. The Structure Tensor matrix is then also eigen-decomposed and the results are interpreted equally as in case of the Hessian Matrix.

Properties of the Eigensystem-based Cylindrical Structures Filtering

The magnitudes of the particular eigenvalues in Hessian matrix-based or Structure tensor-based filtering are determined not only by the shape of the object, but simultaneously also by the local contrast. Therefore, brighter objects prove higher absolute enhancement than less bright objects. E.g. less contrasty cylinders manifest smaller response then much brighter objects of non-cylindric shape. This limits direct usage of these methods for vessel enhancement in pCTA data, because the vessels are often not the brightest structures (the

bones are) and vessels often touch bones (refer to Fig. 3.13d), what misleads the algorithm. Therefore, the magnitude of eigenvalues does not provide reliable information as the vessels are not local density extremes, but present only intermediate values between densities of soft tissue and bone. In this setting, the convolution with the 'Mexican hat' filter does not bring predicable results, as the enhancement depends also on the mutual relations of the values constituting the object. On one border, the vessel is positively enhanced (being a very local density maximum) and on the other negatively enhanced (being a very local minimum). Additionally, the enhancement maxima in pCTA data do not indicate centres of cylindrical structures, because the structures are inhomogeneous.

Nevertheless, the orientation information (the eigenvector related to eigenvalue with the smallest magnitude) provided by these methods, according to our research, is quite stable and reliable. As long as the size parameter σ for both algorithms is sufficiently close to size of the sought object, the object orientation can be reliably derived. This property can be very useful for further pCTA data processing, as it allows stable, reliable and unsupervised estimation of vessel orientation (see examples in Figures 3.22–3.25).

Comparing the computational efficiency of the two presented approaches, computation of the Hessian matrix requires 6 filtering passes, whereas the Structure tensor requires $3 + 6 = 9$ filtering passes. Additionally, the Hessian matrix-based filtering efficiently suppresses noise (structures much smaller then selected object size), whereas the Structure tensor enhances potential gradients close to the center of the weighting function and therefore is less usable for noisy datasets (e.g. for CT dataset with artifacts due to presence of metalic implants).

3.6.1   Model-Based Identification of the Vessel Tissue

According to our research, four types of information could be derived from volumetric data:

- density or gradient information,
- spatial location of structures in the data,
- object shape information, and
- texture or frequency information.

Since the density and spatial information is not always sufficient for the vessel segmentation (as discussed in previous subchapters) and there is no significant texture information within the vessel or bone objects, shape model is the only remaining information that can be exploited.

In a shape-based segmentation, the cylindricity of the vessels is used as a criteria for classification. The tubular shape property of the vessels comes from the hydrodynamic pressure, because the blood pressure is equal in all directions. When the vessel is healthy, the flexibility of the vessel wall is equal around the cross-section and the vessels hold the shape of a curved cylinder, with decreasing diameter further from the heart.

In the shape-based or model-based segmentation, valid shapes must be recognized and then parameters of the object must be derived, or pre-defined model must be matched and compared. In pCTA data, an exact predefined model (with precisely given parameters) is not applicable, as the orientation, diameter and densities are not known, or known only approximately. Therefore, structures that fulfill cylindricity criteria must be selected and precise shape of the structures must be then evaluated. The global cylindricity criterion is given by the distribution of voxels with distinct or similar density around the object centre, as discussed in Section 3.6.
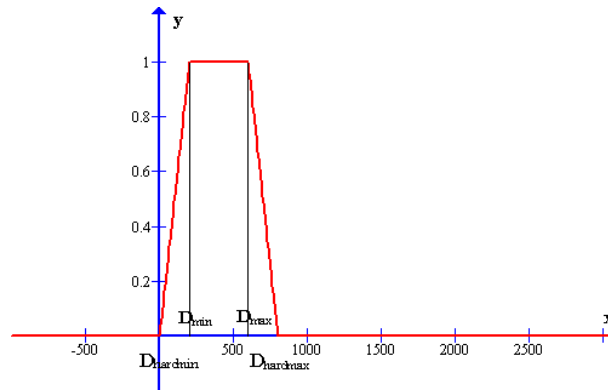
Figure 3.14: *Function for mapping tissue densities to vessel probability (see text). Horizontal axis: densities in HU, vertical axis: vessel-density probability.*

Hessian Matrix-based Enhancement of Cylindrical Structures in pCTA Data

As discussed in previous sections, Hessian matrix-based filtering cannot be directly applied to pCTA data to enhance vessels, due to two main problems: i) the vessels are not always the brightest/darkest structures, and ii) the high variability of densities belonging to vessel tissue (contrast agent, soft plaque, calcifications . . .) make the enhancement uneven. To overcome these problems, we suggested to remap densities in the dataset to vessel probability with a simple trapezoid function:

$$
p_v(x) = \begin{cases}
0 & \text{if } D(x) < D_{hardmin} \text{ or } D(x) > D_{hardmax} \\
1 & \text{if } D(x) > D_{min} \text{ and } D(x) < D_{max} \\
f_1(D(x), D_{hardmin}, D_{min}) & \text{if } D(x) > D_{hardmin} \text{ and } D(x) < D_{min} \\
f_2(D(x), D_{max}, D_{hardmax}) & \text{if } D(x) > D_{max} \text{ and } D(x) < D_{hardmax}
\end{cases} , \qquad (3.17)
$$

where $D_{hardmin}$, D_{min}, D_{max} and $D_{hardmax}$ are the thresholds identifying vessel densities in the dataset and f_1, f_2 are linear mapping functions. An example of such function is presented on Fig. 3.14. Applying such mapping, structures with densities similar to vessels are enhanced and most vessels become the brightest structures (Fig. 3.15).

After this density remapping, enhancement of tubular structures can be finally employed. By application of different values of σ for the Hessian matrix-based filter we enhance vessels of different sizes, as depicted on Figures 3.16–3.19. Using multi-scale approach, we can merge results of individual scales to a multi-scale image (Fig. 3.20a and Fig. 3.21aa).

In this way, the vessel presence and the its size can be fully automatically detected, requiring no user interaction. The vessel segments can be identified e.g. by thresholding of the filtered volume (similar to Sato [113]) or possibly by active contour approach (e.g. as in Krissian [115]). A simple example of region growing complemented with hysteresis thresholding for such purpose is on Fig. 3.26.

As in these images also other interfering objects might be enhanced, we proposed to enhance the classification of the objects also with the orientation information (Fig. 3.22–Fig. 3.25). In these images, the color-coding defines orientation of the structure in space. It is evident that vessels are—nearly exclusively—vertically oriented structures (appearing as 'blue' in the the images).

In this manner, the vessels can be identified on a simple knowledge-based classification, e.g. as described in Tab. 3.2. For object identification, e.g. region growing with feature value thresholding can be used (Fig. 3.26).

(a)   (b)
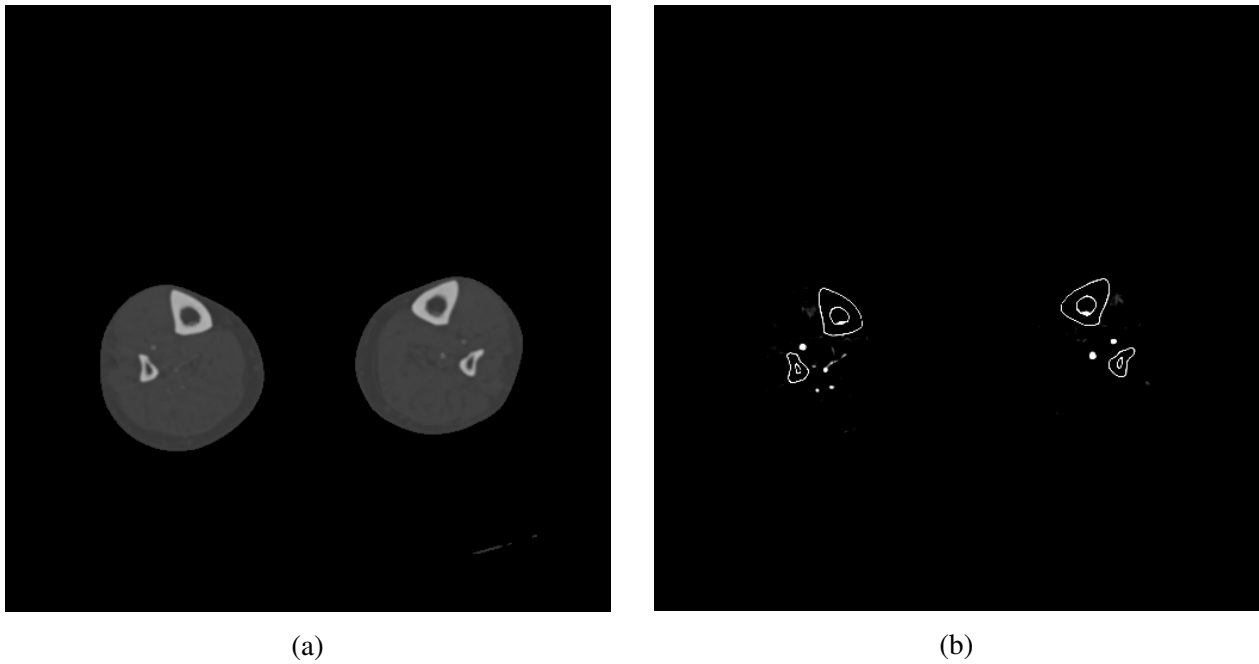
Figure 3.15: *Mapping of tissue-densities to vessel probability. (a) Original slice from a pCTA dataset; (b) Slice with vessel densities enhanced by remapping.*

Vessel Object	Features
Aorta	Cylindrical object with diameter e.g. $\approx$8–11 (largest object), vertically oriented, located centrally in the top of the dataset
Femoral Segments	Cylindrical objects with diameter e.g. $\approx$3–8, vertically oriented, located in the middle of the dataset
Tibial Segments	Cylindrical object with diameter e.g. $\approx$1–3, mostly vertically oriented, located in the lower third of the dataset

Table 3.2: *Example of knowledge-based classification of structures in pCTA dataset after Hessian matrix-based enhancement of cylindrical structures.*

3.6.2 Conclusion

In the previous text we showed a fully automatic method aimed at detection of vessels in pCTA dataset. The results demonstrate a promising way towards automatic extraction of vessel tree, e.g. by fitting a hierarchical vessel tree template, where knowledge about the objects (or their features) must be first extracted. The proposed method derives the approximate radii and orientations, together with a probability to be a cylindric structure in a given point of the dataset. Additionally, information about the object size and location can be derived, by employing e.g. region growing and thresholding.

We also identified the actual limitations of this algorithm:

- The most important are the memory requirements, representing minimally 1,2 GB of memory for processing of a full-sized dataset ($512\times512\times1200$), since for Hessian matrix-based filtering and the subsequent eigenvalue decomposition the data need to be computed in (at least) 32-bit floating-point precision. To overcome this limitation, specific research is currently performed in our group aimed at streamed implementation of the Gaussian kernel-based filtering with smaller memory requirements.
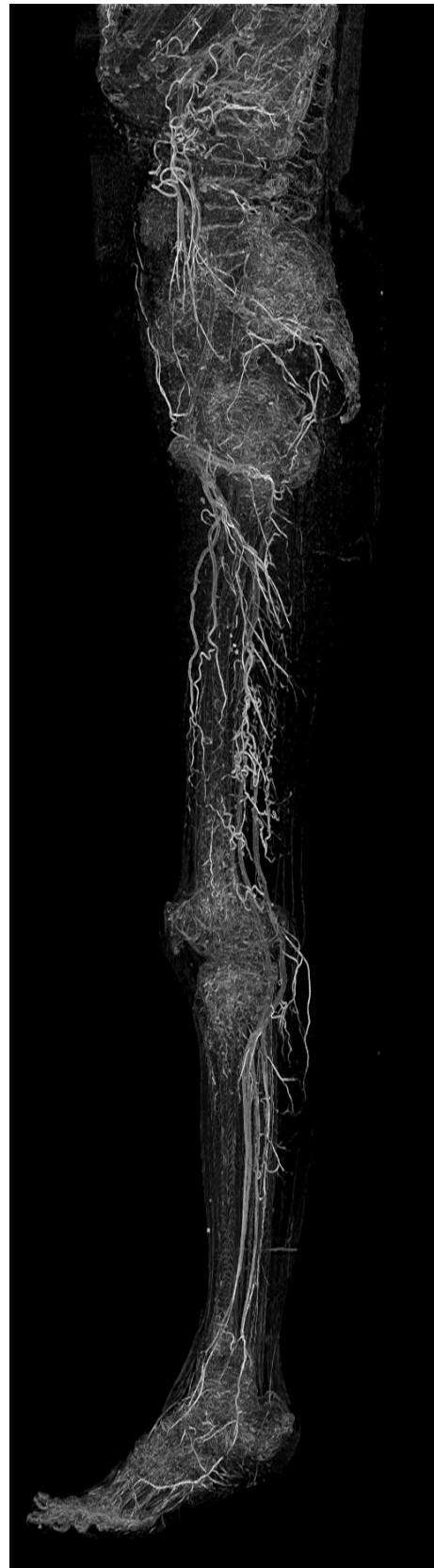
(a)   (b)

Figure 3.16: *Hessian matrix-based enhancement with $\sigma = 1.0$; mostly collateral vessels are enhanced. (a) frontal and (b) lateral MIP of the processed volume.*

(a) (b)

Figure 3.17: *Hessian matrix-based enhancementwith σ = 3.0— distal (tibial) segments of the vessel tree are mostly enhanced. (a) frontal and (b) lateral MIP of the processed volume.*

(a)   (b)

Figure 3.18: *Hessian matrix-based enhancement with* $\sigma = 6.0$*; medium-sized vessels (femoral and femoro-popliteal segments) are enhanced. (a) frontal and (b) lateral MIP of the processed volume.*

<div align="center">(a)   (b)</div>

Figure 3.19: *Hessian matrix-based enhancement with $\sigma = 8.0$; mostly the largest structures (e.g. aorta) are enhanced. (a) frontal and (b) lateral MIP of the processed volume.*

(a)   (b)

Figure 3.20:   *Comparison of Hessian matrix-based enhancement of vessels to a MIP with manually out-segmented bones. (a) MIP of multi-scale response of Hessian filtering, merged maxima from Fig. 3.16–Fig. 3.19), (b) MIP of original density volume. (Frontal views).*

<div align="center">(a)   (b)</div>

Figure 3.21:   *Comparison of Hessian matrix-based enhancement of vessels to a MIP with manually out-segmented bones. (a) MIP of multi-scale response of Hessian filtering, merged maxima from Fig. 3.16–Fig. 3.19), (b) MIP of original density volume. (Lateral views).*

(a)   (b)
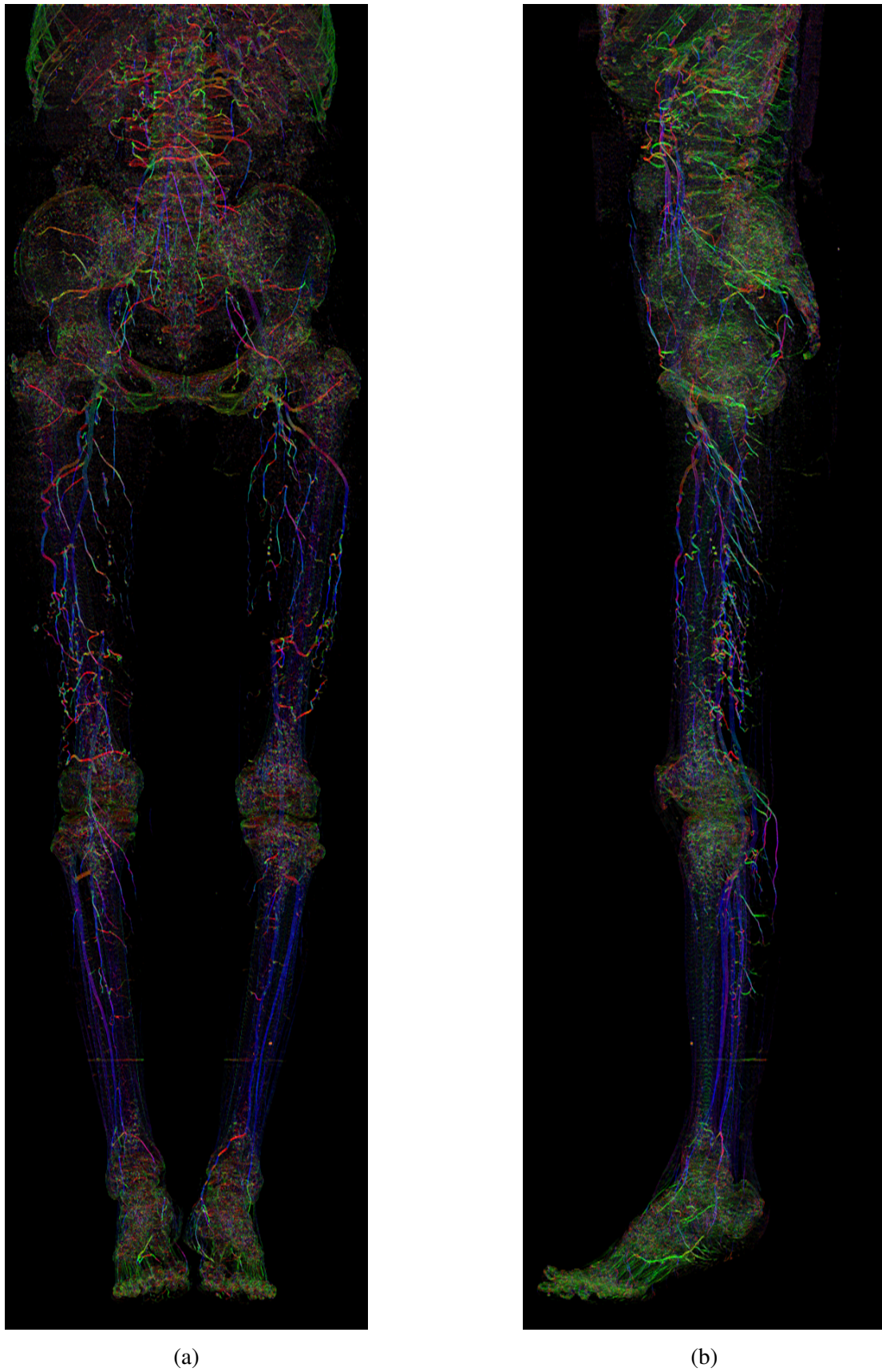
Figure 3.22:   *Hessian matrix-based enhancement of vessels with visualization of orientation. Red component conveys horizontal left-right direction, green component horizontal front-back direction and blue component vertical direction. Result for filter σ = 1.0. (a) frontal and (b) lateral MIP of the filtered volume.*

(a)   (b)
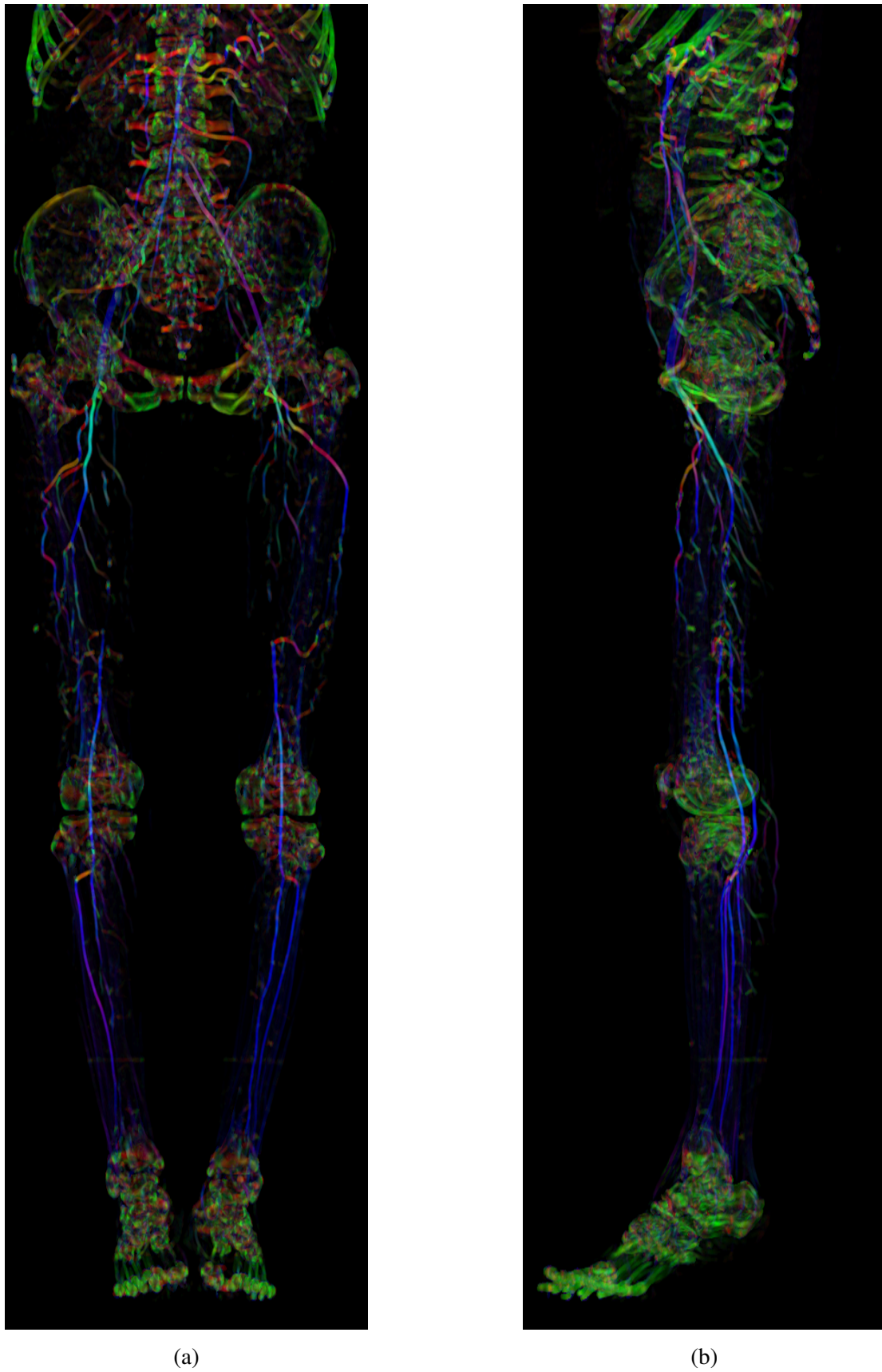
Figure 3.23:   *Hessian matrix-based enhancement of vessels with visualization of orientation. Red component conveys horizontal left-right direction, green component horizontal front-back direction and blue component vertical direction. Result for filter $\sigma = 3.0$. (a) frontal and (b) lateral MIP of the filtered volume.*

(a)   (b)
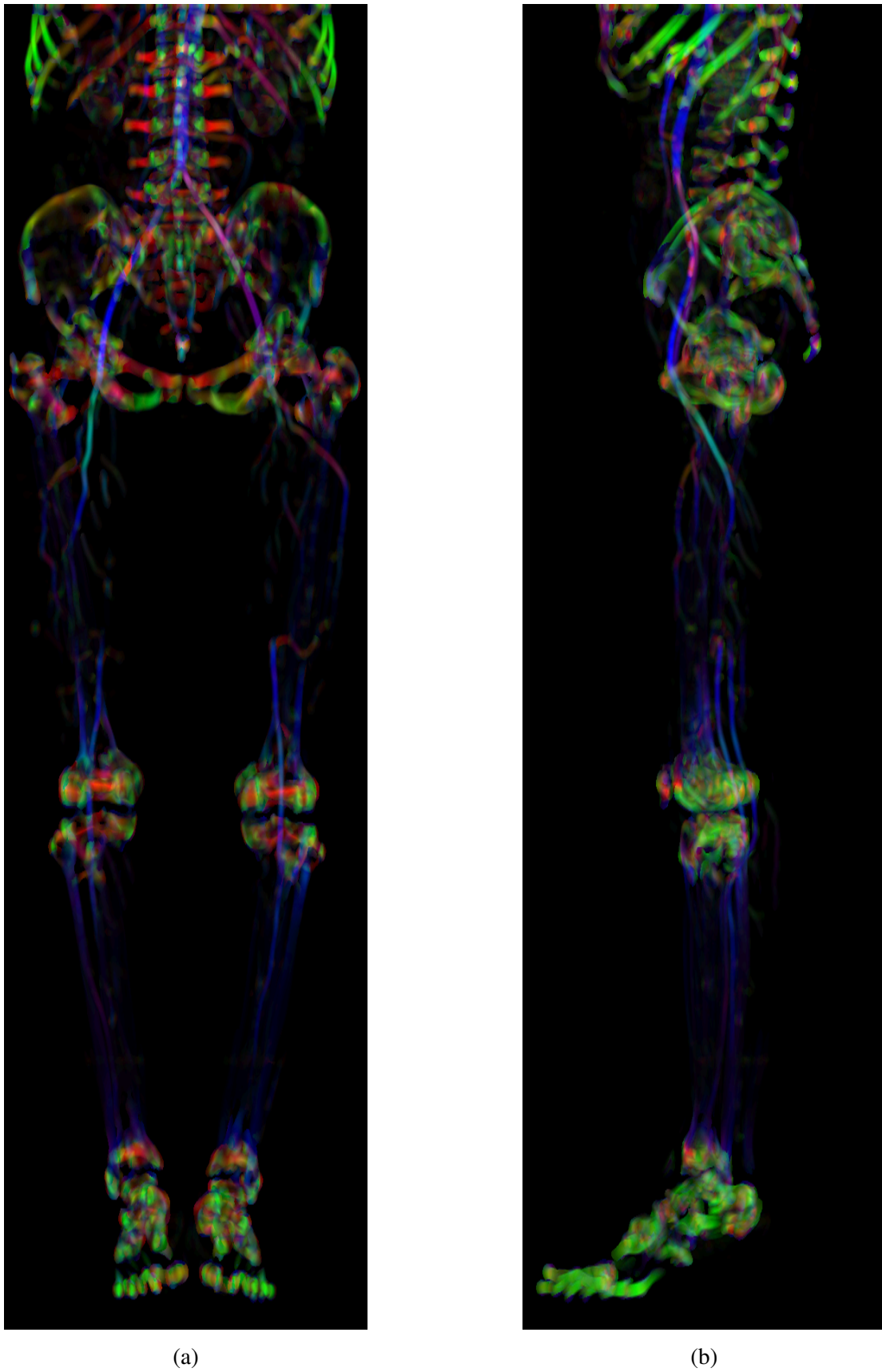
Figure 3.24:   *Hessian matrix-based enhancement of vessels with visualization of orientation. Red component conveys horizontal left-right direction, green component horizontal front-back direction and blue component vertical direction. Result for filter $\sigma = 6.0$. (a) frontal and (b) lateral MIP of the filtered volume.*

(a)   (b)
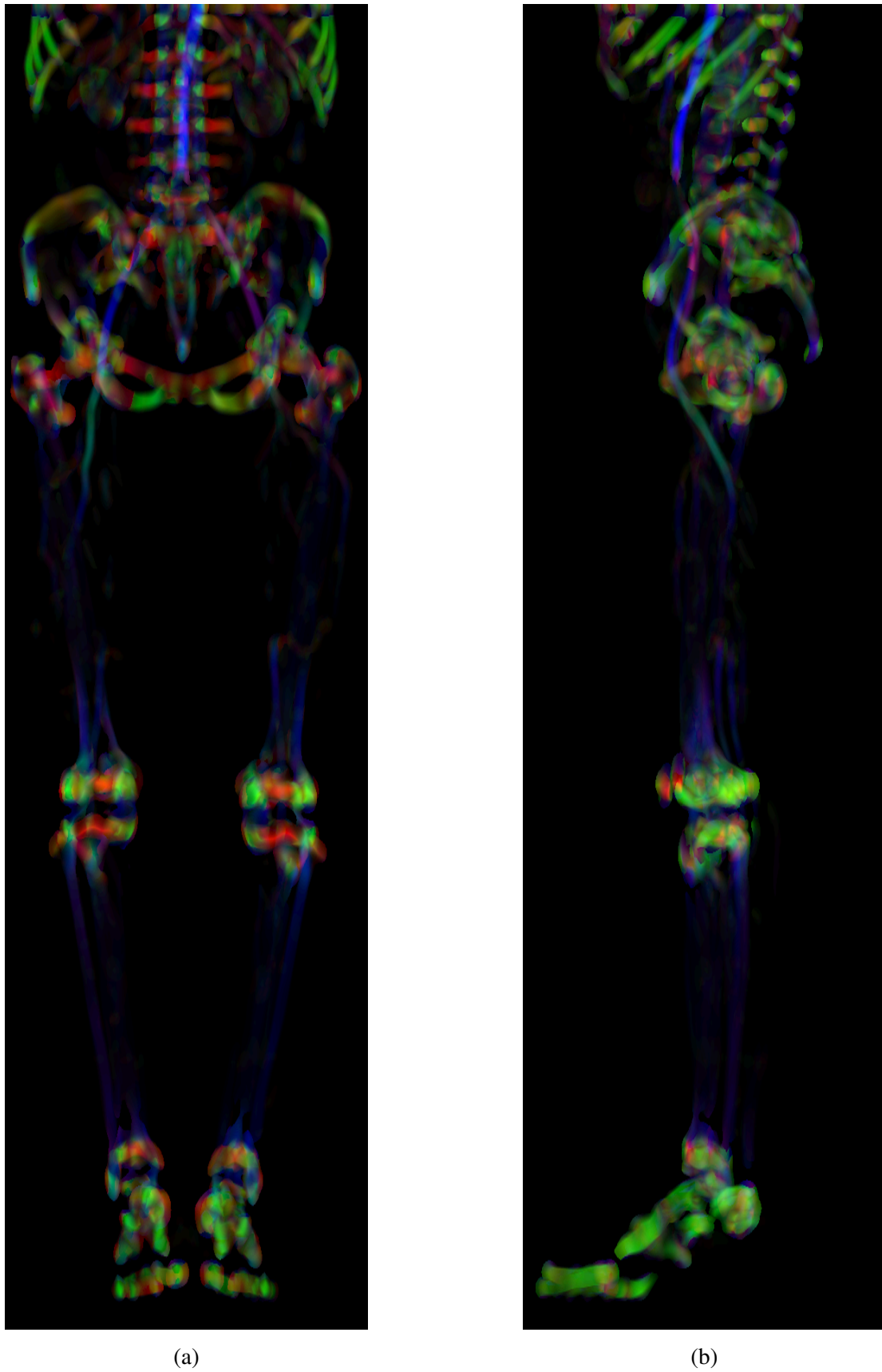
Figure 3.25:   *Hessian matrix-based enhancement of vessels with visualization of orientation. Red component conveys horizontal left-right direction, green component horizontal front-back direction and blue component vertical direction. Result for filter $\sigma = 8.0$. (a) frontal and (b) lateral MIP of the filtered volume.*

<center>(a)   (b)   (c)   (d)</center>
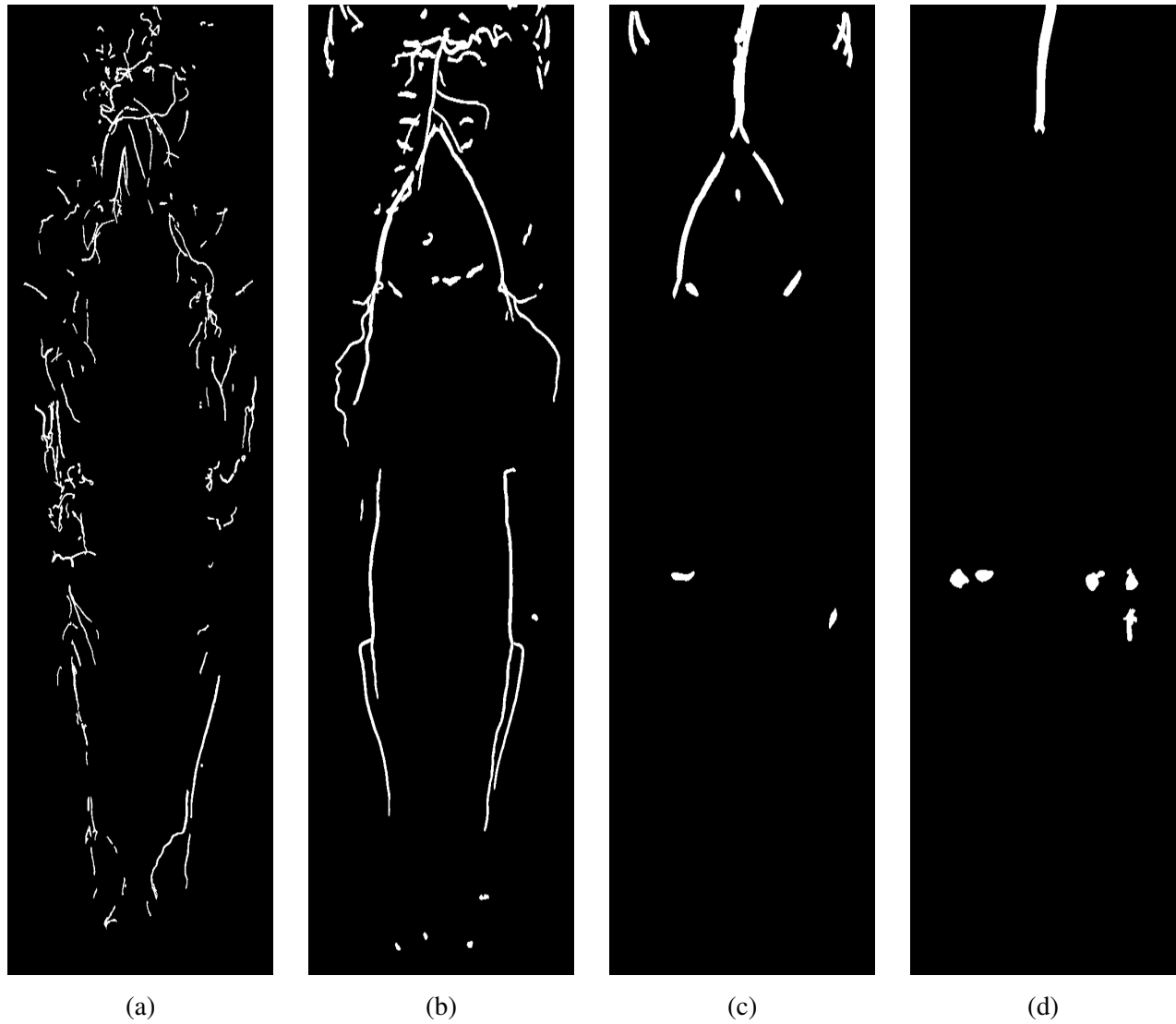
Figure 3.26:   *Identification of vessel structures in Hessian matrix-based enhancement, by means of hysteresis region growing, thresholding and small-objects rejection. Results for: (a) $\sigma = 1.0$, (b) $\sigma = 3.0$, (c) $\sigma = 6.0$ and (d) $\sigma = 8.0$. Compare with Fig. 3.16–Fig. 3.19. (MIPs of the mask volumes, resulting from region growing with hysteresis-thresholding, with $th_H = 0.3, th_L = 0.2$ and small-object rejection $th_{size} = 20$. Orientation properties were not considered in this case.)*

- Very important is also the computational complexity, mainly for kernels with higher σ. Simple implementation which uses only increasing filter sizes proved to be inapplicable in clinical practice as the filtering takes several hours for $\sigma > 5.0$. This heavy burden could be addressed in the future by building the scale-space by sub-sampling the datasets (as opposite to increasing of the filter sizes), by introduction of filter-code optimization (e.g. implementing the filters using dedicated signal-processing instructions of modern CPUs) or by application so-called recursive filters. These techniques could significantly reduce the computational requirements of the proposed vessel classification algorithm and thus bring it to further development.

- A weak point of the proposed algorithm is its dependency on the $D_{hardmin}$,D_{min},D_{max} and $D_{hardmax}$ remapping threshold values. If the dataset represent normal or slighly diseased anatomy, these values are
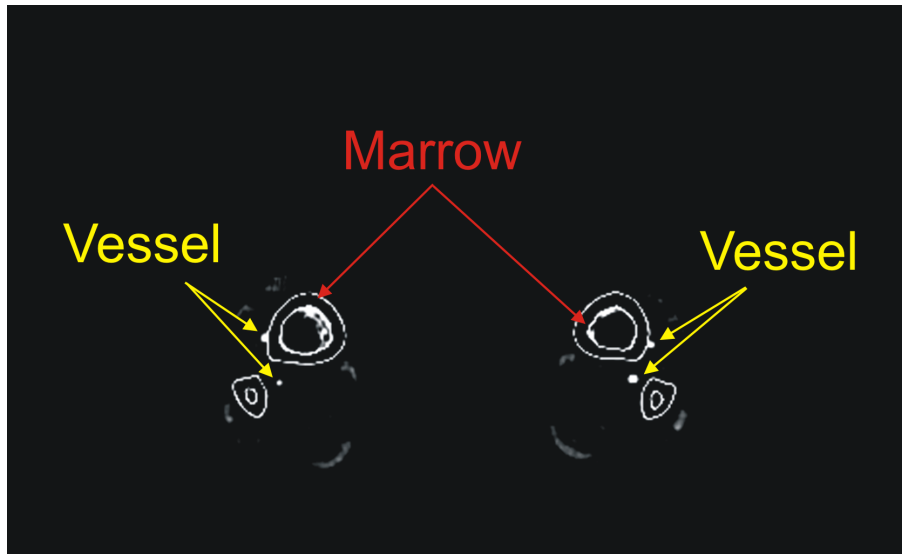
Figure 3.27: *A horizontal slice from vessel-density enhanced volume (by density remapping, see Eq. 3.17). In certain areas, not only the vessel but also the bone tissue, the bone marrow or PVE-affected areas are enhanced, interfering in Hessian matrix-based filtering, creating 'imaginary' objects.*

easy to derive, i.e. nearly constant for fixed scanning protocol. But, if the vasculature is severely affected, it is nearly impossible to set these thresholds globally so that the vessels form cylindrical shape in the remapped volume. It seems to be impossible to identify vessels of severely diseased patient based on their density and shape properties, as the tubularity criteria is no longer fulfilled. In such cases, manual interaction is a prerequisite.

- An inherent problem of the application of Hessian matrix-based filtering and the vessel-density remapping is the simultaneous enhancement of non-vessel structures, that prove density properties similar to vessels. The most pressing problem is the enhancement of the internal parts of long bones as tibia or fibula (see Fig. 3.27). There, parts of bone, bone marrow and PVE-affected areas become enhanced and due to the shape and size of these objects, these become amplified by the Hessian matrix-based filtering. In majority, this is caused by the PVE and generally is a sampling problem, influencing filtering results with small filter sizes.

3.7   Conclusion on Data Segmentation and Classification

In the previous sections, we gave an overview of methods that are aimed on segmentation and classification of pCTA datasets and suggested solutions to some of the presented problems, mainly by trying to introduce anatomic information to the segmentation step, either by application of an probabilistic atlas or by model-based object classification. According to the research and achieved results, we make certain conclusion:

To be able to label individual voxels correctly, *information whether the voxel belongs to a particular vessel is needed*. For this, the following criteria must be met: firstly, voxel density must be in a defined range of densities. If true, then secondly the presence of potential vessel in which the voxel shall lie must be evaluated.

To evaluate vessel object presence, rough estimation of vessel diameter must be presented first, as an input parameter of the algorithm. Then, objects of similar size will be detected. According to the features of the

detected object (orientation, location, size, shape) the presence of vessels can be determined and the question whether given voxel lies inside a vessel object can be answered. Such information is usually available for voxels lying close to vessel centerline and is less reliable for those lying close to the vessel border. Therefore, for precise segmentation, exact centerline and precise radius has to be identified, and the whole identified object will be finally labeled.

In the light of the above mentioned requirements, we dare to conclude that neither density or gradient information in individual voxels, nor density properties of regions with unknown shape exhibit sufficient features for vessel tissue classification. Thus, algorithms based on these assumptions cannot provide reliable segmentation in case of presented pCTA data.

The above described conclusions are valid for current pCTA datasets, but might become less relevant in future, mainly in the following cases:

- If second dataset with different density properties of the vessels can be acquired (e.g. a scan without a contrast agent injection), there will be much more information in a single location available for the classification purposes. In such bi-modal datasets, individual voxels could be identified solely on their 'dual' density properties. *(The first reason why this approach has not been implemented is the complexity of required non-rigid warping and registration. Simple subtraction without registration results in a difference image which is usually unusable due to patient movement. Registration, that includes non-rigid, free-form warping to compensate the shift of the corresponding tissues within the dataset is therefore needed. The computational complexity of such step is high, as the vector field describing the shift through the volume is difficult to derive and requires numerous optimization and warping steps. The registration must be also very precise, as even only a small misalignment would result in visible artifacts in the difference image. The second reason why this method has not been implemented is that the clinical experts do not prefer the double-scanning procedure, exposing the patient to doubled dose of X-rays radiation.)*

- With the advent of newly designed, dual-source CT scanners (scanners that have two sets of X-rays emitter units with detectors shifted by 90°) such segmentation approaches might became partially obsolete. As X-rays attenuation in the tissues does depend both on tissue type *and* type of X-rays radiation, by scanning the tissue with X-rays with different frequencies or measuring the attenuation spectra of a wideband X-rays emitter one can detect the tissue type. Individual units scan the body with different scanning protocols and therefore spectral properties corresponding to particular tissue types can be detected. Thus, using this spectral information the classification step will become very simple, as the iodinated contrast medium manifests properties different to calcium in bones. The patient body motion artifact shall be effectively suppressed by the simultaneous scanning.

Chapter 4

Modeling and Reconstruction

4.1 Introduction

For advanced vessel tree processing, assessment and visualization a precise geometric model of the vessel structures embodied in the pCTA data is needed. Under *modeling* we understand determination of parameters (e.g. geometric properties) and the structure of a vessel tree in the pCTA data. E.g., if we model the vessel tree as an oriented-graph model, where the vessel segments are represented by curved cylinders, then the parameters sought are the radius, orientation, centerline position and possibly also the density properties inside and outside of the reconstructed vessels, together with the topology of such graph. The number and complexity of the parameters depend on the selected model type, its structure and is mainly determined by the requirements of later processing, visualization or quantification steps.

The geometric information needed for applied visualization techniques described in Chapter 5 defines the minimum requirements on the model of the vessel tree. In our case, the most important is the vessel centerline identification (the axis of the curved tubular model), together with orientation and approximate radius information. The centerline is a prerequisite for the curved-planar reconstruction (CPR) images where the dataset is longitudinally resampled along these centerlines.

The modeling of vessel trees in pCTA data can be considered as hierarchical. On the top of the hierarchy (on the most abstract level), the topological structure of the vascular tree is modeled, e.g. as a set of segments and bifurcation points. On the middle level, the vessel segments are modeled as a sequence of short tubes approximating locally a curved cylinder. On the bottom level (on the most concrete level) the parameters of a cylindrical model correspond to local properties of the underlying data.

Generally speaking, the model building consists of three steps:

- **Definition of an area in which the vessel shall be detected and modeled.** In this step, areas where the vessel is present are defined. The purpose of this step is to derive initialization points for later estimation or fitting of a local vessel model. Such points can result from segmentation step, can be derived as an approximation of vessel path or defined manually by the operator. The goal is to limit the parameter search-space in the subsequent steps, to make them more reliable and faster. Here also approximate shape and orientation may be provided, either by explicit definition or as a result of processing (e.g. skeletonization, vessel-tracking, etc.),

- **Estimation of individual model parameters in particular location.** Taking the points from the afore-mentioned step, data properties in a neighbourhood are evaluated to estimate parameters of a local vessel

model. The model type is often pre-determined (e.g. a cylinder); parameters of such model are derived. This can be done either by iterative fitting of a template, followed by optimization of the parameters, or within a single computation. And

- **Building of a vessel tree topology and hierarchy.** In this step, the estimated local models are organized into a higher-level structure (e.g. points into segments, segments into tree etc.), which finally builds the whole vascular tree.

The sequence of the modeling steps is not always necessarily as presented; the order of operations may vary. E.g. the vessel tree reconstruction can be done first by estimation of local properties of the vessel segments and then by organization of these local models in a hierarchy. Alternatively, the hierarchy can be defined as first (e.g. given by known anatomic properties) and then the hierarchy and the local models of which it consists can be fitted to the actual data by means of automatic or semi-automatic techniques.

In the modeling, aspects of segmentation arise. For reconstruction, ideally a precise volumetric representation of vascular tree could be presented. In such case the surface, centerlines, etc. could be easily reconstructed. Unfortunately, this is not the case of pCTA data. Due to imperfections of segmentation and classification algorithms and pathologies presented in the data it is impossible to achieve precise segmentation. Therefore, modeling and reconstruction in pCTA data shall not address only particular geometric modeling, but should also tackle the imprecise identification of tissues. The main errors in tissue classification arise from problematic differentiation between soft tissue and non-calcified plaque/thrombus in the vessels, between vessel and trabecular bone and between calcification and cortical bone. The problem of imprecise segmentation can be partially addressed in the modeling by introduction of a fixed shape for particular local model or by smoothing and averaging of parameters of such local models, but in this way only small imperfections of the segmentation can be addressed. To achieve the best possible modeling and reconstruction, a precise segmentation a pre-requisite, what is a motivation for algorithms described in Chapter 3.

4.2   Related Work

Vessel reconstruction from volume datasets are a topic significantly addressed in the literature, both for 2D and 3D modalities, as the geometric model is very useful later in stages of visualization and quantification. There are several works that extensively review the vessel modeling and reconstructions issues, as e.g. Kirbas and Quek [62] or Bühler *et al.* [122]. Therefore, we give only a short overview of the existing techniques, which can be divided in three elementary groups:

- **Methods for diameter and center-line estimation.** Methods that generate feature images yielding high responses in the center of the vessels are used here, followed by a search process aimed on grouping of these features into connected structures. Multiple approaches exist: *skeletonization of binary segmented datasets*, by e.g. means of distance field (Selle *et al.* [123], Bitter and Kaufman [124]). These methods usually require additional pruning and grafting of the resulting binary segmentation to obtain vessel axis. To overcome this problem, e.g. a gradient vector field flux was suggested in Bouix *et al.* [125]. *Height-ridge traversal* (Frangi *et al.* [80], Furst *et al.* [126], Furst and Pizer [127], Aylward and Bullitt [128], Lindeberg [119], Sorantin [129], Passat [130] and others) can be alternatively used for the centerline extraction. These ridges can be either density ridges from the original dataset (typical for smaller vessels where borders are less dense due to PVE) or can be a result of cylindrical structures enhancement by appropriate filtering techniques(as described in Section 3.6), studied e.g. by Krissian *et al.* [115]. In these

methods, the centerline can be directly the path along the height-ridge, or the centerline is determined as a skeleton of the structures in the input data which are previously binary segmented (e.g. by thresholding) or a model can be fitted to the height-ridge data and modified until optimum is reached (Fridman *et al.* [131]. The height-ridges or the skeletonization points can be also interpreted as 'optimal points' for the vessel center and a centerline of a vessel as a curved line connecting these optima. Therefore, vessel centerline identification can be implemented also as an optimal path search (so called *vessel-tracking*), either as an iterative process (Flasque [132]) or as the Dijkstra's least costly path algorithm (Kanitsar *et al.* [15]). Such approach is very similar to challenges addressed in works dedicated to virtual endoscopy, i.e. finding an optimal path for viewing the examined anatomic structures (e.g. Deschamps and Cohen [133]). Both problems are similar, trying to find centerlines for cylindrical or tubular objects. Having a centerline, the diameter is usually determined by fitting and optimization of a local model or by optimization of some likelihood measure (Wink *et al.* [134]), trying to estimate local parameters of the object (orientation, size). Within our research, we also experimented in this field, by trying to fit a cylindrical model to a vessel in local neighbourhood (La Cruz *et al.* [135]),

- **Methods for Vessel Surface Reconstruction.** Within these often deformable models (e.g. level sets Lorigo *et al.* [79], active contours Lorenz *et al.* [116] and Yan and Kassim [136], deformable organisms McInerney *et al.* [32], B-Splines and NURBS Volkau *et al.* [137]) are used. In these approaches borders of vessels are determined (based on the high gradient-magnitude features) and the surface of the vascularity is derived and modeled. In majority of the mentioned approaches the hierarchical structure of such derived model is not considered, as the surface description does not provide such information. Such information can be derived later by binary segmentation and introducing skeletonization approaches mentioned earlier, and

- **Methods for estimation of vessel tree topology, hierarchy and spatial arrangement.** The vessel tree topology, hierarchy and its spatial arrangement is important for further evaluation and processing of the whole vascularity, therefore its reconstruction and modeling is an important step. Agam *et al.* [138] reconstructed the thoracic vessel system by application of cylindric filters and fuzzy shape representation, to improve detection of nodules in lungs. Selle *et al.* [123] applied graph-analysis approach to recover the hierarchy of vessels detected by skeletonization. Zana and Klein [139] used Hessian and Laplacian filters to detect bifurcations in eye fundus, where a simple tree model was created and most similar model of the vascularity was fitted. In Bullitt *et al.* [140] analysis of pre-segmented vessel segments was implemented and vessel tree was built on similarity, parent-child relationship and modified minimum spanning tree algorithm (Bullitt *et al.* [141]) basis. In work of Chalopin *et al.* [142], skeletonization and graph-structure recognition, based on previous anatomic information was used. In the presented works, either analysis of the derived structures was executed and morphological and hierarchical restrictions were set (e.g. cycles were not allowed) or a predefined template was fitted to the underlying data.

A sore point of the vessel modeling are the bifurcations. Modeling of these is often omitted; only few works addressed this problem, e.g. in the extraction of branching tubular structures by cores in volume datasets by Fridman *et al.* [131]. In their work, vessels in MR were considered, where continuation of the vessel course and spatial properties of the bifurcations were considered, mainly relying on the distinguishable density properties of the vessels. Antiga and Steinman [143] proposed a solution of bifurcation modeling by decomposition of the identified vessel segments to a set of best-fitting spheres; but their approach was applied to already preprocessed triangular surface mesh and not to volume data.

4.3   Problems of Vessel Model Reconstruction in pCTA Data

A very promising visualization technique for PAOD assessment, which proved clinical relevance is the curved-planar reformation (CPR) (see Section 5.2). To generate CPR images, centerline of a vessel course is needed. A centerline must be created for the whole vessel path, originating in aorta and leading down to pedal arteries, to allow global assessment of the disease. Such vessel path is created as a combination of multiple segments from the model. To provide such paths from a vessel tree model, three challenges must be addressed in the reconstruction:

- **Estimation of the centerline and the radius of the cylindrical segments.** This is a complex task due to pathologies present in pCTA data (see later in the text),

- **Building of the vessel tree hierarchy.** Building the vessel tree hierarchy is important mainly for CPR image generation, but also for later vessel tree quantification. For pCTA data, it is often done semi-automatically; fully automated approaches depend on the availability of precise identification of vessel segments,

- **Precise modeling of the bifurcations.** Bifurcation are often locations where lesions start to develop; their precise visualization help in detailed diagnostics and treatment planning. Geometric modeling is complicated, as the shape of bifurcations vary significantly. If a precise volumetric model of the bifurcation would be available, then e.g. surface modeling or extraction by cores ([131]) or skeletonization would be possible. Actually only approximate solutions are available; this topic needs to be addressed in future.

Centerlines and radii are currently the most important geometric properties of the vessel tree, as they are a prerequisite for used visualization techniques (Chapter 5). Manual specification of these parameters for the whole vessel tree is unfeasible; therefore in our research we have focused on design, improvement and evaluation of algorithms that estimate local properties of the vessel segments and constitute a curved-cylinder model.

Various methods presented above can be used to derive centerlines; in our research we utilized the so-called *vessel-tracking* algorithm (described in [15]), which proved good results even in presence of PAOD-induced pathologies. Vessel-tracking is implemented as a searching of optimal path in evaluated graph, where vertices of the graph are positions of the individual data voxels and values of the edges are given by density and gradient properties therein. To ensure acceptable computation times, algorithmic optimizations for optimal-path search algorithm were introduced (Falcão and Udupa [144]). Start- and end-points for the path searching are defined manually (by the operator). Because in computation the vessel size is not explicitly considered, the path inside the vessel will be not necessarily centered, causing the *pseudo-stenosis* problems in the CPR images ([16]). To overcome this limitation so-called *vessel-path centering* must be employed, to ensure that the path used for CPR image generation is in the centre of the particular vessel. This process corresponds to fitting of a local model, during which a circular cross-section of the vessel is expected in a cross-section resampled perpendicularly to vessel axis.

In this setting, the local model estimation is reduced to estimation of parameters of a circle or an ellipse that models the vessel border in the perpendicular cross-section; for more stable estimation a straight cylinder with circular or elliptical cross-section can be fitted, averaging information from multiple slices. Then, the problem is the detection of border points. To the points a model is subsequently fitted and a best fit is evaluated. This might be tricky because the vessel wall is problematic to detect and model due to its complex shape resulting
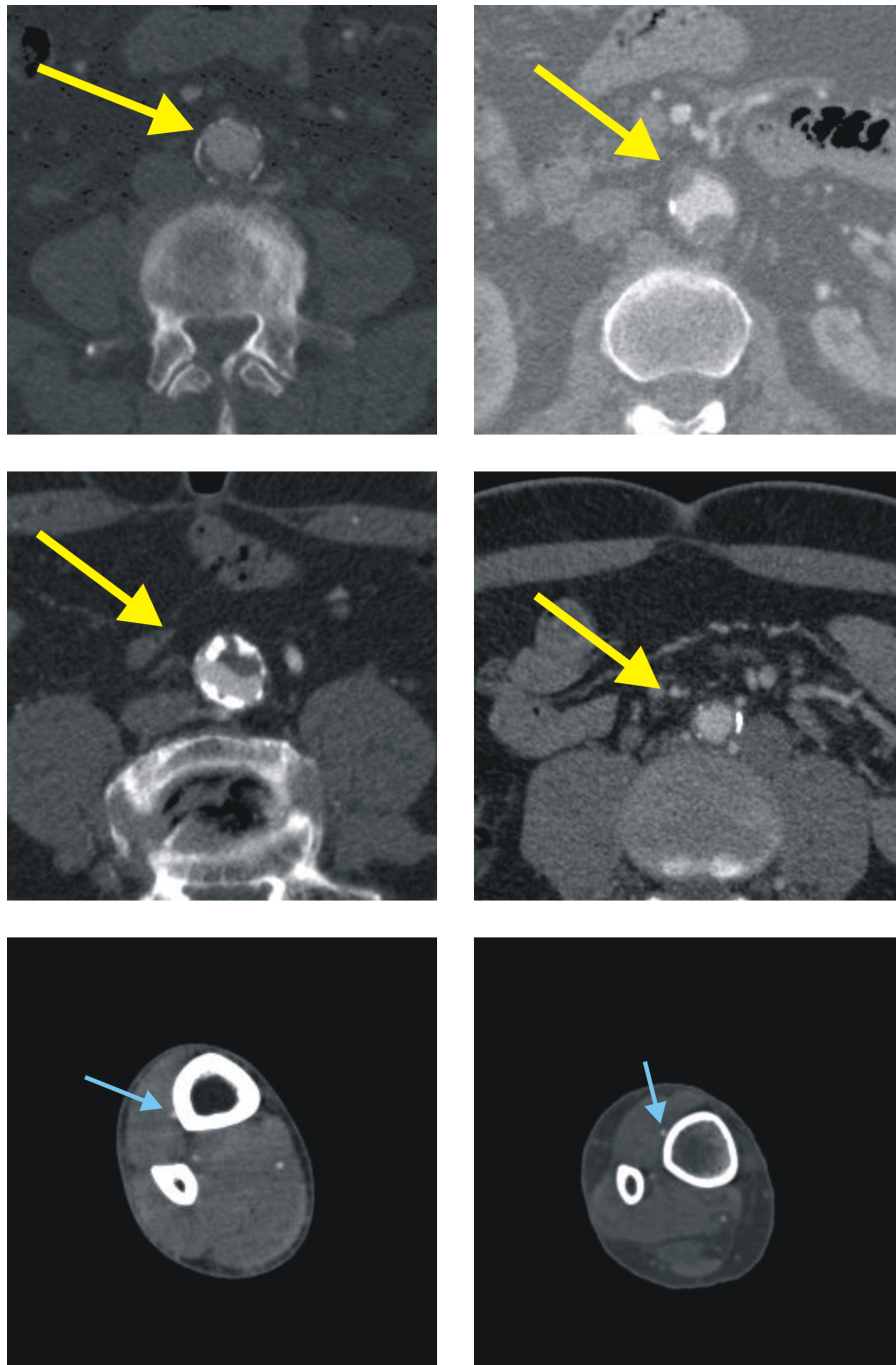
Figure 4.1: *Pathologic changes in the vessels hamper easy reconstruction of vessel segments. Top and middle row show cross-section of the aorta (yellow arrows) affected by PAOD (within the vessel, the dark areas are soft plaque and the bright are calcifications); the problem is to detect the correct diameter. The presence of bone objects (vertebra) which posses same density properties make a precise reconstruction even more difficult. The bottom row show cross-sections in area of tibia. The vessels are thin, blurred due to PVE, thus problematic to identify and reconstruct precisely.*

from PAOD pathologies (see Fig. 4.1).

Research presented in this thesis was neither specifically focused on vessel wall detection, nor on development and evaluation of vessel tree modeling techniques. For data processing, we introduced and modified the

already existing techniques ([15, 16]). Nevertheless, we consider modeling and reconstruction to be important part of pCTA processing pipeline; in case of interest we kindly recommend the reader to other works that address this issue, e.g. the PhD thesis of La Cruz [145]. The vessel border reconstruction for a vessel influenced by atherosclerotic diseases is an interesting problem, being addressed within the scientific community; the results are still questionable (e.g. [146]).

A specific problem in the pCTA data is the existence of occlusions, i.e. of vessels in which the blood flow is completely blocked. This happens either due to development of atherosclerotic lesions that fill the whole vessel lumen or due to blocking of the particular vessel due to thrombus. As a result, these vessels are not visible in the CTA images, because the contrast-medium did not flow in. Still, reconstruction of such occluded vessels might be of clinical interest, e.g. for treatment planing. To allow this, a knowledge-based interpolation was suggested in our environment (Rakshe *et al.* [148]) to bridge the missing segments. Nonetheless, automatic recognition of the whole vessel tree hierarchy remains still a challenge and various semi-automatic approaches are designed and tested.

Chapter 5

Visualization

5.1 Introduction

The visualization is the last step of the pCTA data processing, but is the most important one. Actually the results of this step are that 'what matters' in medicine. The ability to create high-quality and intuitive images that depict particular pathologies influences the overall applicability of the pCTA data-processing pipeline in the clinical environment. The objective of visualizing the peripheral arterial tree in patients with PAOD is to detect, localize, and gauge the degree and length of vascular changes which cause diminished blood flow to the legs in order to initiate the appropriate therapeutic measures. Visualization of these properties from the datasets is not trivial and straightforward and in this chapter we discuss the bottlenecks and potential solutions.

Visualization of data is a very important subject overall in the science, as it enables intuitive and simple condensation of complex information. It is well known that a good image is worth of thousand words. In an image, mutual relationships of various features can be shown, leading to intuitive understanding of the situation, which would otehwise be complicated to achieve by verbal explanation. A typical example of image-based visualization that unveiled important relationships was the visualization of cholera patients by Dr. Snow (London, 1854), where the source of cholera—a pump with infected water— was identified and by banning its usage the cholera epidemic was successfully ended.

The term *visualization* covers a wide range of approaches. On one side, it relates to displaying of objects in photo-realistic quality. A whole field of computer graphics, named *rendering* is dealing with such visualization. On the other side, visualization relates to displaying of measured signals or derived information in 'an artificial way', where the interpretation of a resulting 'image' is not straightforward and has to be 'learnt'. An example of the latter are e.g. function charts, histograms, scatter plots, etc. But such visualizations can—if done properly—intuitively depict certain features of the data and show important properties. Challenges of this type are investigated in the field of *information visualization*.

Visualization of medical data is somewhere between these two extremes, depending on the modality. It typically incorporates some features of both mentioned approaches. Natural photo-realistic visualization is preferred for its intuitivness, but only simple information (location, presence, density) can be presented in this way. On the other hand, visualization of signals that have no spatial relationships (e.g. electrocardiogram signals) is often needed and therefore information visualization approaches must be employed. In visualization of medical data the challenge is to find a way how to depict the information hidden in the dataset, so the images allow: i) intuitive and ii) reliable diagnostics of the clinical problem in question.

5.2   Visualization of Volume Datasets and Related Work

pCTA datasets are volumetric (3D) datasets, as explained in Chapter 2. They consist of several hundreds of 2D axial slices (Fig. 1.8), constituting a 3D volume. In early stages of CT technology the individual 2D slices were examined for diagnostic purposes. The clinical experts evaluated the axial images and traced down the pathological changes in the tissues. This has been possible only when only just few slices were created, in the period of single-slice CT scanners. But such approach is becoming less and less feasible with the advent of modern multi-slice CT devices, which generate more than 1000 transverse images at once. Inspecting such a vast amount of pictures is very tedious and prone to examination errors. Hence, methods for visualization of the whole 3D volume in a smaller set of views are required. Thus, methods that map or project 3D volume to 2D views must be employed.

The simplest methods for volume visualization come from the idea of modeling the traditional X-rays examination. By 'casting rays' parallel to a viewing direction through the dataset it is possible to simulate measurement of 'energy attenuation' along the rays, if the voxels in the dataset are assigned 'attenuations' according their densities. The summed attenuations are then projected on the viewing plane, resulting in final dataset re-projection. More often, a similar technique called *maximum-intensity projection* (MIP, Rossnick [149]) is applied, projecting only the maximum density value along the ray to the viewing-plane (Fig. 5.1a, Fig. 5.1b). MIP, despite it simplicity proved its significant usefulness in vessel visualization both for CT and MR modalities (Napel *et al.* [150]).

Extending the concept of attenuations and ray-casting further, *a direct volume rendering* (DVR, Levoy [151], Drebin *et al.* [152]) can be introduced. By assigning color and transparency values to the voxels according their densities, objects in the dataset can be visualized (Fig. 5.1c). Surface shading can be introduced by taking the surface normal and viewing direction into account. DVR has gained high importance in radiology within recent years (Fleischmann *et al.* [153]), as it is quite a simple method and is capable to generate very intuitive images, especially for CT data.

Taking parameter setting of the DVR to an extreme, one can assign complete transparency to certain density ranges and complete opaqueness to others. Thus, through a visualization method called *iso-surface rendering* only surfaces of the objects are visualized (Fig. 5.1d). Because of resulting images not capable portraying important pathologic changes (which are volumetric, not surface phenomena), iso-surfacing is rarely used for vessel diagnostics.

5.3   Vessel Visualization in pCTA Datasets

The culprit lesion in atherosclerosis is the plaque, causing luminal narrowing (stenosis) or completely filling and occluding the vessel lumen. Initially, atherosclerotic plaque is of soft-tissue density (i.e., X-rays attenuation similar to muscles), and thus hypodense to the contrast-medium opacified intravascular blood stream. Over time, however, atherosclerotic plaque calcifies and its CT density is then greater than the of contrast-medium opacified blood. This poses a significant problem for imaging diseased arteries with CT, because the hyperdense, calcified plaque obscures the vessel lumen when MIP or DVR is used (Fig. 5.2). Because of the different therapeutic consequences it is clinically important to distinguish between calcified plaque, significant narrowings, and complete occlusions. Another problem of the MIP and DVR techniques in vessel visualization is that vessels are frequently obscured by bones, unless the bones are segmented out in a separate procedure

| (a) | (b) | (c) | (d) | (e) |
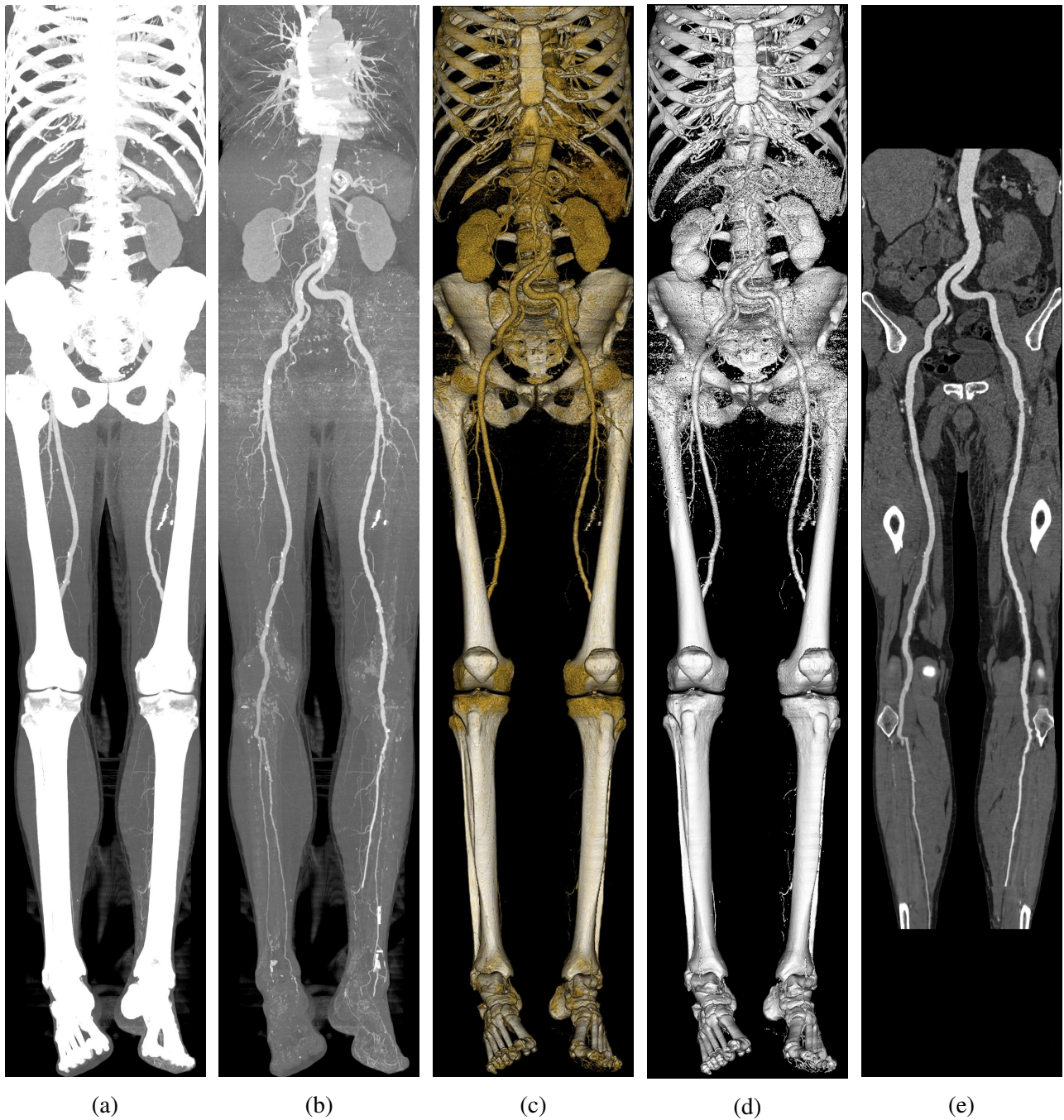
Figure 5.1: *Visualization of a pCTA dataset. (a) maximum-intensity projection (MIP), (b) MIP with manually outsegmented bones, (c) direct volume rendering (DVR), (d) iso-surface visualization (th = 200 HU) and (e) multi-path curved-planar reformation (mpCPR)*

(compare in Fig. 5.1). Both MIP and DVR, however, provide excellent spatial perception for the observer and provide bony landmarks for vessel segment identification. They also nicely display collateral vessels. This is important, because a significant flow obstruction in the main conducting arteries is often accompanied by the development of a network of collateral vessels, which maintain a basic blood supply to the tissue distal to the lesion. Therefore, the presence of collateral vessels is an indirect sign of a presence of hemodynamically significant reduction of blood flow.
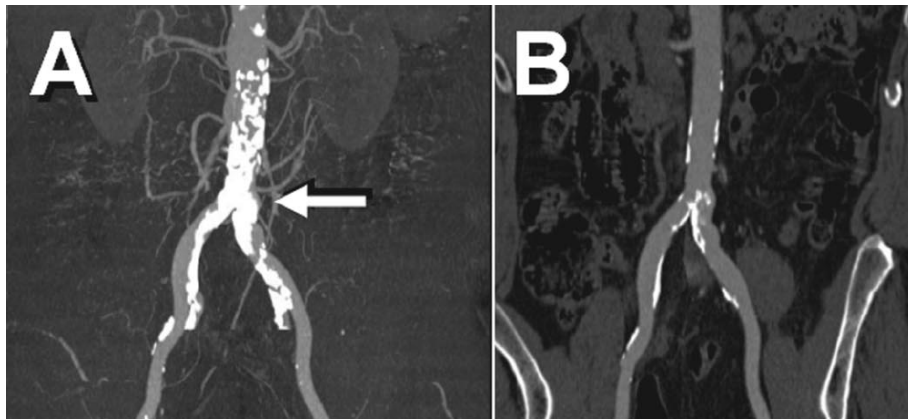
Figure 5.2: *Vessel lumen is obscured in MIP images (A), but visible in CPR (B). (Image reprinted from [153].)*

A reliable and automatic segmentation of diseased vessels in their entirety is still elusive, despite of achievements described in Chapter 3 and 4. There are, however, robust algorithms that can approximately calculate the center paths of the major conducting arteries [15, 154, 133, 155]. The peripheral arteries of the lower limbs constitute a tree-like structure and their centerlines represent a three-dimensional tree of paths (Chapter 4). The vessel tree can be used as an input function for the creation of curved planar reformations (CPR, Kanitsar *et al.* [16]). These longitudinal cross-sections through the arteries provide an excellent view on the vessel lumen (Fig. 5.1e), unobstructed by calcified plaque or overlying bony structures. A CPR is generated by resampling the 3D data set along a free-form cut surface as determined by the vessel centerline of the artery of interest. All other objects of the dataset (which may provide clinically useful information such as anatomic context, bony landmarks, or collateral vessels) are either distorted or not visualized at all (Fig. 5.1e). This limits the spatial perception of CPR images and thus their ability to communicate the findings to the treating physician.

A CPR allows an unobscured investigation of the vessel lumen by creating a longitudinal section through an approximate vessel centerline. Eccentric plaques and calcifications are investigated by rotating the CPR around the central axis of the vessel. The limitation of CPR is that it is sensitive to an incorrect vessel-centerline position, which may lead to so-called *'pseudo-stenosis'* (Kanitsar *et al.* [16]). It may also fail to visualize very thin vessels due to the same problem. Another inherent disadvantage of CPR, however, is its ambiguous display of the anatomic context. The viewer cannot reliably identify the anatomic segment that is displayed in the CPR image, which is essential for clinical decision-making. Kanitsar *et al.* [16] also developed extensions of the basic CPR concept, called thick-CPR and multi-path CPR (mpCPR). Thick-CPR performs MIP rendering in a close vicinity of the curved plane through the vessel centerline. Multi-path CPR incorporates CPR renderings of an entire vessel tree within one image, which improves spatial perception.

To allow intuitive and representative visualization of curvilinear and cylindric structures in an unobscured and proper manner, extensive research has been done. Much work has been published related to the clinical visualization of cylindrical structures, mostly referred to as virtual endoscopy (VE, Hong *et al.* [156], Wan *et al.* [157]). Here the researchers also tried to solve the problem of visualization along an identified centerline. With VE the interior of a cylindrical structure is visualized. As opposed to vessel visualization it shows the outside of cylindrical structures and the anatomical context. Hauser *et al.* [158] developed two-level rendering of medical images. In their work, they fused DVR and MIP techniques in one image. A density-based pre-classification step determines which technique to use for which object. DVR was used for bones and vessels and MIP was used for skin and soft tissue. Zhou *et al.* [159] extended this approach and developed a system where a region

in focus is defined through a 'magnifying glass'. Within the magnifying glass, the data is rendered photo-realistically, e.g., using DVR. Outside this region, data is rendered using non-photo-realistic styles, e.g. using contours only. Viola *et al.* [160] employed focus & context visualization for biology datasets, where the objects in focus were pre-labeled and the visualization properties (e.g. transparency) were governed by the information which objects are in focus in respect to their mutual spatial organization.

5.4 Focus & Context Visualization of Vessels

From the previous considerations it follows that the vessels as focus objects should be treated differently than the surrounding context data. The focus & context approach has been already widely used in information visualization (Card *et al.* [161]). An extensive work in the area of focus and context visualization was done by Viola [162], exploiting these approaches also for biomedical datasets. Visualization of vessels is a good example where this concept can be applied to the advantage of medical imaging. In this setting, the available information from the pre-segmented vessel tree can be used by our algorithms for defining the focus area in the dataset, which is treated differently from the rest of the data (context).

Here we introduce the *VesselGlyph* (VG) for focus & context rendering of blood vessels. The VesselGlyph is an abstract representation aimed at incorporating different rendering styles for the creation of an image. An example would be a CPR rendering of a vessel and its immediate neighborhood, combined with a DVR rendering of the surrounding data. The VesselGlyph serves several purposes. On the one hand it gives an abstract notation on which rendering styles are combined and shows how the transitions between the styles are handled. The VesselGlyph also facilitates a systematic exploration of various combinations of rendering techniques which otherwise would have eluded the investigator. Furthermore, the VesselGlyph may serve as an interface element, which allows the user to change styles or parameters. Examples in this respect could be the type of CPR (CPR or thick-CPR), width of the transitional region between the focus and context areas and the context area rendering algorithms (DVR or MIP).

The VesselGlyph allows visualization and investigation of objects in areas where they would otherwise be obscured if volume visualization techniques alone would be used. A spatial configuration of the VesselGlyph that suppresses objects in front of the focus area may solve this problem. The advantage of the VesselGlyph is the possibility to depict the investigated structures in their correct anatomic context.

5.5 Concept of the VesselGlyph

The VesselGlyph is an abstract notation describing the combination of different rendering styles within one image. Let us consider a single axial slice of a CTA data set showing a round cross section of an artery oriented perpendicularly to the CT section. The focus area is close to this circular object. The context area is the area surrounding the vessel. The vessel path intersects the axial slice close to the center of the vessel. The VesselGlyph (Fig. 5.3a) describes the spatial arrangement of focus and context regions, where different techniques are used for rendering with a possible smooth transition between them. Sweeping the VesselGlyph along the curved vessel centerline would cover those regions of the data that constitute the focus and context subset in the original volume data. As an example, the VesselGlyph shown in Fig. 5.3a combines CPR rendering of the focus with a DVR rendering of the context, including a smooth transition between the two rendering styles. The CPR rendering is depicted as a horizontal line as CPR resamples the vessel along an infinitesimally
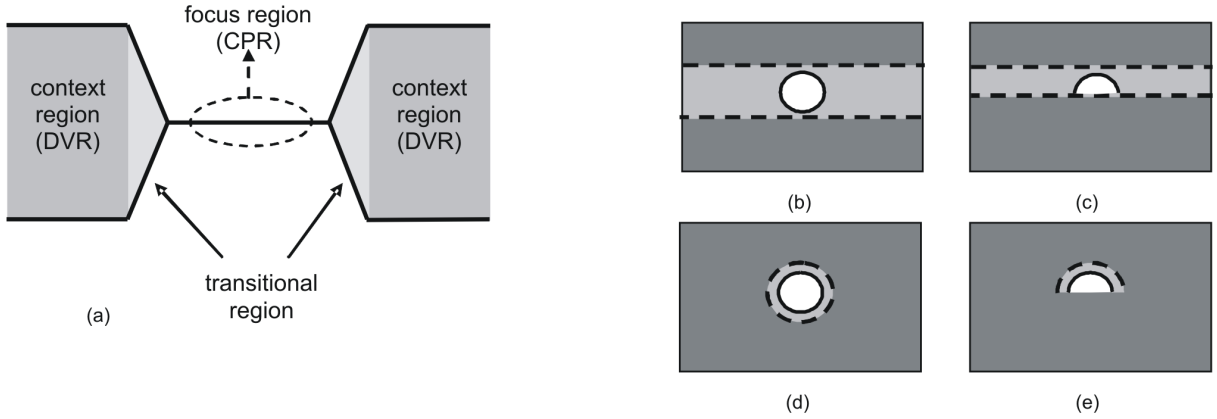
Figure 5.3: *(a) The VesselGlyph (VG) for vessel focus & context rendering. VesselGlyph configurations for: (b) full-vessel Thick Slab VG, (c) half-vessel Thick Slab VG, (d) full-vessel Tubular VG, (e) half-vessel Tubular VG.*
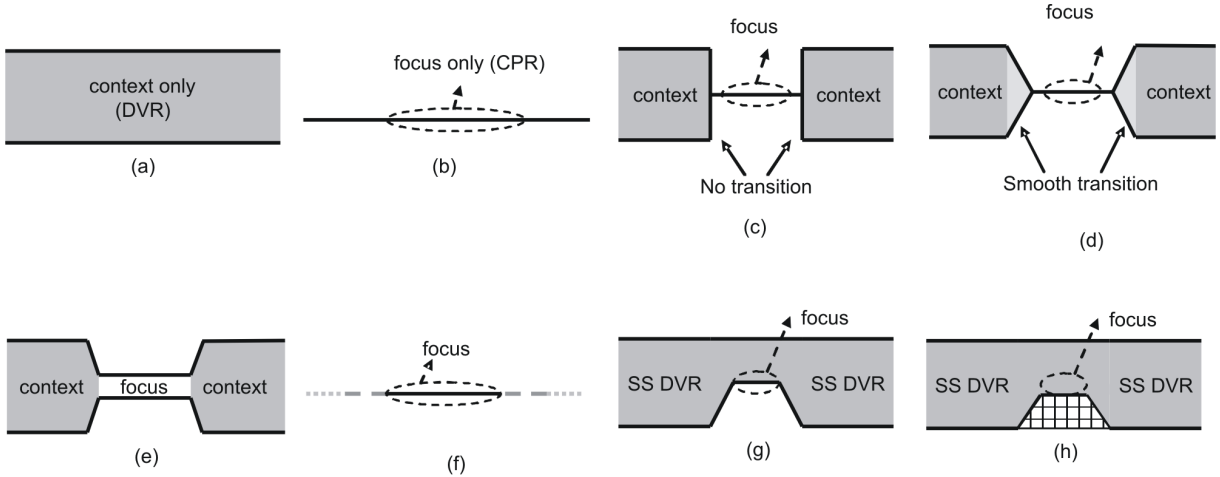
Figure 5.4: *VesselGlyph examples: (a) DVR of the entire dataset, (b) CPR through the vessel centerline, (c) combination of CPR and DVR without transition, (d) combination of CPR and DVR with transition region, (e) thick-slab, (f) CPR with fading in context area, (g) foreground-cleft with surface-shaded DVR (SS DVR), (h) foreground-cleft with occlusion lines.*

thin free-form surface. The DVR style of the context is depicted as two symmetric grayish areas. The larger extent of these areas reflects the fact that DVR takes samples from a larger region of the data set. If ray-casting is used for rendering then all samples along each ray are taken into account. The VesselGlyph further describes a smooth transition from CPR to DVR. Close to the focus region only a thin slab of data samples is considered in the rendering stage. Close to the context region more data samples along an individual ray are included. Fig. 5.4 gives examples of several possible configurations of the VesselGlyph. This figure also shows that previous vessel visualization techniques (DVR, CPR) can be considered as special cases of VesselGlyph.

The VesselGlyph can thus also be regarded as an extension or generalization of known approaches. Fig. 5.4a represents the VesselGlyph that describes standard DVR. It provides excellent context visualization, but as no focus region is defined, the vessels of interest may be obscured by overlying bony structures or vessel wall calcifications. Fig. 5.4b describes the CPR rendering, which provides a detailed view on the vessel and its

flow channel. Data far away from the vessel center are intersected by the thin curved surface, which does not provide a good context overview. Fig. 5.4c and Fig. 5.4d show combinations of CPR for the vessel and DVR for the context. The abrupt transition in Fig. 5.4c produces discontinuities in the resulting image, which makes it easy to distinguish between focus and context. In Fig. 5.4d there is a transitional region that ensures a smooth change from focus to context. In Fig. 5.4e a combination of a thick-CPR in the focus and DVR in the context is illustrated. A thick-CPR in this case may not only implement MIP, but can also aggregate the data samples within the slab using shaded or unshaded DVR. Thick-CPRs alleviate the problem of imprecise vessel centerlines, which is especially important for small vessels. The VesselGlyph in Fig. 5.4f describes a CPR rendering where the information in the context area is fading out. Data far away from the vessel center are thus not rendered. This ensures that the important focus information immediately stands out in the resulting images. Fig. 5.4g describes a Foreground-Cleft VesselGlyph, where DVR is used both for focus and context. To allow a clear view of objects in focus, the VesselGlyph ensures that objects in front of the focus region are suppressed. The Foreground-Cleft VesselGlyph can be completed with 'occlusion lines' indicating front-to-back spatial ordering of objects (Fig. 5.4h).

In the following we investigate the properties of images generated by various configurations of the Vessel-Glyph. Special attention is paid to the ability to display vascular detail and anatomic context simultaneously.

5.5.1 CPR+DVR VesselGlyph

CPR images are very important for vessel investigation in the clinical environment. The radiologists prefer them mainly for their ability to show the vessel lumen—to see whether a plaque or calcification occludes the vessel partially or fully. On the other side, CPR images lack context information. Therefore we propose to use CPR only in the focus region and apply DVR in rendering the context area (Fig. 5.4c). There is an abrupt change between the two regions (Fig. 5.5a).

Visualization with the CPR+DVR VesselGlyph can be performed in color or in gray-scale. Color images create higher contrast between different tissues, while the gray-scale images retain 12-bit gray-scale information. This is important in the clinical environment, because radiologists are used to 'window' the investigated images. The 'window' shows only the relevant range of densities. This helps to emphasize the information that would be suppressed in case of resampling of 4096 possible gray levels in the CT data to 256 levels of gray in the PC workstations. Advantageous is the combination of color DVR context and gray-scale rendering of the focus area with the 'windowing' possibility.

5.5.2 Blended CPR+DVR VesselGlyph

Here we propose a transition area between the focus and the context area in the VesselGlyph (Fig. 5.4d). This eliminates the sometimes disturbing abrupt transition in images produced with the CPR+DVR VesselGlyph. The crossover region ensures a smooth transition from the technique used for the focus area to the technique used in the context area. This can be implemented in various ways, e.g., by linear interpolation of both techniques or by changing the width of the context within the transition area. Fig. 5.6a shows an example of such a blended VesselGlyph.

(a)   (b)
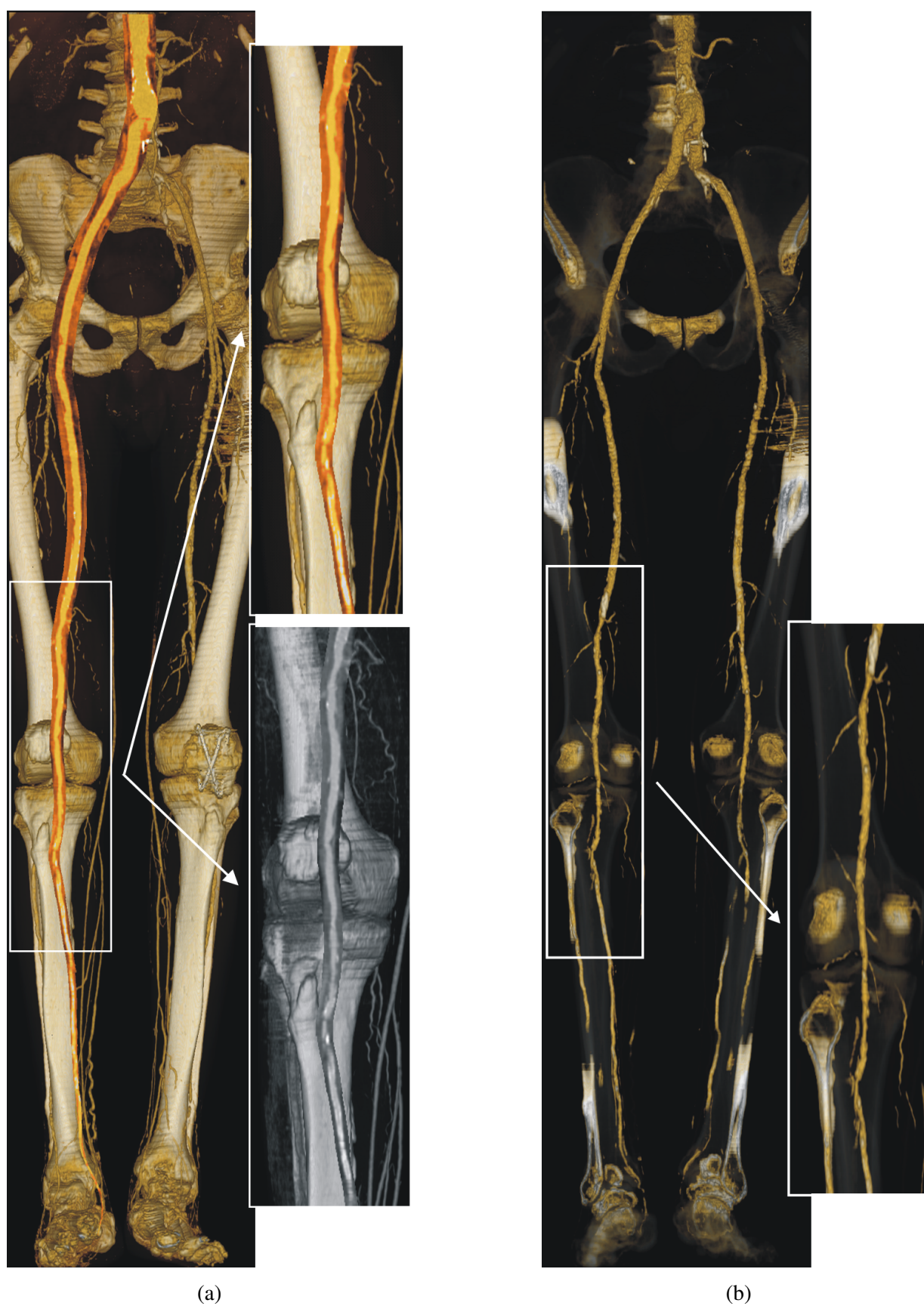
Figure 5.5:   *(a) Application of VG with CPR for focus and DVR for context (DVR+CPR VG), (b) Thick-Slab VG rendering; context is rendered very transparently and slab in focus is rendered rather opaque.*

5.5.3 Foreground-Cleft+DVR VesselGlyph

CPR images provide a good view of the vessel interior; but do not give sufficient information on the overall vessel shape and its front-to-back spatial ordering. Moreover, they fail to visualize thin vessels, when the centerline is incorrectly identified. In these cases, the radiologists prefer DVR images. As mentioned before, object occlusion is a problem here. Therefore, we propose a VesselGlyph, which ensures that the objects in front of the focus region will be suppressed, resembling a cleft in the foreground (Fig. 5.4g, Fig. 5.4h).

For DVR visualization of vessels, one has two possibilities – either to show the entire vessel or to show the vessel interior. The first case we call full-vessel configuration (Fig. 5.3b). The second case we call half-vessel configuration (Fig. 5.3c). The Foreground-Cleft VesselGlyph prevents the loss of spatial arrangement information. To emphasize this information in images, we suggest to render occlusion lines (Fig. 5.6b) which indicate whether the area of focus is behind the actual object. Using this concept, the investigation of otherwise occluded objects is possible and the front-to-back information is still available.

5.5.4 Thick-Slab VesselGlyph

The CPR+DVR VesselGlyph or the Foreground-Cleft VesselGlyph show clearly and correctly the focus regions in their context. However, the radiologists are also sometimes interested in other structures surrounding the main vessels, e.g., collateral vessels. These structures lie in the context area of the previously mentioned VesselGlyphs where they might be occluded by dense objects, e.g., bones. As mentioned above, this problem is partially solved by CPR or thick-CPR, which are actually special cases of the proposed Thick-Slab VesselGlyph.

The Thick-Slab VesselGlyph has a focus region in the shape of a slab curved along the vessel path (Fig. 5.4e). We have several possibilities how to render this VesselGlyph. The context region can be set fully transparent and MIP can be used in the focus area (which is actually the thick-CPR technique of Kanitsar *et al.* [16]). As an alternative, DVR can be used within the focus with the context area set either fully or partially transparent (Fig. 5.5b). Fig. 5.6e shows a half-vessel rendering of Thick-Slab VesselGlyph. The thickness of the slab may also be varied along the vessel tree, e.g. thicker for the aorta, and thinner for crural arteries, respectively.

5.5.5 Tubular VesselGlyph

In case the radiologists want to see vessels clearly depicted within the suppressed context, we propose the VesselGlyph illustrated in Fig. 5.3d and Fig. 5.3e. DVR is used for both focus and context, but the context is rendered very transparently, giving only supplementary information, whereas objects in focus are rendered photo-realistically and in high quality. Fig. 5.6d depicts a half-vessel rendering and Fig. 5.7 shows a full-vessel application of the Tubular VesselGlyph. Note, that bony structures in close vicinity to the vessels of interest are also fully rendered. This may cause 'pseudo-calcifications' of the vessel wall, or small areas of occlusion. Changing the viewing direction may alleviate this problem. This problem results from the fact that we do not have precise information about the vessel diameter in a given point. We only estimate this value and therefore the focus region can include also objects that lie in close vicinity of the vessels, e.g. adjacent bones.

5.5.6 Multi-Path CPR+MIP VesselGlyph

A very promising VesselGlyph seems to be the combination of multi-path CPR (mpCPR) and MIP (Fig. 5.8). In plain MIP images with out-segmented bones the vessel lumen can be obscured by calcifications or stent
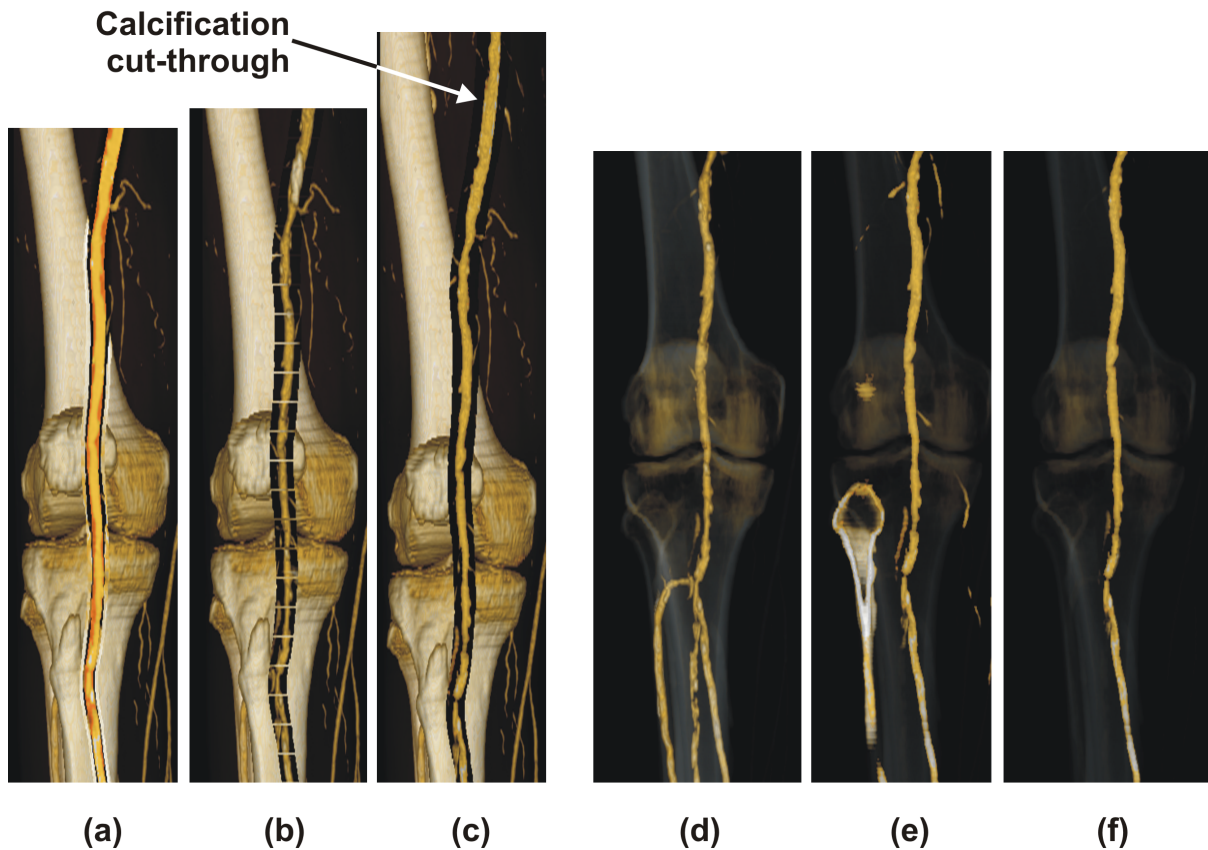
Figure 5.6: *VesselGlyph close-ups of a knee area for: (a) CPR blended in DVR, (b) Foreground-Cleft with occlusion lines (fullvessel), (c) Foreground-Cleft (half-vessel) (d) Full-vessel rendering with a Tubular VG (multi-path version), (e) Half-vessel rendering with a Thick-Slab VG, (f) Half-vessel rendering with a Tubular VG.*

implants. The CPR show vessel lumen (which is the main subject of examination) clearly, but the anatomical context is lost and collaterals are not visualized (Fig. 5.9). Thus, in a combination qualities of both can be retained. The width of the mpCPR portion is dictated with the identified radius of the vessel. This combination received significant interest in medical environment and therefore is undergoing thorough testing and evaluation to determine its usefulness and qualities in everyday clinical practice.

If results of such combined VesselGlyph are to be used for diagnostic purposes one limitation has to be taken in account, possibly checked and corrected during the data-processing phase. If the diameter is identified larger as should be, an impression of 'pseudo-soft plaque' close to vessel border might arise (Fig. 5.9). We explain this phenomenon by the fact that MIP images appears 'brighter' compared to mpCPR, even with same 'windowing' setting. The higher brightness of MIPs is given mostly by a projection of denser soft tissues (e.g. muscles or inner organs); whereas the close vicinity of vessels in mpCPRs consists mostly of fat that is less dense. Thus, if the mpCPR portion includes also voxels belonging to structures neighbouring the vessels from outside, darker areas appear in the merged images. In results an impression of a darker band is created what resembles soft plaque. Therefore, proper identification of vessel diameter is crucial if such VesselGlyph combination is to be used.

In certain cases, small underestimation of the vessel diameter might reduce unwanted artifacts of this kind,

(a)   (b)   (c)
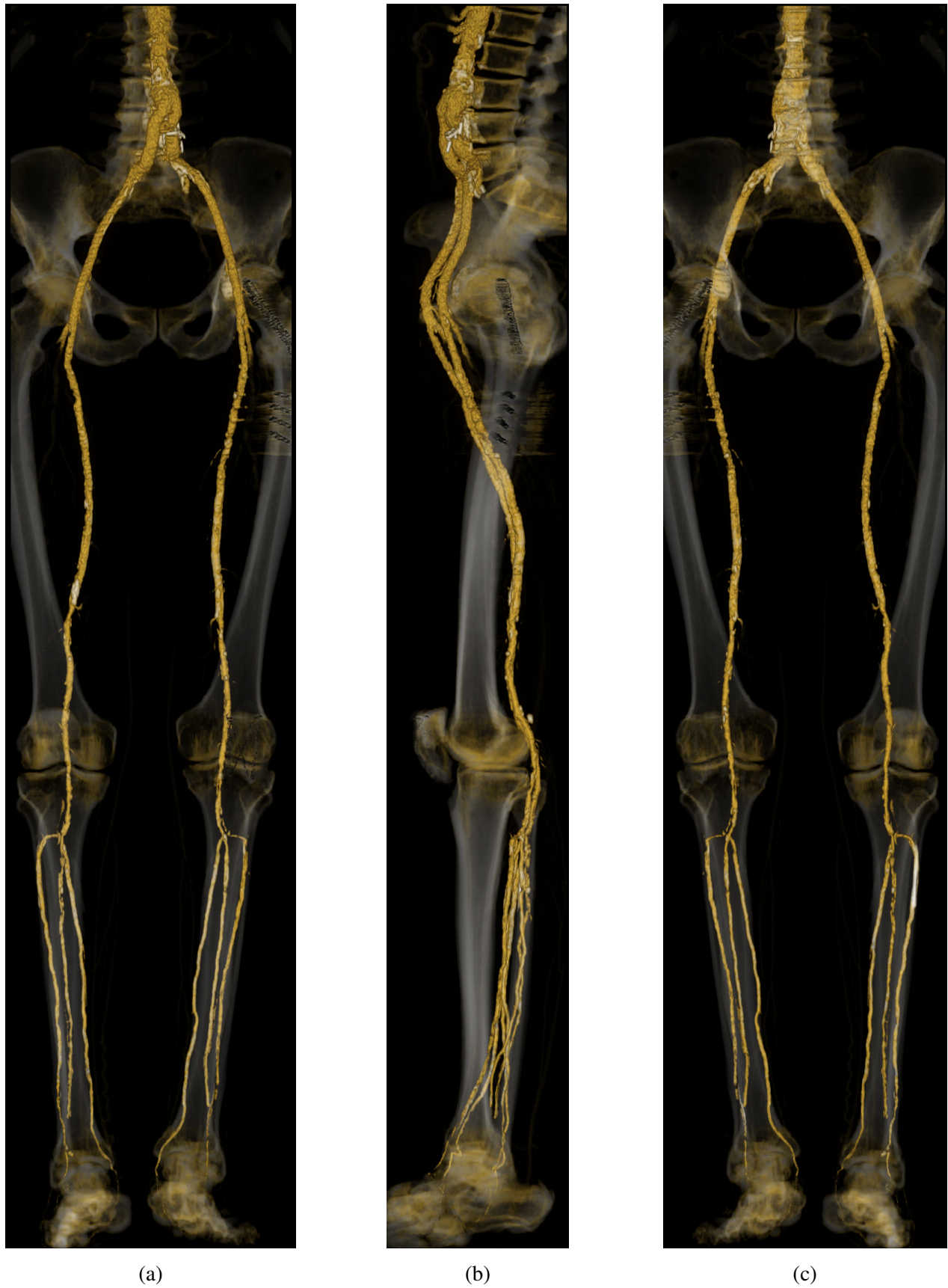
Figure 5.7:   *Full-vessel Tubular VesselGlyph: (a) frontal view, (b) lateral view, (c) rear view. These images show the multi-path possibility of the VesselGlyph.*

playing on the fact that walls of the vessel are rendered the same in mpCPR and MIP images, only the central part (the lumen) is rendered differently. Thus, using different technique in the inner part of the vessel is sufficient and potential artifacts are then reduced, without lowering the clinical quality of the pictures.

Nevertheless, significant underestimation (>30%) of the radius also leads to incorrect images, e.g. for larger calcifications where the visualized lumen will be rendered narrower as in reality. Therefore, precise identification of centerline and radius of vessels is an absolute prerequisite for mpCPR+MIP VesselGlyph.

5.6 Implementation Details

The VesselGlyph is a generalization of vessel rendering techniques. It includes multiple visualization techniques that are merged in final image. To achieve this merging the rendering with different techniques can be implemented either by assembling of two independently produced images or the result can be formed in one step with varying parameters pf the rendering algorithm. The example of the first is e.g. the mpCPR+MIP VesselGlyph (Subsection 5.5.6), where two independent visualization of the vascularity are created and then merged on the tree hierarchy and segment diameter.

Alternatively, the VesselGlyph can be implemented as an extension of the DVR algorithm, where a transparency modifier is assigned to each volume element through the VesselGlyph. The value of the modifier is based on the orientation and the distance of the actual volume element to the vessel centerline. This modifier later controls the transparency function in the DVR stage.

As described in Tab. 5.1, image generation using the VesselGlyph is currently with an unoptimized implementation not possible in real-time. The off-line generation of images takes a significant amount of time, which only allows the user to see pre-computed images for a limited number of view angles. Therefore we investigated the possible acceleration by modern graphics hardware in the image production stage. Modern graphics hardware, driven by the gaming industry, have evolved rapidly. Today, many graphic accelerators support 3D textures and are usable for 3D volume visualization [163, 164].

Visualization of 3D textures is done by defining of a set of cut polygons with specified 3D texture coordinates. These 2D polygons are then rendered taking advantage of hardware interpolation of the 3D data to 2D planes. The texture unit of the GPU maps the densities to colors and transparency values which are used for direct volume rendering. This part of the GPU is user-programmable (fragment program) and can merge different 3D textures in the rendering stage. In our case, this feature can be used then for multiplication of the transparency of the original data with the transparency modifier at a given location.

Using this approach we were able to render datasets of $512 \times 512 \times 128$ voxels with 256 cutting polygons in 2 fps on an nVidia 5700 GPU with 128 MB RAM. The 128 slices is the maximum size of the dataset due to the RAM size on the graphics card. We expect that in the future hardware-supported rendering of full-sized datasets will be possible. To overcome this problem today, we developed a system, where slabs of 128 slices each are rendered sequentially and the final image is composed part by part.

5.7 Conclusion on Visualization

In the previous sections, we proposed and discussed visualization of vessels in pCTA data, aimed for its application in regular clinical practice. Such images must sufficiently visualize the pathologies in a natural way. We showed that in case the individual simple rendering techniques are suboptimal due to introduced limitations,

Computation time for:	Software (Athlon 1.4GHz CPU, 2GB RAM)	Hardware (nVidia 5700, 128 MB RAM)
VesselGlyph Transparency Modifiers	1–5 min	—
DVR with transparency modifiers	10 min	0.5 min

Table 5.1: *Computation times for pCTA dataset (512×512×1298) pre-processing with the VesselGlyph and image production based on the VesselGlyph (final image: 724×1298 pixels, 2× oversampling in viewing direction)*

techniques can be combined for better results, e.g. by means of the proposed VesselGlyph concept. Some of the designed combinations require only minor modification of the existing tools to create the images (e.g. for mpCPR+MIP combination), but most of them require more complex modifications of rendering algorithms to employ the required variability of parameters, e.g. that control transfer function in DVR. For clinical usage, real-time implementation of such renderings are also needed, to allow systematic exploration of possibilities that VesselGlyph offers. In future, this can be achieved either by CPU-based optimization of the algorithms or by introduction of HW-acceleration by means on modern graphic cards.

For a potential future work we identified within our research the following guidelines:

- **Visualization approach:** As described in Section 5.1, either natural 'photo-realistic' visualization depicting the dataset in a 'natural' way can be employed, or dedicated signal 'information visualization' can take place. In our cooperation with clinical experts we found out that only 'natural' visualization (MIP, DVR, CPR) are welcome for pCTA processing. Derived information (as e.g. ratio of calcification along the vessel path) is not accepted. We explain this fact by the observation that visualization based on MIP/DVR/CPR is less prone to misinterpretation (which might result from incorrect data processing and reconstruction errors). For a skilled radiologist it is possible to recognize if artifacts or misclassifications of tissues are present in the output images, by subconscious recognition of context information. Derived images displaying only some kind of signal or measure lack this complementary information, hence are less reliable and may potentially lead to wrong results. Therefore, we expect 'natural' (MIP/DVR/CPR) visualization to be most suitable for pCTA data visualization. Recomputed information can be introduced only as additional or complementary measure, displayed e.g. as a side-bar.

- **Density vs. mapped rendering:** For 'natural' visualization, two distinctive approaches are used for data projection: direct projection of density values (MIP, CPR) and mapping of density values to properties that are used in later computation of the projection (DVR). Mapped techniques are therefore dependent on parameter values that provide the mapping and therefore may potentially fail in visualization of important features, if the parameters are set incorrectly. Inability to display important features exist also for MIP (e.g the occlusion problem) and CPR (e.g. incorrect reconstruction of vessel centerlines leads to a pseudostenosis problem) images, but the fact the these images retain full 12-bit gray-scale information reduces certain risks. We presume that under these considerations visualisation methods displaying original densities are slightly more suitable than approaches employing density mapping.

- **Focus and Context Visualization:** Focus & context visualization seems to gain significant importance for data visualization these days (e.g. Viola [162]). For this, decomposition of the data to allow iden-

tification of the included objects or tissues is needed, typically by means of voxel labeling. Then, this information is used to determine rendering properties for individual objects, if items in focus shall 'stand out'. Hence, application of focus and context approaches solves two problems: first, allows unoccluded view of objects in focus; and second, allows completion of image with proper context, in areas where the focus-rendering did not bring understandable, intuitive information. In such setting, application of focus and context techniques is very suitable for vessel visualization.

A partially unanswered question in this field of research remains the issue what to visualize and how. A clear answer on to what extent do the overall vessel tree shape and its hierarchy, the curvature of segments, the highlighted visualization of calcifications and soft plaque and other aspects influence the diagnostic value of the images is not known yet. Also, requirements on the image resolution, gray-scale levels and final composition of rendering techniques must be answered, first by the clinicians themselves. These questions are important; they remain a challenge independent of the used modalities and quality of the scanning devices.
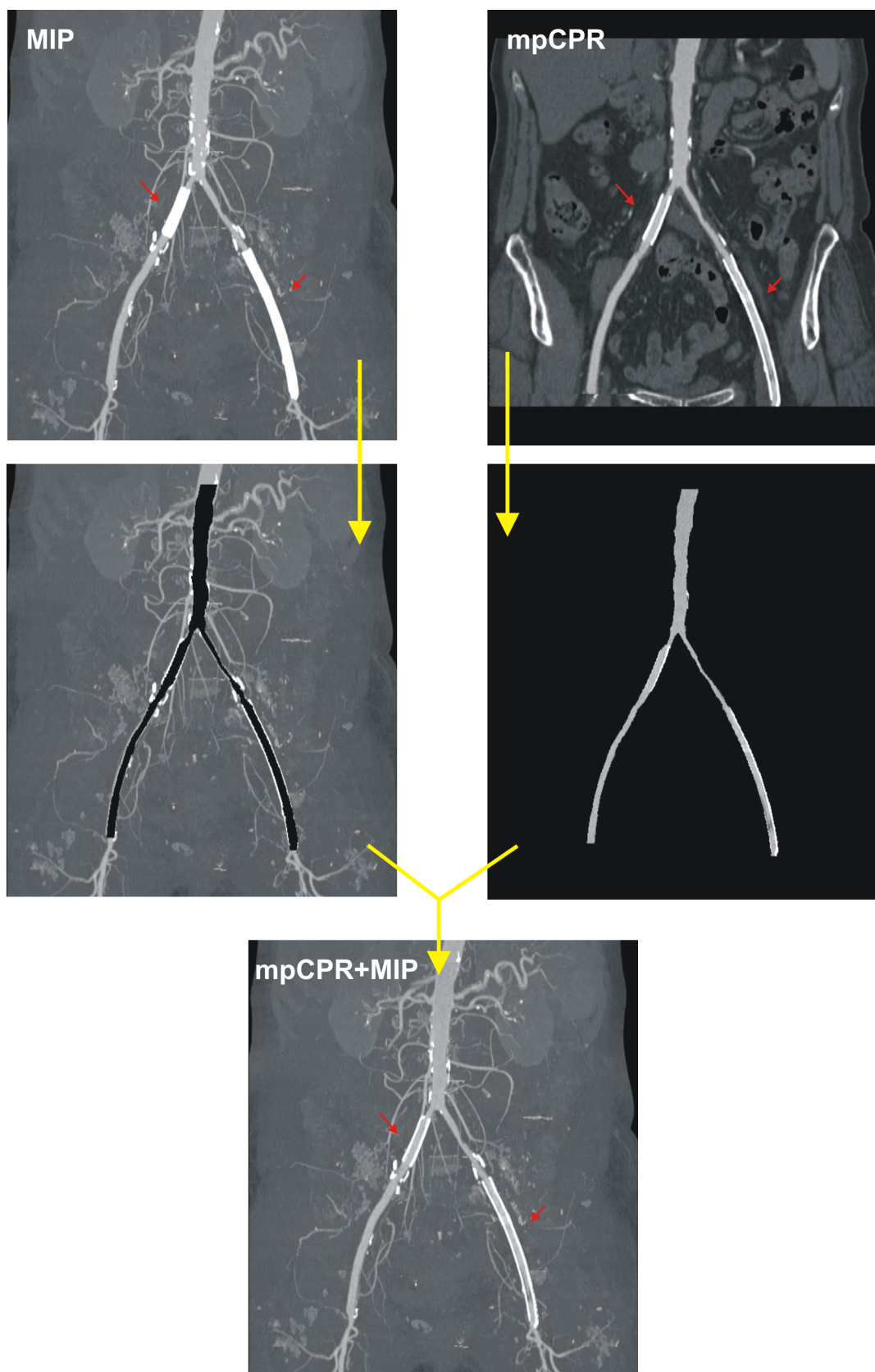
Figure 5.8: *Multi-path CPR+MIP VesselGlyph and image generation. Multi-path CPR (mpCPR) showing vessel lumen is used for focus and MIP is used for context, depicting collateral vessels and giving overall anatomic orientation. (Compare areas indicated by red arrows in MIP, mpCPR and combined images.)*
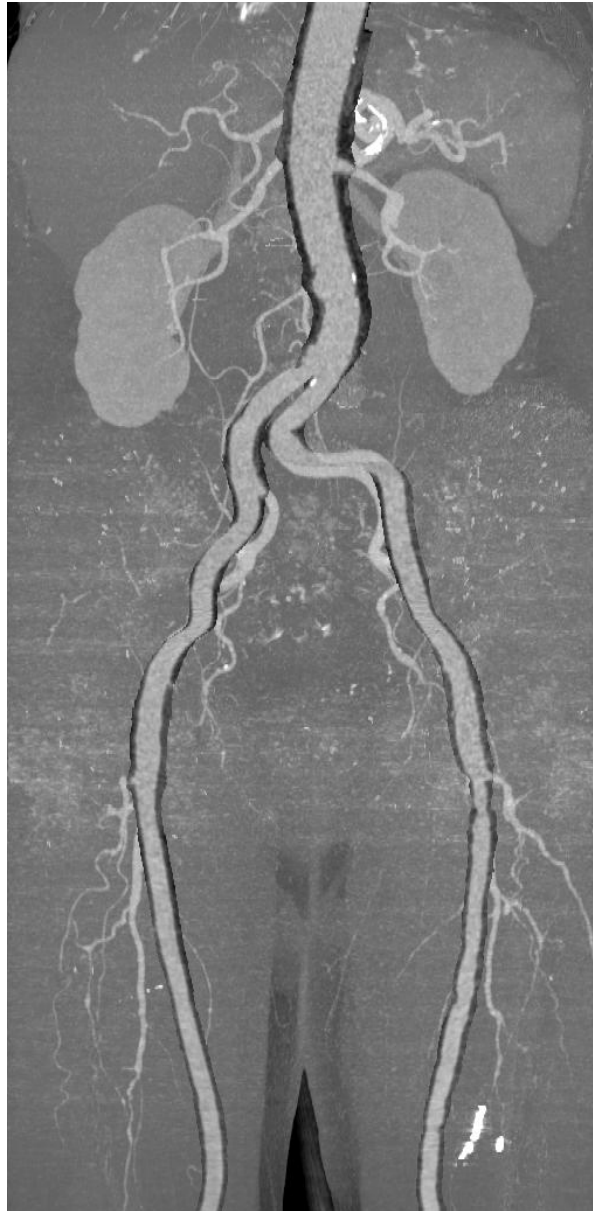
Figure 5.9: *Result of multi-path CPR+MIP VesselGlyph with incorrectly identified vessel diameter, resulting in impression soft 'pseudo soft-plaque' in the vessels (see text for further explanation).*

Chapter 6

Software Implementation

6.1 Introduction

Processing of peripheral CT-Angiography data is a task determined by real demands of clinical experts. Therefore, the focus of the research should not only be on the design of particular algorithms, but also on their practical implementation—to allow their usage in daily clinical practice. To support our research, we developed and implemented a complete medical workstation software aimed on pCTA data processing. Building such software package is a rather complex task and in the following the main design issues are discussed.

In implementation of such a complex software several aspects need to be addressed. First, an overall system composition must be analyzed to specify which modules are necessary. Functionality of individual modules is determined by user requirements, developed algorithms and their control interface. This altogether builds a general architecture of the system. Also concrete practical issues of the architecture design must be considered. To support easy development, stability, possible simple extendibility and to allow further prototyping and extensions, the system must be implemented as a very flexible one. Sufficient adaptability and variability of the system can be ensured e.g. by a plugin design.

A significant part of software design, determining the overall quality and performance are the data structures. This is an important issue especially in the case of pCTA data because of its enormous size, often reaching the physical limits of the current hardware setups. Therefore, as another aspect of the design, data structures that help in reducing memory requirements, yet ensuring fast access to its elements, are required.

There already exist numerous software packages, aimed on processing of medical data or on processing of images and volume data in general. The medical processing software is often commercial and proprietary (e.g. Siemens Syngo software, Siemens LEONARDO workstation, Viatronix V3D system, Vital Images Vitrea software, Barco Voxar3D software, Agfa IMPAX system, GE Advantage Workstation, TeraRecon AquariusNET system, Tiani JVision software, dedicated Philips medical systems as Advanced Vessel Analysis, etc.) These are in most situations not suitable for research purposes, because their source code in not available. As a complement, several open source projects or packages with free license for academic purposes exist, e.g. MeVisLab (MeVis, Bremen, Germany) aimed on medical data processing, VTK/ITK packages (Kitware, Clifton Park, NY, USA) or Julius Caesar software platform (Caesar Research Centre, Bonn, Germany), among others. Some of these offer a suitable base for further academic research and implementation.

In our research environment, certain code was already implemented and available as a result of a previous research ([15, 16]). Therefore, we decided to utilize the knowledge incorporated in it, but simultaneously we

also decided to rewrite it completely, in order to prevent potential problems with intellectual property rights in the future. In the next sections, we describe our proposed software solution, named the *AngioVis ToolBox* (AVT) that was used to implement and evaluate the algorithms described in the previous chapters. The system has been installed in General Hospital in Vienna, Department of Angiography and Interventional Radiology, and used on a daily basis (up to 10 patients per week are processed, altogether up to 400 patients since the program introduction), what proved its qualities and clinical relevance. The *AVT* software has been also presented several times to the scientific community (e.g. Straka *et al.* [165]) and was also awarded a 3rd place Medical Prize Award on the Eurographics 2005 Conference in Dublin, Ireland. The software has also been installed in few other places for PAOD research purposes (e.g. Stanford University Medical Center, California, USA). The proposed system was implemented in C++ (Stroustrop [166]) under the Microsoft Windows 2000/XP operating system. The Qt multi-platform library (Trolltech, Norway) is used for the user-interface and the graphic support of the system is based on OpenGL. Such combination proved to be flexible and stable and ensures the possibility for porting it to other operating systems (Mac OS, Linux) in the future.

6.2   Main Modules

In the previous chapters, various aspects and properties of individual pCTA data processing steps were discussed. The pCTA data workflow pipeline itself was introduced in Section 2.3, where the main steps were identified:

- Data acquisition (scanning),
- Tissue segmentation (bone, vessel, soft tissue labeling, etc.), background identification and removal,
- Vessel tree extraction and modeling,
- Data resampling and generation of visualizations, and
- Image storing in a clinical Picture Archiving and Communication System (PACS).

In the beginning, the patient is scanned to assess the potential pathologic changes in the body. The scanning produces a volumetric dataset that has to be processed to derive images holding diagnostic information. Such images are then interpreted by experts for treatment purposes. A system aimed on processing of pCTA data then must consist of several modules, as pictured on Fig. 6.1.

The processing works as following: the scanned data must be first labeled for tissue type. In the proposed *AVT* software, this segmentation and classification (refer to Chapter 3) is provided in a module named *Bone Remover*, because its main purpose is to label and out-segment bone tissue for 'boneless' MIP images. Secondly, a vessel tree is reconstructed from the labeled dataset by means of the vessel-tracking techniques (Chapter 4) in a module called *Vessel Tracker*. Its purpose is to derive a geometric vessel tree model, providing information about vessel centerlines, diameters and vessel tree hierarchical organization. In the last step, the tree information and labeled volume data are exploited in a module named *Image Series Output*, which produces a set of visualizations of the pCTA data. These views, stored in the DICOM format, display the dataset from various view-angles and are organized in so-called series to allow their easier management and retrieval in PACS.

In the Fig. 6.8 the block scheme of our pCTA processing system is depicted. The system design can be analyzed in two ways:

- **Vertical analysis**: Memory structures representing and holding the data (the volume grid and vessel tree model) are the lowest part in the hierarchy. The data are then used in a layer of 'general' algorithms, as are e.g. the visualization techniques (volume data are needed in MIP, CPR and DVR modules, but the

vessel tree is required only in CPR module) We call these algorithms 'general' because their outputs are used in several next steps.

The next above layer are the dedicated algorithms, aimed on specific processing of the data. These can often require user-guided definition of parameters. The actual user interface is provided in the highest level, typically consisting of windows, buttons and other widgets and serves for communication between the user and the algorithms guided by the input parameters. Depending on the complexity and mutual dependency of the algorithms, the layer of dedicated algorithms and the user-interface layer can be merged into one. This is mainly true for simple processes with immediate response to user events (e.g. changing of value of an individual voxel), whereas for more complex algorithms that require longer computation times (e.g. vessel-tracking and path-centering) it proved to be appropriate to separate these two layers. If so, then the user interface just provides input parameters to the underlying layers. Because of this, the user
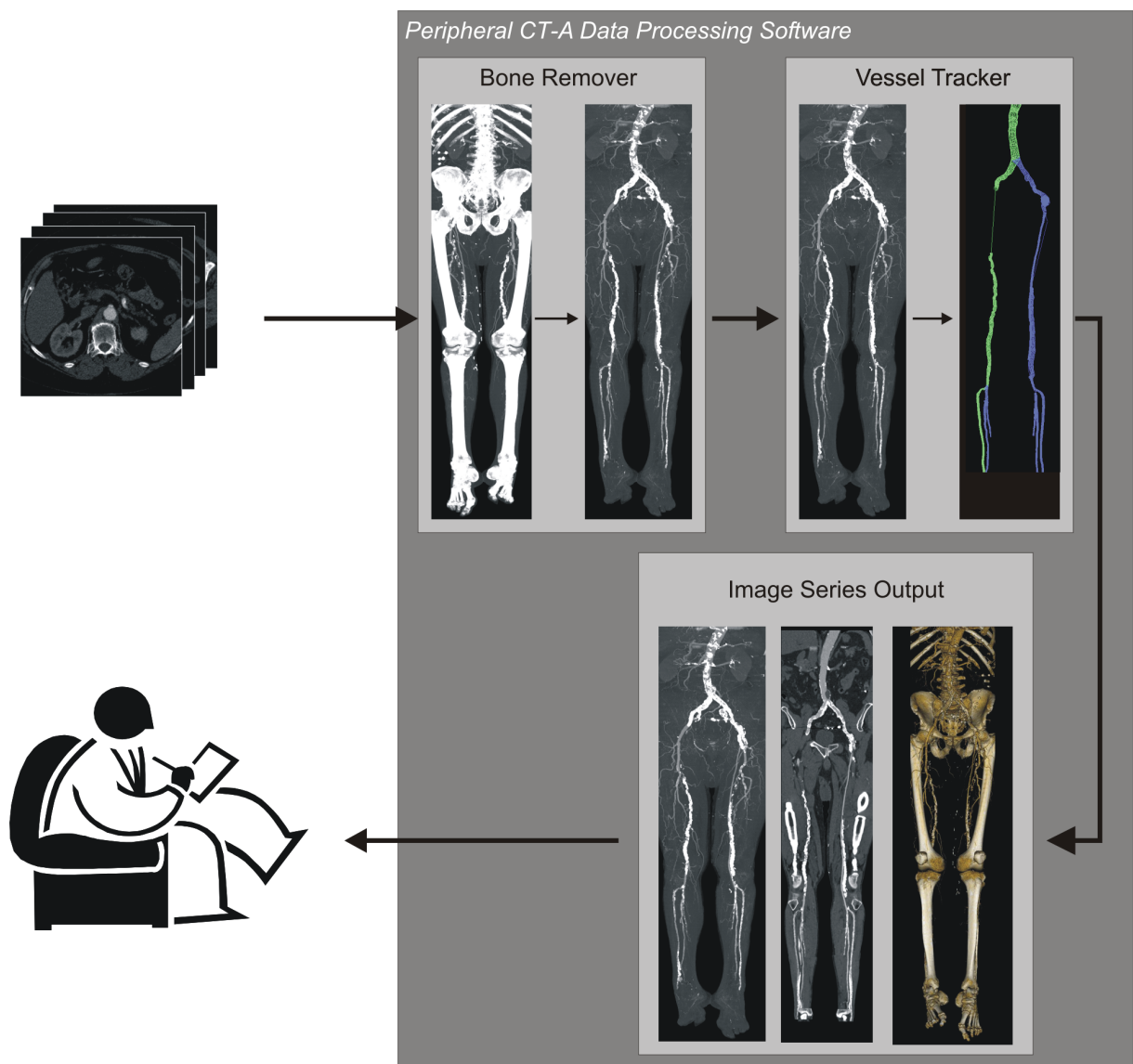

Figure 6.1: *Main modules of a software aimed on processing and visualization of pCTA datasets. Input data is first segmented, then vessel tree is reconstructed. In the last step, clinical visualizations of the data are created, followed by their storage in PACS systems and diagnostic interpretation.*

interface layer can be implemented not only by means of a local GUI system, but also as a client-server system (e.g. by a web-browser interface) if the future shows this as necessary or appropriate.

- **Horizontal analysis**: If analyzing the block scheme in a horizontal manner, the main module decomposition (see Fig. 6.1) can be recognized:

  First, the bone removing (the tissue segmentation) is executed. Within this step, slice and MIP view are needed, being necessary for operator navigation within the designed semi-automatic segmentation algorithms. Here, the volume data is segmented, classified and complemented with tissue labels (indicated by the red arrow in Fig. 6.8). In the Vessel Tracker stage, the vessel tree model is built, enabling to create CPR views of the data. Within this module various visualizations as MIP, slice view and CPR are employed to support the user navigation in the dataset and also dedicated algorithms for vessel-tracking and path-centering, manipulation of the vessel tree, etc. are applied. In the last step, named Image Series Output, the final images are produced. Due to the size and applied interpolation filters this may be a lengthy task taking up to 30 minutes on current PC workstations. These images also have to be organized into so-called series compatible with the DICOM standard. The last module automates this and thus removes the burden of manual image export from the operator. Within this block, the data (volume grid and vessel tree model) and also visualization algorithms (MIP, CPR, DVR, ...) are exploited, as seen on Fig. 6.8.

An example of implemented user-interface for the mentioned modules can be seen in Appendix A. According to our experience, Figures 6.1 and 6.8 show a minimal set of functionality that is required for processing of pCTA datasets in a clinical environment. The presented setup forms the majority of the system installed in the aforementioned hospitals. For regular usage, such system must be operated by a trained user, as the most of the algorithm are not yet fully automatic. Much effort is being invested into research to make various aspects of the software more automatic and less labor-demanding, to allow fast PAOD diagnostics in future, what is a prerequisite for regular screening of the disease in the human population.

For daily clinical routine, the presented setup has to be complemented also by modules responsible for easy data retrieval (e.g. a database of datasets where these are identified by patient name, date/time, etc.) and modules holding patient information as gender, age, stage of the disease etc. Depending on the actual installation, also modules providing DICOM connection to the CT scanner and PACS system might be required. These tools might be either of commercial origin or research subjects of their own; in both cases is their description beyond the scope of this thesis. In the case of interest, we kindly recommend the reader e.g. the DICOM Toolkit (dcmtk package by Offis, Germany [167]) for further study.

6.3   Plugin System

A software package, as described in the previous section, which is used both in daily clinical practice and for research and prototyping purposes is expected to be stable, reliable and effective on one side, with high flexibility and simple extensibility on the other. These are sometimes antagonistic requirements—adding and evaluating new functionalities may influence the existing features and lead to instability.

Flexibility and mutual internal independence of the code is required, to allow having both working code and a development version. Therefore, we proposed to implement the system as a set of code blocks, organized in a hierarchical manner that utilize only *run-time* mutual dependency. This allows to create a system, where blocks can be easily added and removed, without the need to modify the source code. Thus, the version for clinical

application can contain only reliable and stable modules, whereas in the research version new algorithms can be tested without the need to supervise two versions of the code.

6.3.1 Implementation

A modular system having the required flexibility is expected to load and register its modules dynamically, just in the time of the application start. A practical implementation of such *plugin* system can be based on the technology of *dynamically linked libraries (DLL)*, available in many modern operating systems—the .DLL modules in Microsoft Windows, .so modules in Linux, etc. The DLLs are libraries, in which the code is shared among multiple programs, saving both disk and run-time memory space. The binding between a code already loaded in memory (e.g. a code from executable file) and a code in the DLL is not fixed. This means that a call to a function that is located in a DLL is not statically linked, but instead it is directed to a *function pointer*. Assigning values of these pointers can be done either automatically (provided by a compiler) or manually, by searching for a function *name* and thus retrieving the function address. An example code snippet might look as (C++ code):

```
-----------------------------------------------------------------
typedef int (__cdecl* MultiplyNumbersFuncPtr)(int a, int b);


MultiplyNumbersFuncPtr multiplyNumbersFunc;
DLLHandle libraryHandle;


libraryHandle = loadLibrary("example.dll");
multiplyNumbersFunc = (MultiplyNumbersFuncPtr)GetProcAddress(
        libraryHandle,
        "multiplyNumbers");


if (multiplyNumbersFunc)
{
    int a = 7;
    int b = 4;
    int result = multiplyNumbersFunc(a, b);
}
-----------------------------------------------------------------
```

A simple function call to an acquired function address (with suitable number of parameters) executes the function code. The limitation of this approach is that only pointers to static objects (i.e. global functions and global objects can be derived. If integration with object-oriented programming is needed, then access to objects via unified interface must be provided, allowing possible re-casting of the pointers later in the code. Thus, for management of the object only basic (inherited) class interface is needed, whereas for specific functionality the newly added methods can be provided by means of the mentioned re-casting. Together with the possibility of the DLLs to be loaded on demand and by accessing their global symbols, a copy of inherited class object can instantiated. An example of a code that allows instantiating different 'descendants' of the parent class in run-time dependency might be implemented as follows:

```
------------------------------------------------------------------
// parent.h
// Parent Class Definition

class MyObject
{
public:
     MyObject() { }
     // pure virtual function
     // must be redefined in child classes
     virtual int multiplyNumbers(int a, int b) = 0 ;
};
------------------------------------------------------------------
// module1.h
// Module 1
#include "parent.h"

class MyObject1 : public MyObject
{
MyObject1() { }
    // redefined function
virtual int multiplyNumbers(int a, int b) { return a*b; }
};

char* moduleIdentification() // returns a string with identification
MyObject* createInstance() { return new MyObject1; }
------------------------------------------------------------------
// module2.h
// Module 2
#include "parent.h"

class MyObject2 : public MyObject
{
MyObject2() { }
    // redefined function
virtual int multiplyNumbers(int a, int b) { return a*a*b*b; }
virtual int divideNumbers(int a, int b) { return a/b; }
};

char* moduleIdentification() // returns a string with identification
MyObject* createInstance() { return new MyObject2; }
------------------------------------------------------------------
```

For usage of the inherited classes in a system, the following construction can be applied:

```
----------------------------------------------------------------
#include "parent.h"
typedef MyObject* (__cdecl* CreateFuncPtr)();


MyObject *obj;
CreateFuncPtr createFunc;
DLLHandle libHandle;
List libraryList;

libraryList = findLibraries();                 // a function that searches
                                               // for available libraries
List::iterator it = libraryList.begin();
while(it != libraryList.end())
{
     String libraryFileName = *it;
     libHandle = loadLibrary(libraryFileName);

     createFunc = (CreateFuncPtr)GetProceAddress(
        libHandle, "createInstance");

     if(createFunc)
     {
          obj = createFunc();

          int a = 7;
          int b = 4;
          // will yield different results for module1 and module2
          int result = obj->multiplyNumbers(a, b);
     ++it;
}
----------------------------------------------------------------
```

In such way, modules derived from a base class can be loaded to the system via the flexible plugin system. If additional properties of the class interface (functions that exist only since certain level of inheritance) are needed, the object pointers can be manually re-cast and then accessed. During this re-casting, it is necessary to ensure that a base class pointer of only suitable modules will be modified (e.g. by checking the identification string for given module class), to ensure correct functionality. Otherwise access to such re-cast object might lead to unexpected results.

6.3.2   Plugin Management

The presented plugin system is not a novel concept. In software, plugins often work as 'replaceable' modules for different implementations of the same functionality. In this way plugins form a software counterpart to the hardware unification and module compatibility, allowing to use implementations of different producers to work in a particular system.

In a system, either some or all modules can be seen as plugins. If only some blocks are 'replaceable', then a fixed interfaced, dedicated for the given type of module is sufficient. If the whole system consist of plugins, then problem of flexible interface and code-reuse arise, together with the need to manage the modules.

The flexibility of interface was discussed in the previous section. The code-reuse, by which we mean that plugins (e.g., for visualization) can be used in different stages of the processing pipeline can be addressed by hierarchical utilization of the plugins, e.g. we allow to use plugins within other plugins. Such hierarchy need to be built and managed. A part of the system, that allows retrieval, loading and binding of individual plugins in the system is needed. In our system this is handled by a *plugin manager*, representing actually the basic level of plugin hierarchy. The duties of such plugin manager are loading of the libraries, holding the list of available plugins, instantiation and deletion of the objects, etc. An important feature of the plugin manager is the servicing of the requests for 'functionality'. In a flexible system, usually particular functionality is not identified exactly, but through 'potential capabilities'. A typical request in medical data processing algorithm can be e.g. a 'request for MIP visualization'—if a MIP image has to be created. In such case, the plugin manager searches the list of available plugins and returns the first plugin capable of producing MIPs, regardless of its origin and other properties.

6.4   Data Structures

Data structures and data organization in memory and on disks are important parts of programming (Wirth [168]). A good design of memory structures is important for overall algorithm efficiency—in this view, organization of data in memory *is* a part of the algorithm, as it influences the way how the data are accessed and manipulated. In the case of volume data, this becomes even more important—due to its size, which determines both the processing response and required memory space. If the data structures and the memory design are not concerned, it may happen that complexity of the algorithms grows to unbearable heights or the particular data cannot be represented and processed on a given machine architecture at all.

As depicted on Fig. 6.8, two main data structures are used in pCTA data processing: the volume grid with pCTA density information and a model of a vessel tree, representing the geometry and hierarchy of the vasculature. Effective and optimized implementation of these has a crucial influence on if a pCTA dataset can be processed on a regular PC workstations and if yes, then if with reasonable performance.

6.4.1   Volume Grid

The volume representing the acquired CT densities is the most important data structure in the pCTA processing system. It is a stack of 2D slices, constituting a 3D grid. Typically, there are up to 1200-2000 slices, 512×512 pixels each, with 4096 levels of gray. If the densities are represented as 16 bit integers, it renders a data size of up to 800 MB. If represented as 32-bit floating point numbers, it yields up to 1600 MB. Such sizes are acceptable only if no additional parallel volumes are needed (e.g. for vessel-tracking purposes, for gradient

image computation, etc.), otherwise the data do not fit to memory of the actual PCs. Moreover, we expect that in the future the number of slices will grow, taking the memory requirements close to the limit of current 32-bit operating systems.

On the other hand, pCTA data contain a lot of 'free space'—areas where objects or tissues unimportant for pCTA diagnostics are represented (air, scanner table, covering sheets, etc.) These can be removed from the dataset without influencing the clinical value of the data and can be replaced by a single constant value, e.g. by zero. In this setting, the main problem of the pCTA data—its size—can be solved by implementation of various kinds of run-length-encoding (RLE) schemes, for compressing the 'empty' space. Such approach leads to reduction of needed memory space, but access to individual voxels in such representation is less effective. In the case of pCTA data, the access and processing in such compression scheme should be not much less effective as access to simply represented data, in order not to deteriorate the system performance even more (processing of the pCTA data is computationally demanding even in an ideal case).

If considering efficiency of accessing the data elements, then the most effective and fastest solution for both random and sequential access is a simple pointer arithmetics in a linearly allocated memory block. In such case, the sequential access requires only one arithmetic operation on a pointer and random access requires only few additional computations.[1] It is evident that the sequential access is generally much faster then the random access. pCTA data processing algorithms consist of many sequential access operations; therefore the efficiency of sequential access significantly influences the overall performance of algorithms. In the following, we have focused on development of structures with fast sequential access.

Besides the possibility to fit actual dataset to available system memory and the duty to ensure fast sequential access, yet another two aspects that influences efficiency of data manipulation has to be taken into account, in respect of the planned visualization of the data (Chapter 5). Due to the size of the dataset it is not easy to ensure rendering at 'interactive' frame-rates; to achieve best results, two optimizations can be introduced:

- Firstly, the largest possible amount of elements representing the unnecessary information has to be omitted during the processing. Data structure should allow simple identification of larger empty areas, without the need the access individual voxels in them, by having information whether the block is empty or not as a result of preprocessing step. And

- Secondly, the volume elements which contribute to final image shall be accessed as fast as possible. This concerns not only individual voxels, but also their close neighbourhood (e.g. for computation of gradients, which are utilized within direct volume rendering — Fig. 5.1c). In current computer architectures, the data in processor cache are accessed several times faster then the data in main memory. Elements adjacent to processed element will be therefore accessed more rapidly if they are already loaded in the cache, what requires that spatially adjacent elements of the dataset must lie in close vicinity in the memory. This can be ensured by so-called block structure of the grid (for more details and evaluation of this phenomenon please refer to in the work of Grimm and Bruckner [169, 170, 171]). Such block structure groups represents the dataset not as linear array or individual 2D slices, but as a set of smaller 3D blocks. Within these blocks, elements that are spatially close are also nearby in memory space, what ensures more effective usage of the cache in processors and thus more effective processing and visualization.

Considering the above-mentioned requirements, we suggested a memory structure whose principles are de-

---

[1] Under a sequential operation in a 3D volume grid we understand a movement in 6- or 26-neighbourhood system, starting from a previously defined position. Under a random access we understand operations with explicitly defined values for all three coordinates, e.g. *get(x, y, z)*.
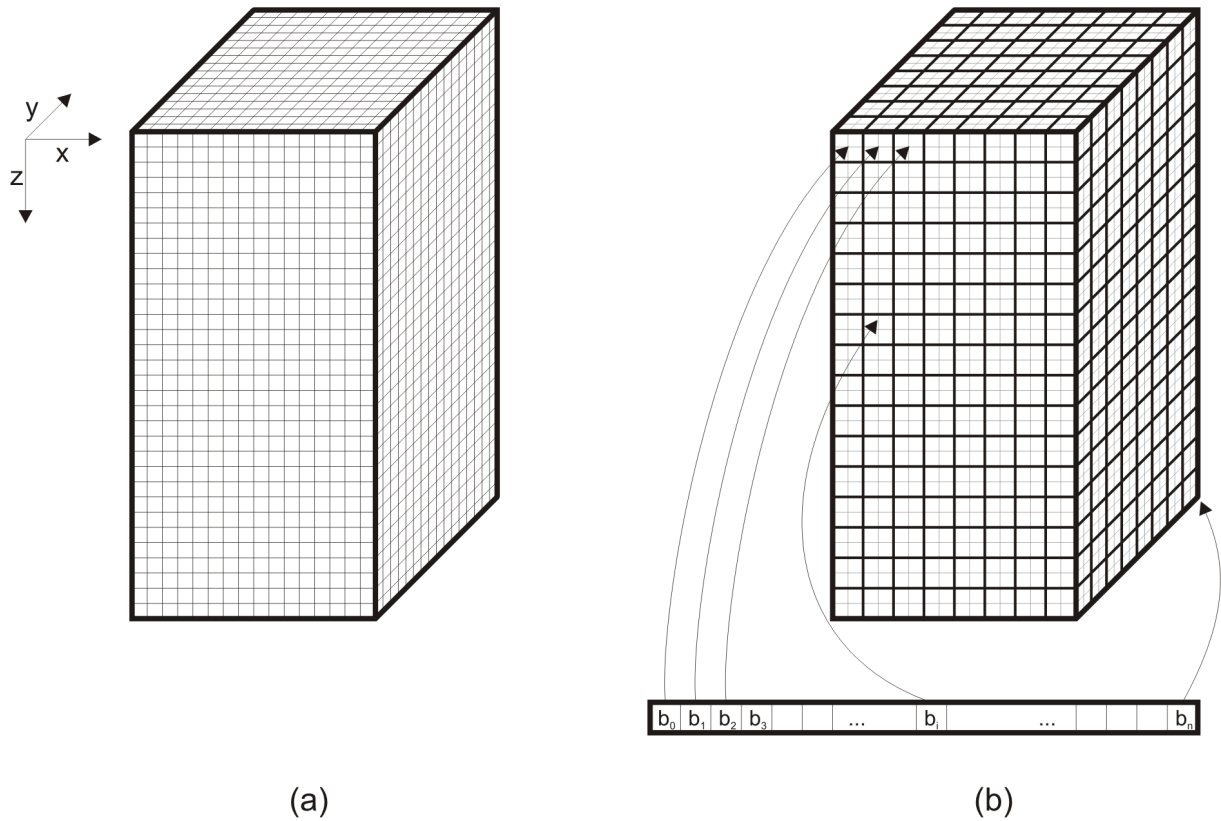
Figure 6.2: *Block memory structure. (a) Original volume dataset, (b) dataset divided into blocks. Blocks are independently allocated in the memory and references to them are kept in a list.*

scribed in next. The dataset (Fig. 6.2a) has a block represented in the memory (Fig. 6.2b); blocks are independently allocated and a list of pointers to them is kept, to allow access to them and their management. Structure of individual block is shown in Fig. 6.3: Each block holds a table of pointers to its neighbour blocks and a flag indicating whether the block represents relevant data or is empty If it contains relevant data, then the an own chunk of memory is allocated. If it is empty, then data pointer points to a shared empty block representation. Such empty block is represented only once in memory. The actual organization of the dataset in the memory is as depicted on Fig. 6.4. Thus, memory requirements are significantly lowered. The actual saving ratio depends on the type of data and pre-segmentation of the background areas, but for full-sized pCTA data is (according our experience), approx. 30–50%.

Accessing individual voxels in the proposed data structure is a complex operation. First, a block in which the particular element lies must be determined and then a position within the block must be computed. Such access is very slow; without dedicated sequential algorithms processing of pCTA data would take very long.

For optimized sequential access an efficient sequential access shall be similar to simple pointer arithmetics, both in programming usage and computational complexity. This means that a movement within the dataset—e.g. in a 26-neighbourhood, followed by dereference of a value—shall consist of not more then few arithmetic or memory referencing operations. In work of Grimm and Bruckner [169, 170, 171] a fixed memory addressing scheme was employed; this cannot be used here, as not all blocks are represented in memory and the sequence of block is arbitrary. Moving inside a memory block is trivial—simple pointer arithmetics suffices. The problems start when crossing the border of individual blocks—a 'jump' to a neighbour block must be provided. To

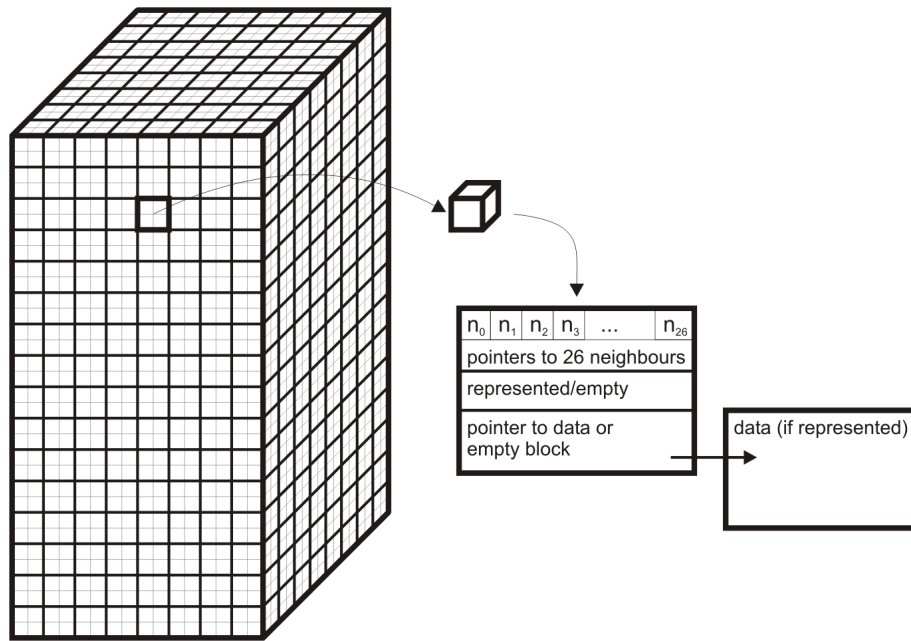Figure 6.3: *Data structure of a volume grid block. Every block contains a table of pointers to other 26-neighbour blocks and either allocated data or a reference to shared 'empty' block.*

achieve effective addressing, we proposed a scheme based on a so-called *adjacency block*, which is generally a type of a look-up table, holding an index to identify to which neighbour block we have 'jumped in' and an offset therein. For efficiency reasons, we proposed to introduce a concept of 27-neighbourhood[2] to allow also jumps inside blocks. The neighbour index in the adjacency block is translated to absolute address via neighbour address list, which is special to every block. To deference the value, the offset is added to the address of data for given block and the values are read, either in own data or in the shared block.

Structure and element of the adjacency block are shown on Fig. 6.5. The adjacency block is one layer thicker compared to data blocks, to allow handling of situations when the movement in the 27-neighborhood jumps 'outside' of the actual data block. Thus, the movement consists of two steps: first, a move in the adjacency block is done, deriving new block index and offset. Secondly, the pointer pointing to actual data element is computed and also the pointer in the adjacency block is updated, to handle cases when a 'jump' to other block was done (then a pointer in the adjacency block must return 'from other side', to reflect the block-border crossing), see Fig. 6.7 and Fig. 6.6. updating a pointer that points to data element, and also a pointer that holds pointer in the adjacency block (see

In this way, sequential access to the data elements requires only few arithmetic and memory access operations. The advantage of the approach is that is works independently on whether the actual data are allocated or just referenced to a shared empty block ; this property might even change during the run of the application. The proposed addressing scheme proved to be efficient and fast. The sequential access was implemented by means of *iterators*, which resemble pointers and the operations; programmer's usage of iterators is also similar to usage of pointers. This concept lowered significantly the memory requirements, allowing to process large data and leaving enough space for parallel volumes needed in certain algorithms. It also allowed more effective implementation of volume rendering algorithms, thus allowing faster image generation, with nearly real-time

---

[2]A 27-neighbourhood system is an extension of 26-neighbourhood system; the 27-neighbourhood system simply considers also the central element.
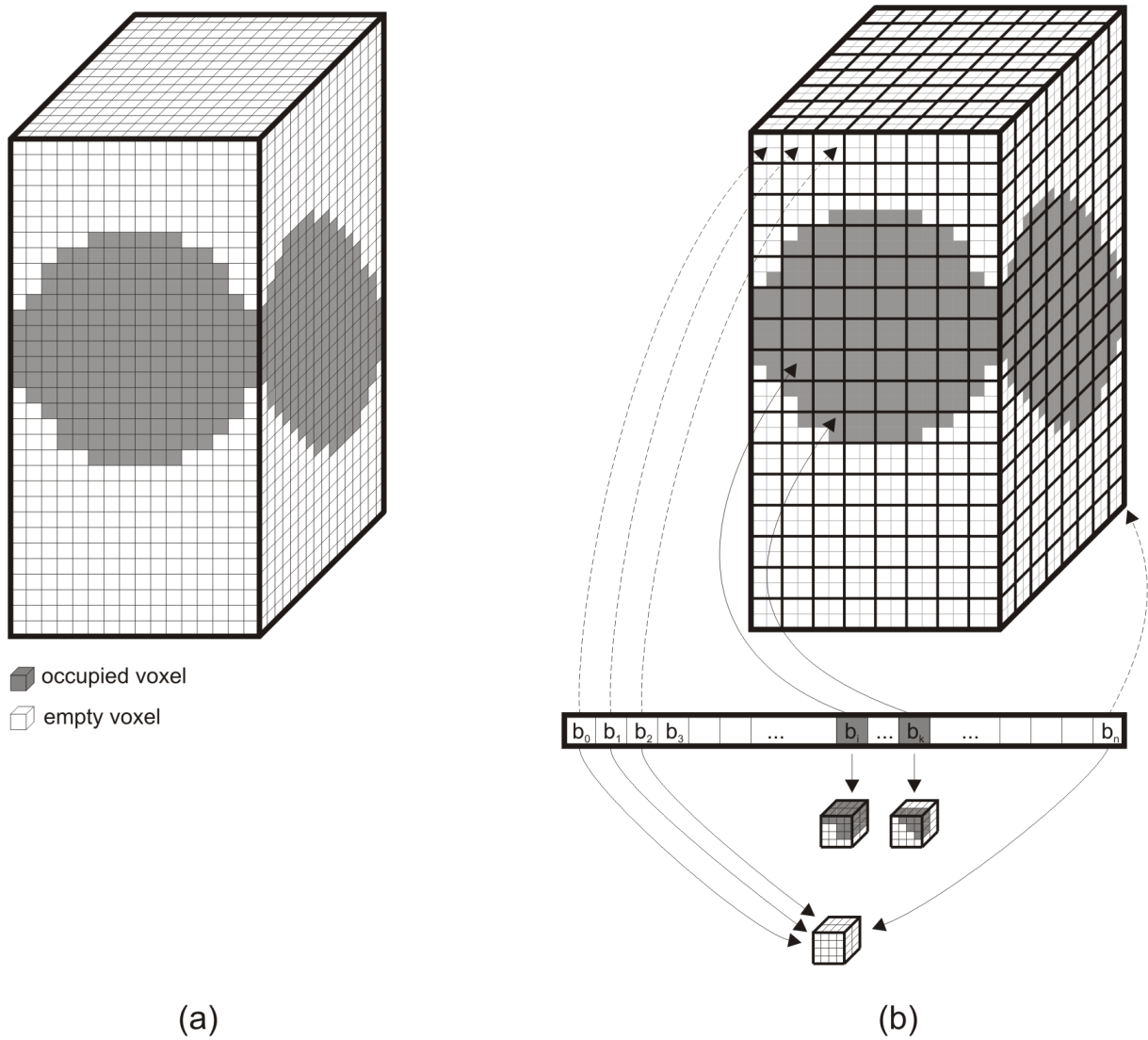
Figure 6.4: *Representation of occupied and empty block in the block memory structure. (a) A volume with empty and occupied elements. (b) Non-empty blocks are represented fully in memory, whereas empty blocks use shared representation of the empty data.*
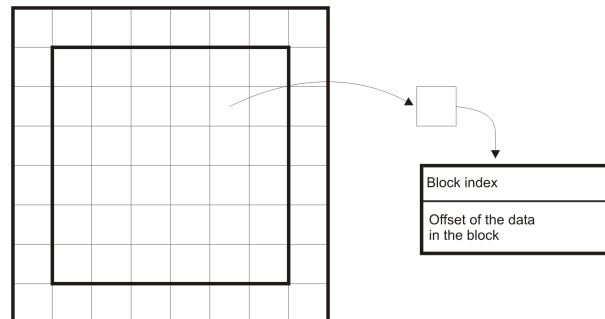
Figure 6.5: *Adjacency block, used as a look-up table for sequential movements in the volume. The adjacency block is one layer thicker than a data block. Every element of the adjacency block holds an index of block in 27-neighbour it points to and offset to corresponding position within a block. (2D case is shown for simplicity).*

responses even for large pCTA data (depending on required quality, sampling, size of data, etc.)

There are two limitation of the proposed solution that need to be considered: the first disadvantage is the limitation of the movements to only the 26-neighbourhood, i.e. maximum one unit-step in the direction of each coordinate axis. This property is a result of the one-voxel layer thickening of the adjacency block; but for our algorithms, limitation to 26-neighbourhood was not significant. The second limitation is the speed of writing operations; for every writing operation, it has to be tested whether the block is allocated or empty, and if empty then it have to be allocated. Therefore, the writing operations are slower — at the expense of optimized sequential access and compressed representation. Again, this was only a smaller limitation for our algorithms, because writing operations are needed only in the segmentation step.

6.4.2   Vessel Tree

The vessel tree is a the second most important data structure in pCTA processing. It holds both hierarchy and geometry of the vessel tree in the processing pipeline. The purpose of the vessel tree is to provide a simple access to structures representing the tree, as are e.g. individual segments, bifurcation points and their parameters and also to allow easy reconstruction of the vessel paths, for the purpose of e.g. CPR data resampling. Many possible solutions for vessel tree models exist; we proposed a model based on the oriented-graph concept. The vessel tree is represented as a set of edges (modeling the vessel segments) and vertices (corresponding to bifurcations). For each segment, orientation information, representing the blood flow direction, is available. In such oriented graph, begin- and end-points of each segment are therefore defined. Individual begin-points of segments can be end-points of other segments and vice versa.[3]

The vessel tree itself is then a list of edges (segments) and a list of vertices (control points). The control points store their position in the dataset and list of segments that start or end in it. The segments store information in which control point they begin and end, plus representation of the vessel course between these two points. To model the vessel course easily and effectively, we proposed to use a list of equidistantly sampled points. The information of the vessel course points is complemented with geometric information therein by storing radius of locally fitted circle model.

The hierarchical organization of the vessel tree allow traversing of the tree from the root to its endpoints and thus constituting a vessel path. (The concept of vessel path is described in Section 2.2). Automatic path generation is a prerequisite; both CPR and mpCPR images require this information.

6.5   Conclusion on Software Implementation

Within the previous sections, the main aspects of implementation of software aimed on pCTA data processing were summarized. As described, this is an complex task; its tediousness also depends on whether libraries (for user-interface, mathematic algorithms, visualization, data storage, etc.) with ready-made code are available. As individual algorithms often depend on data access paradigms and data structures are specific problem in pCTA (due to the volume size), often ready-made approaches cannot be used. Then, own libraries must be developed, reflecting the actual properties of the pCTA pipeline.

---

[3]For the PAOD pathology reasons it proved to be useful also to have vertices (control points), which are not real bifurcations but only create an artificial break within a segment. In processing these vertices are easily distinguishable, as only one segment is entering and only one segment is leaving these control points.

Diagnostics of the PAOD based on CPR visualization is still in its early days; the CT or MR scanner possession prerequisite still limits such diagnostic approach to become regular. Therefore, dedicated software modules for peripheral vascularity are still not common in most clinical workstations—what makes the proposed software special.

The described plugin architecture ensured flexibility of the system. This is important as certain extension are expected in the future; improvements of the algorithms discussed in the previous chapters are being suggested in the scientific community.

The most important experience from the implementation is the fact that expectations of users of the software are often very different compared to the ideas of the software developers. Communication of users' expectations is essential; it influences how the software is welcome in the clinical environment and influences overall application of developed algorithms in the clinical practice. As a conclusion, we advice to thoroughly discuss the users' expectations and possible technical solutions among the whole group of clinical and technical experts before and also during implementation of such software. The software developers should learn and understand important issues of diagnostic process; the clinical experts shall make certain effort to explain their expectations or requirements on the processing software in more explicit manner. We have recognized that often simpler, but more reliable manual techniques are more welcome among the medical experts, compared to a more complex and more sophisticated but slower and less reliable automatic algorithms. Efficiency of the processing and user satisfaction are as important as highly complex algorithms; for the clinicians, the computers and algorithms are just tools (i.e. 'the means') and not the subject of research (i.e. 'the objectives'). This has to be understood by the computer scientists; cooperation and understanding on both sides will then result in much better and more valuable results for all.

(a)

$\mathcal{C}$ points to itself

location with pointers to data,
points to actual block

location requiring additional
step to reflect
'over-border' access
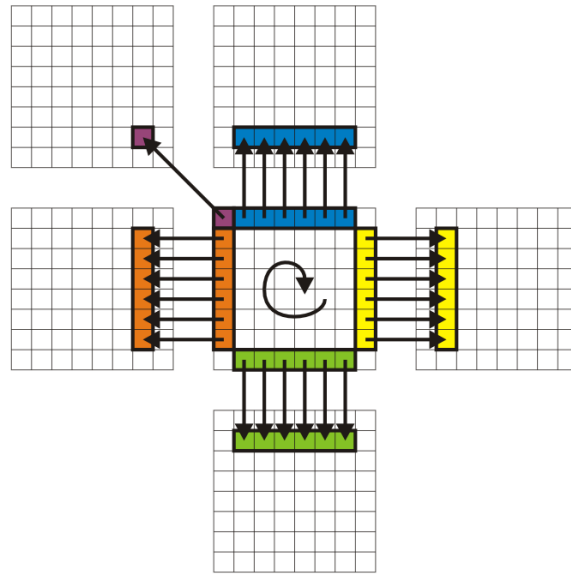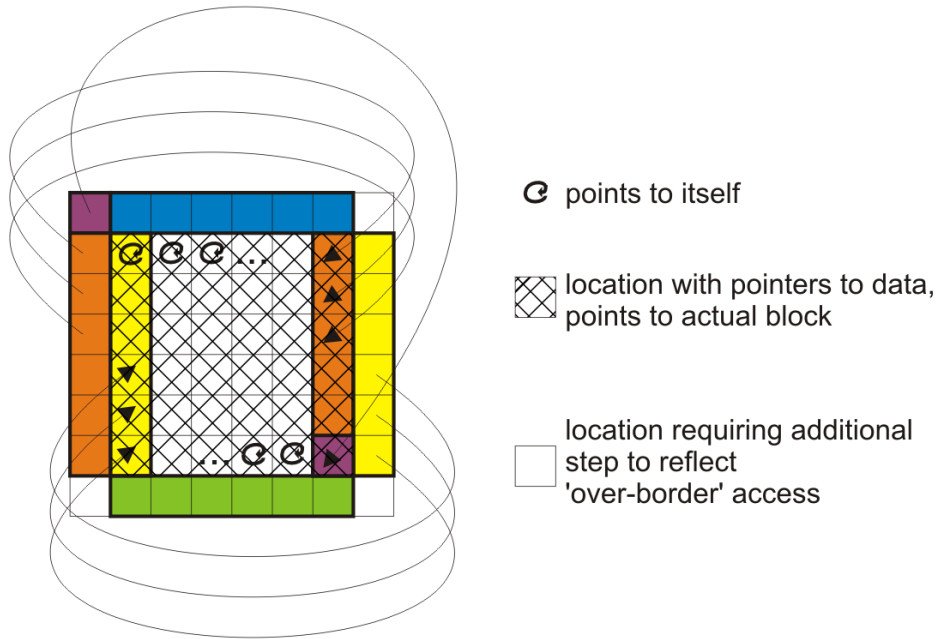
(b)

Figure 6.6: *Movement in the dataset with a block structure within 27-neighbour system. (a) For elements lying inside the block the mutual relation is straightforward, the pointers from adjacency blocks point to corresponding data locations. For elements accessed 'over the border' a shift to elements in other blocks is provided. (b) Move of the position within the adjacency block. For positions inside the block the shifted position is final, whereas for accesses 'over the border' additional shift to provide 'return from the other side' is needed. For further details, see text. (2D case is depicted for simplicity).*

Neighbourness Block

Original Block *j*

Neighbour Table

0	Pointer to self
1	Neighbour 1 pointer
2	Neighbour 2 pointer
3	Neighbour 3 pointer
4	
26	Neighbour 26 Pointer

**Data
(represented or
reference to empty
block)**

Stage 1

Neighbourness Block

Neighbour n_i

Offset in data
neighbour n_i

Get pointer to
neighbour n_i

Original Block *j*

Neighbour Table

0	Pointer to self
1	Neighbour 1 pointer
2	Neighbour 2 pointer
3	Neighbour 3 pointer
4	
26	Neighbour 26 Pointer

**Data
(represented or
reference to empty
block)**

Stage 2

Neighbourness Block

New Block *k*

Neighbour Table

0	Pointer to self
1	Neighbour 1 pointer
2	Neighbour 2 pointer
3	Neighbour 3 pointer
4	
26	Neighbour 26 Pointer

**Data
(represented or
reference to empty
block)**

Stage 3

Figure 6.7: *An example of a move in the 27-neighbour system. In the beginning, we expect to move over a block border. In the next stage, a move is executed in the adjacency block; index of a block and position offset therein is derived. In the last stage, the actual position depends on absolute address referenced by block index and on the derived offset. Position in the adjacency block is also correspondingly updated. For further details, see text. (For simplicity only 2D case is depicted.)*
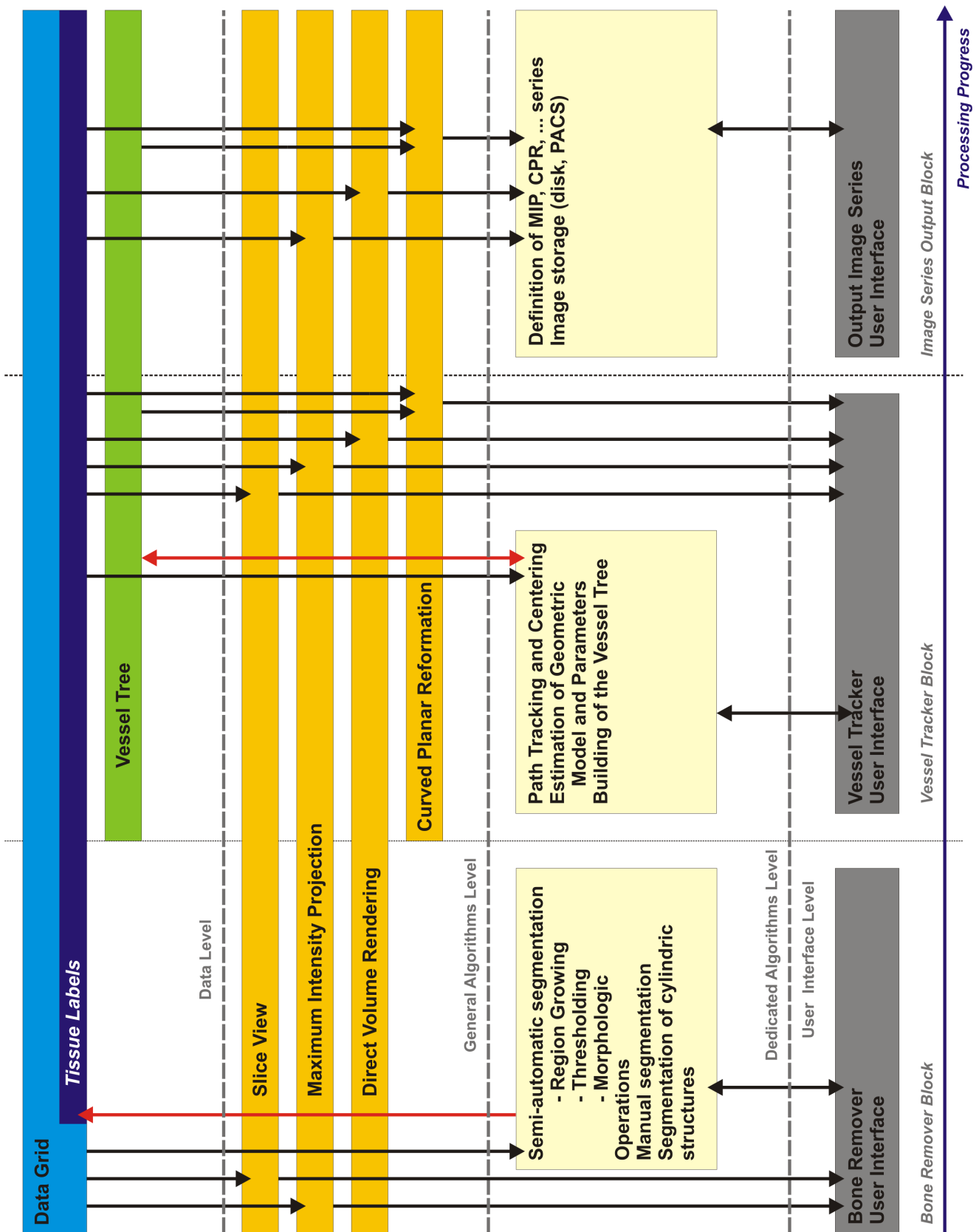
Figure 6.8: *Block scheme of a pCTA processing pipeline. The arrows depict which functionality is used in what blocks. The red arrows denote where actual data modifications take place. Viewing the image from left to right the process of processing pipeline can be seen, in relation to block scheme of the pCTA processing workflow on Fig. 6.1.*

Chapter 7

Conclusion

Within the previous chapters, we presented the results of a nearly four-year ongoing study on a field of processing and visualization of peripheral CT-Angiography datasets. We tried to address the particular challenges in the whole processing pipeline—the dataset segmentation, vessel tree reconstruction and visualization of the data. Further, we implemented the developed algorithms in a form of a medical workstation software, suitable for application in a clinical environment. Summarizing our research and work of other groups that appeared during the years, we conclude the following:

- According to evaluation of the output of the whole processing pipeline and positive acceptance of the algorithms in the clinical environment, we see our work as substantial and promising in the field of interventional radiology. The daily usage of our software for regular diagnostics only emphasizes this fact. In this light, we consider PAOD diagnostics based on CPR images as clinically relevant; for further application and routine usage of the proposed diagnostic technique in medical environment, a reliable and widely accepted implementation of the software solution is a prerequisite (e.g. by means of the proposed AngioVis ToolBox, within commercial packages, etc.) Nevertheless, we do not consider our work as completely finished; many problems remained open, among which the potential automation of those steps in the processing pipeline, which currently require operator intervention is most important,

- A precise segmentation of the pCTA dataset, mainly of the thin vessels, still remains a challenge. Significant improvements have been introduced by means of both operator-guided and automatic segmentation algorithms, but the results are not 100% correct or the required manual corrections are meticulous and therefore boring and lengthy. Partially, we assign these problems to shortcomings of the proposed segmentation algorithms, but we also consider the segmentation imperfection as a sampling problem; if the thin vessels would be better sampled, then e.g. model-based segmentation would delivered better results (being currently limited by the PVE). It can be expected that scanning resolution will change in next generation of scanners, with newly designed X-rays detectors. Certain segmentation problems might disappear in short time due to advent of announced dual-source scanners (e.g. Siemens SOMATOM Definition scanner), producing bi-modal data; nevertheless, the properties and features of such dual-source scanning have to be evaluated first. Such device was not available in our environment; according to our knowledge there are only two of them installed around the world so far. Regardless of the future, a modification of the proposed software system for such bi-modal data is simple and straightforward. In the meantime, CT-Angiography subtraction approaches are being tested, to circumvent the problem of bones occluding vessels in the image, as presented in work of Tomandl *et al.* [172] aimed on intracranial

CT-Angiography and based on preliminary version of Siemens Leonardo workstation; or as proposed in the work of Manniesing [173], where subtraction of CT scans with and without contrast agent were provided, also aimed on intracranial vessel analysis. Such approaches seem to work for structures with fixed shape, i.e. the skull and the brain. However, their application to pCTA is questionable and would require precise registration, which is still hard to achieve,

- In the field of vessel tree reconstruction we suggest further research in computerized recognition of the data, e.g. based on properties derived via model-based segmentation. In this setting, the algorithms will deliver much more information about objects' shape, size and location; further research will show whether such information is sufficient for automatic recognition of anatomic structures and for fitting of a particular vessel-tree template. Meanwhile, a library of predefined anatomic vessel-tree templates was suggested to support easier operator-driven reconstruction of the vessel tree. Properties that are automatically derived after manual location of the bifurcation points contribute to unsupervised determination of parameters (e.g. those of vessel-tracking algorithms), thus making tree reconstruction more reliable and more convenient to the user,

- As for visualization, a full implementation of the VesselGlyph concept by means of distance field or tissue labelling and direct volume rendering still remains a challenge. Much effort is invested in our environment for both CPU/software and GPU/hardware-accelerated approaches to achieve complete and efficient implementation. In between, the advent of dual-source scanner might contribute to the pCTA visualization in the future; special spectral properties of contrast agent versus calcification versus bone tissue shall lead to better enhancement of these structures in the derived images.

Appendix A

AngioVis ToolBox User Interface Snapshots
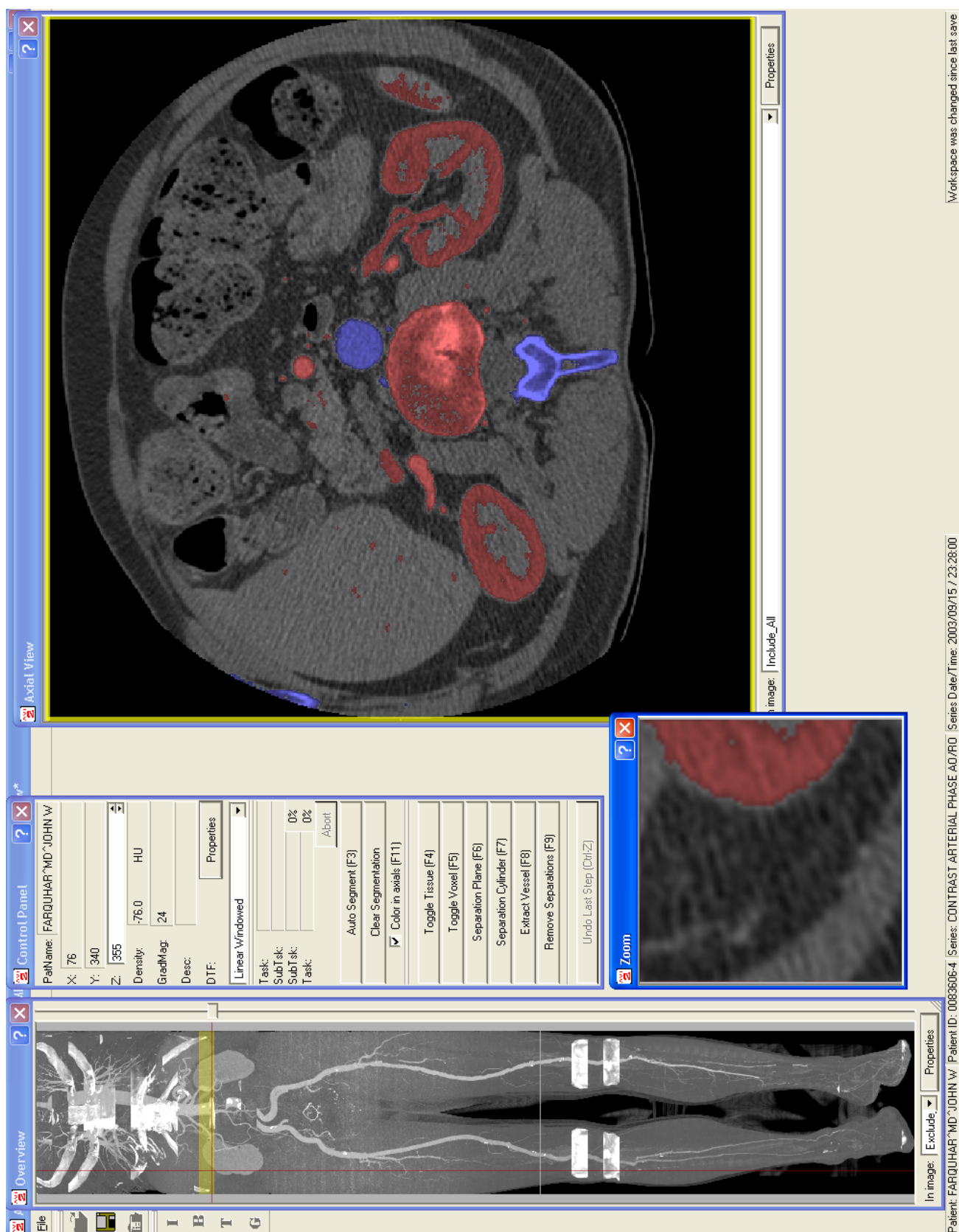
Figure A.1: *User-interface for manual bone editing in the AngioVis ToolBox. The dataset is first pre-segmented by automatic threshold-, gradient- and region growing-based technique and later the result is edited by a trained operator.*
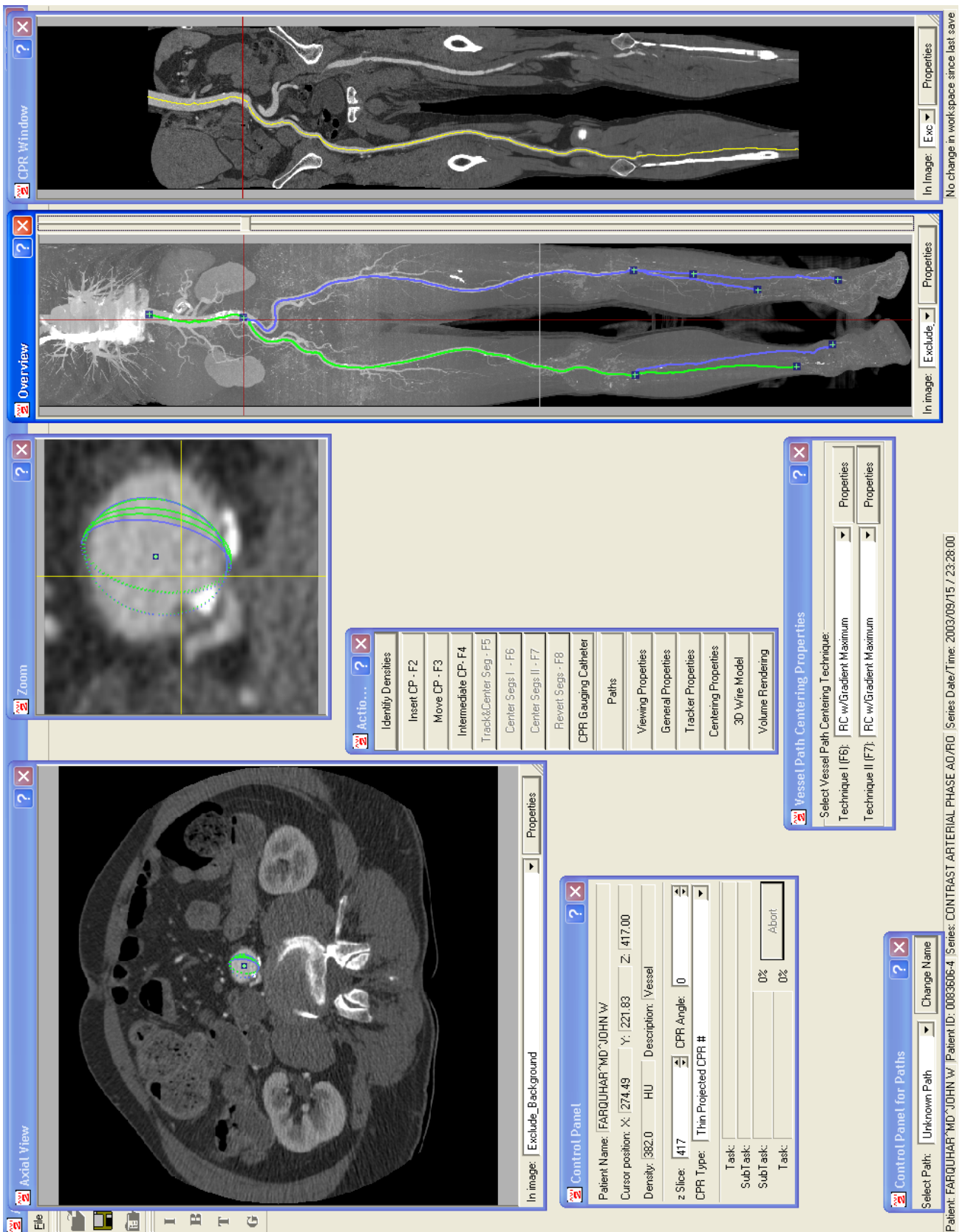
Figure A.2: *User-interface for vessel-tree reconstruction in the AngioVis ToolBox. For dataset with edited bones a hierarchical vessel tree is manually defined. The individual segments are then modelled by means of path-tracking and geometric model fitting techniques.*
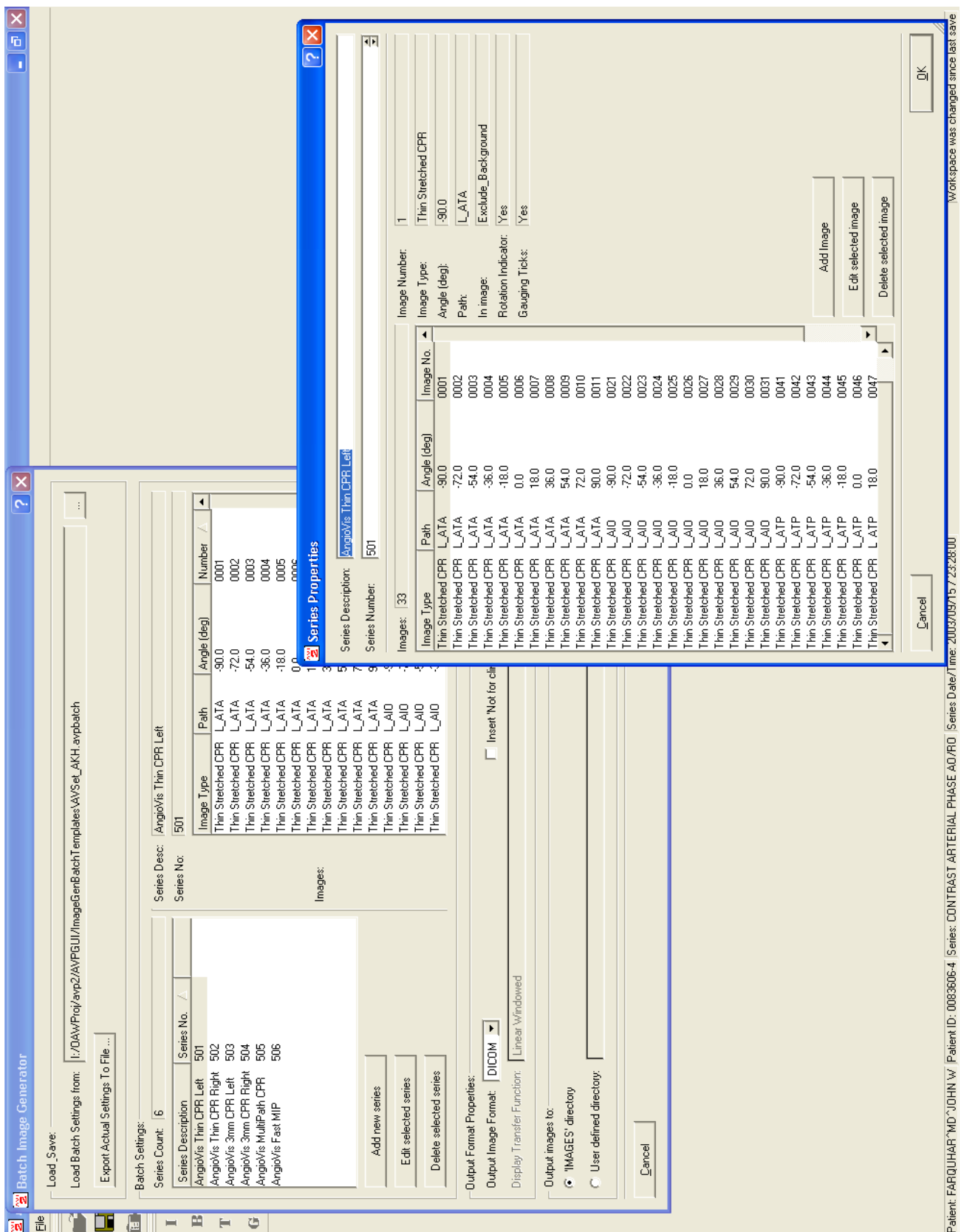
Figure A.3: *User-interface for image output in the AngioVis ToolBox. Images used for clinical PAOD diagnostic, showing the dataset from defined view-angles must be first generated and later organized in DICOM series. The Image Output functionality automates production and organization of defined image sets.*

Appendix B

Abbreviations

Abbreviation	Meaning
2D	two-dimensional
3D	three-dimensional, volumetric
AKH	Allgemeines Krankenhaus Wien (Vienna General Hospital)
ASM	Active shape model
ATA	Anterio-tibial artery
ATM-SVC	Adaptive, template moderated spatial varying classification (method)
CPR	Curved-planar reformation
CRT	Cathode-ray tube
CT	Computed tomography
CTA	CT-Angiography
DF	Distance field
DICOM	Digital Imaging and Communications in Medicine (standard)
DSA	Digital subtraction angiography
DT	Distance transform
DVR	Direct volume rendering
EM	Expectation-maximization
FEM	Finite-elements method
FOV	Field of view
FWF	Fonds zur Förderung der wissenschaftlichen Forschung (Austrian Science Fund)
GB	Gigabyte (1073741824 bytes)
HU	Hounsfield unit
ISEG	ISEG (segmentation software)
k-NN	k-nearest neighbours
kV	kilovolt
LCD	Liquid-crystal display

Abbreviation, Acronym	Meaning
mA	milliampere
MAP	Maximum-a-posterior (estimation)
MB	Megabyte (1048576 bytes)
MIP	Maximum-intensity projection
mL	milliliter
mpCPR	Multi-path curved-planar reformation
MR	Magnetic resonance
MRA	Magnetic resonance angiography
MRI	Magnetic resonance imaging
MRF	Markov random field
NMR	Nuclear magnetic resonance
PA	Peroneal artery
PACS	Picture Archiving and Communication System
PAOD	Peripheral Arterial Occlusive Disease
pCTA	Peripheral CT-Angiography
PDM	Point distribution model
PTA	Percutaneous transluminal angioplasty or posterio-tibial artery
PVE	Partial volume effect
RF	Radio-frequency
S&C	Segmentation and classification
TOF MRA	Time-of-flight MRA
TPS	Thin-plate spline
TRP	Transitional-research project
VE	Virtual endoscopy
VR	Volume rendering
WT	Watershed transform

Bibliography

[1] T. L. Stedman. *Stedman's medical dictionary*. Williams & Wilkins, Baltimore, USA, 1995.

[2] J. Někula, M. Heřman, J. Vomáčka, and M. Köcher. *Radiologie. Skriptum.* Univerzita Palackého, Olomouc, Czech Republic, 2001.

[3] N. M. Rofsky and M. A. Adelman. MR-angiography in the evaluation of atherosclerotic peripheral vascular disease. *Radiology*, 214:325–338, February 2000.

[4] W. C. Röntgen. Über eine neue Art von Strahlen. Technical report, Physikalisch-Medizinische Gesellschaft, Universität Würzburg, December 1895.

[5] H. L. Abrams. History of cardiac radiology. *American Journal of Roentgenology*, 167:431–438, August 1996.

[6] W. J. Morton. *The X ray or photography of the invisible and its value in surgery.* New York: American Technical Book Company, 1896.

[7] E. Haschek and O. Lindenthal. Contribution to the practical use of photography according to Röntgen. *Wien Chir Wochenschr*, 9:63, 1896.

[8] F. H. Williams. *The Roentgen rays in medicine and surgery as an aid in diagnosis and as therapeutic agent.* New York: MacMillan, 1903.

[9] F. Völcker and A. von Lichtenberg. Pyelographie (Röntgenographie des Nierenbeckens nach Kollargolfüllung). *Münchener Medizinische Wochenschrift*, 53:105–106, 1906.

[10] B. Brooks. Intra-arterial injection of sodium iodide. *The Journal of the American Medical Association*, 82:1016–1019, 1924.

[11] S. Radner. An attempt at the roentgenologic visualization of coronary blood vessels in man. *Acta Radiol*, 26:497–502, 1945.

[12] J. Mattson and M. Simon. *The Pioneers of NMR and Magnetic Resonance in Medicine: The Story of MRI.* Jericho & New York: Bar-Ilan University Press, 1996.

[13] P. M. Gruber, E. Hlawka, W. Nöbauer, and L. Schmetterer, editors. *Johann Radon. Gesammelte Abhandlungen*, volume 1. Österrreichsche Akademie der Wissenschaften, Wien, Österrreich, 1987.

[14] F. Natterer. *The Mathematics of Computerized Tomography*. John Wiley & Sons Ltd, 1986.

[15] A. Kanitsar, R. Wegenkittl, P. Felkel, D. Fleischmann, D. Sandner, and E. Gröller. Computed tomography angiography: A case study of peripheral vessel investigation. In *Proceedings of IEEE Visualization 2001*, pages 477–480, 2001.

[16] A. Kanitsar, D. Fleischmann, R. Wegenkittl, P. Felkel, and E. Gröller. CPR—Curved Planar Reformation. In *Proceedings of IEEE Visualization 2002*, 2002.

[17] I. N. Bankman, editor. *Handbook of Medical Imaging, Processing and Analysis*. Academic Press, 2000.

[18] R. C. Gonzales and R. Woods. *Digital Image Processing*. Addison Wesley, 1992.

[19] P. M. Weeks, M. W. Vannier, W. G. Stevens, G. Gayou, and L. A. Gilula. Three-dimensional imaging of the wrist. *Journal of Hand Surgery*, 10A (1):32–39, 1984.

[20] S.E. James, R. Richards, and D. A. McGrouther. Three-dimensional CT imaging of the wrist. *Journal of Hand Surgery*, 17B (5):504–506, 1992.

[21] A. Dempster, N. Liard, and D. Rubin. Maximum likehood from incomplete data via the EM algorithm. *Journal of Royal Statistical Society*, Series B 39:1–39, 1977.

[22] R.A. Redner and H. F. Walker. Mixture densities, maximum likelihood and the EM algorithm. *SIAM Review*, 26 (2):195–239, 1984.

[23] R.O. Duda and P.E. Hart. *Pattern Classification and Scene Analysis.* John Wiley & Sons, 1973.

[24] D. Cooper, H. Elliott, F. Cohen, L. Reiss, and P. Symosek. Stochastic boundary estimation and object recognition. *Computer Graphics and Image Processing*, 12:326–356, 1980.

[25] T. Schiemann, M. Bomans, U. Tiede, and K. H. Höhne. Interactive 3D segmentation. In *Proceedings of Visualization in Biomedical Computing*, 1992.

[26] M. Kass, A. Witkin, and D. Terzopoulos. Active contour models. *International Journal of Computer Vision*, 1 (4):321–331, 1988.

[27] L.D. Cohen and I. Cohen. Finite element methods for active contour models and balloons for 2D and 3D images. *IEEE Transactions on Pattern Analysis and Machine Intelligence*, 15 (11):1131–1147, 1993.

[28] V. Caselles, F. Catte, T. Coll, and F. Dibos. A geometric model for active contours. *Numerische Mathematik*, 66:1–31, 1993.

[29] R. Malladi, J. A. Sethian, and B. C. Vemuri. Evolutionary fronts for topology-independent shape modeling and recovery. In *Proceedings of European Conference on Computer Vision, Stockholm, Sweden*, pages 3–13, 1994.

[30] H. Tek and B. B. Kimia. Image segmentation by reaction-diffusion bubbles. In *International Conference on Computer Vision*, pages 156–162, 1995.

[31] T. McInerney and D. Terzopoulos. Topologically adaptive snakes. In *Proceedings of International Conference on Computer Vision, Cambridge, MA*, pages 840–855, 1995.

[32] T. McInerney, G. Hamarneh, M. Shenton, and D. Terzopoulos. Deformable organisms for automatic medical image analysis. *Medical Image Analysis*, 6 (3):251–266, 2002.

[33] V. Caselles, R. Kimmel, and G. Sapiro. Geodesic active contours. *International Journal of Computer Vision*, 22 (1):61–79, 1997.

[34] S. Kichenassamy, A. Kumar, P. Olver, A. Tannenbaum, and A. Yezzi. Gradient flow and geometric active contour models. In *Proceedings of the Fifth International Conference on Computer Vision, Cambridge, MA*, pages 810–815, 1995.

[35] W. J. Niessen, B. M. ter Haar Romeny, and M. A. Viergever. Geodesic deformable models for medical image analysis. *IEEE Transactions on Medical Imaging*, 17 (4):634 – 641, 1998.

[36] T. F. Cootes and C. J. Taylor. Active shape models - smart snakes. In *Proceedings British Machine Vision Conference*, pages 266 – 275, 1992.

[37] T. F. Cootes, C. J. Taylor, D. H. Cooper, and J. Graham. Active shape models - their training and application. *Comp. Vision Image Understanding*, 61:38 – 59, 1995.

[38] J. R. Beveridge, J. Griffith, R. R. Kohler, A. R. Hanson, and E. M. Riseman. Segmenting images using localized histograms and region merging. *International Journal of Computer Vision*, 2 (3):311–352, 1989.

[39] R. Adams and L. Bischof. Seeded region growing. *IEEE Transactions on Pattern Analysis and Machine Intelligence*, 16 (6):641–647, 1994.

[40] S. C. Zhu and A.L. Yuille. Region competition: unifying snakes, region growing, and Bayes/MDL for multiband image segmentation. *IEEE Transactions on Pattern Analysis and Machine Intelligence*, 18 (9):884–900, 1994.

[41] T.B. Sebastian, H. Tek, J. J. Crisco, and B. B. Kimia. Segmentation of carpal bones from CT images using skeletally coupled deformable models. *Medical Image Analysis*, 7 (1):21–45, 2003.

[42] M. A. Hurn, K. V. Mardia, T. J. Hainsworth, and E. Berry. Bayesian fused classification of medical images. *IEEE Transactions on Medical Imaging*, 15 (6):850 – 858, 1996.

[43] H. S. Choi, D. R. Haynor, and Y. Kim. Partial volume tissue classification of multichannel magnetic resonance images – a mixel model. *IEEE Transactions on Medical Imaging*, 10 (3):395 – 407, 1991.

[44] K. Held, E. Ruta Kops, B. J. Krause, W. M. Wells, R. Kikinis, and H. W. Muller-Gartner. Markov random field segmentation of brain MR images. *IEEE Transactions on Medical Imaging*, 16 (6):878–886, 1997.

[45] S. Geman and D. Geman. Stochastic relaxation, Gibbs distributions and the Bayesian restoration of images. *IEEE Transactions on Pattern Analysis and Machine Intelligence*, 6:721 – 741, 2003.

[46] H. Derin and W.S. Cole. Segmentation of textured images using Gibbs random fields. *Computer Vision, Graphics and Image Processing*, 35:72 – 98, 1986.

[47] S. Lakshmanan and H. Derin. Simultaneous parameter estimation and segmentation of Gibbs random fields using simulated annealing. *IEEE Transactions on Pattern Analysis and Machine Intelligence*, 11 (8):799 – 813, 1989.

[48] M.T. Chan, G. T. Herman, and L. Emanuel. A Bayesian approach to PET reconstruction using image-modeling Gibbs prior. *IEEE Transactions on Nuclear Science*, 44 (3), 1997.

[49] M. T. Chan, G. T. Herman, and L. Emanuel. *Bayesian Image Reconstruction Using Image-modeling Gibbs Prior*. Wiley, New York, 1998.

[50] T. Chen and D. Metaxas. A hybrid framework for 3D modeling image segmentation. *Medical Image Analysis*, 9 (6):547 – 565, 2005.

[51] L. Vincent and P. Soille. Watershed in digital spaces: an efficient algorithm based on immersion simulation. *IEEE Transactions on Pattern Analysis and Machine Intelligence*, 13 (6):583–598, 1991.

[52] V. Grau, A. U. J. Mewes, M. Alcaniz, R. Kikinis, and S. K. Warfield. Improved watershed transform for medical image segmentation using prior information. *IEEE Transactions on Medical Imaging*, 23 (4):447 – 458, 2004.

[53] I. Ahmad, A. Quddus, H.-J. Laine, and O. Yli-Harja. Image segmentation of the CT scans of hip endoprostheses. In *Proceedings of IEEE Nordic Signal Processing Symposium 2000 (NORSIG2000), Norrköping, Sweden*, page 271, 2000.

[54] M. Fiebich, Ch. M. Straus, V. Seghal, B. C. Renger, K. Doi, and K. R. Hoffman. Automatic bone segmentation technique for CT angiographic studies. *Journal of Computer Assisted Tomography*, 23(1), 1999.

[55] F. Y. Kwan, K. C. Cheung, and I. Gibson. Automatic extraction of bone boundaries from CT scans using an intelligence-based approach. In *Proceedings of International Conference on Pattern Recognition (ICPR 2000), Barcelona, Spain*, pages 3441–3444, 2000.

[56] Y. Kang, K. Engelke, and W. A. Kalender. A new accurate and precise 3-D segmentation method for skeletal structures in volumetric CT data. *IEEE Transactions on Medical Imaging*, 22 (5):586–598, 2003.

[57] W. Yao, P. Abolmaesumi, M. Greenspan, and R. E. Ellis. An estimation/correction algorithm for detecting bone edges in CT images. *IEEE Transactions on Medical Imaging*, 24 (8):997–1010, 2005.

[58] L. I. Wang, M. Greenspan, and R. Ellis. Validation of bone segmentation and improved 3D registration using contour coherency in CT data. *IEEE Transactions on Medical Imaging*, 25 (3):324–334, 2006.

[59] G. Behiels, F. Maes, D. Vanderneulen, and P. Suetens. Evaluation of image features and search strategies for segmentation of bone structures in radiographs using active shape models. *Medical Image Analysis*, 6 (2):47 – 62, 2002.

[60] J. G. Snel, H. W. Venema, and C. A. Grimbergen. Deformable triangular surface using fast 1-D radial Lagrangian dynamics - segmentation of 3D MR and CT images of the wrist. *IEEE Transactions on Medical Imaging*, 21 (8):888 – 903, 2002.

[61] M. Descoteaux, M. Audette, K. Chinzei, and K. Siddiqi. Bone enhancement filtering: Application to sinus bone segmentation and simulation of pituitary surgery. In *International Conference On Medical Image Computing and Computer Assisted Intervention (MICCAI 2005), Palm Springs, California)*, 2005.

[62] C. Kirbas and F. K. H. Quek. A review of vessel extraction techniques and algorithms. *ACM Comput. Surv.*, 36(2):81–121, 2004.

[63] G. Marchal, D. Vandermeulen, H. Bosmans, D. Delaere, P. Suetens, and A. Baert. A three dimensional line filter for improved visualization of MRA. *Radiology*, Supplement to number 177:259, 1990.

[64] G. Gerig, O. Kübler, R. Kikinis, and F. A. Jolesz. Nonlinear anisotropic filtering of MRI data. *IEEE Transactions on Medical Imaging*, 11:221 – 232, 1992.

[65] H. Chen and J. Hale. An algorithm for MR angiography image enhancement. *Magnetic Resonance in Medicine*, 33:534 – 540, 1995.

[66] Y. Du and D. Parker. Vessel enhancement filtering in three dimensional angiograms using long-range correlation. *Journal of Magnetic Resonance Imaging*, 7:447 – 450, 1997.

[67] M. Orkisz, C. Bresson, I. Magnin, O. Champin, and P. Douek. Improved vessel visualization in MR angiography by nonlinear anisotropic filtering. *Magnetic Resonance in Medicine*, 37:914 – 919, 1997.

[68] C. F. Westin, L. Wigström, T. Loock, L. Sjögvist, R. Kikinis, and H. Knutsson. Three-dimensional adaptive filtering in magnetic resonance angiography. *Journal of Magnetic Resonance Imaging*, 14:63 – 71, 2001.

[69] Y. Sun and D. Parker. Small vessel enhancement in MRA images using local maximum mean processing. *IEEE Transaction on Image Processing*, 10:1687 – 1699, 2001.

[70] G. Gerig, T. Koller, G. Székely, C. Brechbühler, and O. Kübler. Symbolic description of 3D structures applied to cerebral vessel tree obtained from MR angiography volume data. In *Information Processing in Medical Imaging – IPMI'93. Lecture notes in Computer Science*, volume 687, pages 94 – 111, 1993.

[71] C. J. Yan, S. Hirano, and Y. Hata. Extraction of blood vessels in CT angiography image aided by fuzzy logic. In *Proc. WCC Int. Conf. on Signal Processing (ICSP) 2000*, pages 926 – 929, 2000.

[72] Y. Kawata, N. Niki, and T. Kumazaki. Measurement of blood vessel characteristics for disease detection based on cone-beam CT images. *IEEE Transactions on Nuclear Science*, 43 (6):3348 – 3354, 1996.

[73] N. Passat, Ch. Ronse, J. Baruthio, J.-P. Armspach, and J. Foucher. Using watershed and multimodal data for vessel segmentation: Application to the superior sagittal sinus. In C. Ronse, L. Najman, and É. Decencière, editors, *Mathematical Morphology: 40 years on. Proceedings of the 7th International Symposium on Mathematical Morphology*, volume 30 of *Computational Imaging and Vision*, pages 419–428, Paris, France, April 18–20 2005. Springer SBM.

[74] S. Kobashi, Y. Hata, Y. Tokimoto, and M. Ishikawa. Automatic segmentation of blood vessels from MR angiogaphy volume data by using fuzzy logic technique. In *Medical Imaging: Image Processing 1999*, volume 3661, pages 968 – 976, 1999.

[75] P. Yim, P. Choyke, and R. Summers. Gray-scale skeletonization of small vessels in magentic resonance angiography. *IEEE Transactions on Medical Imaging*, 19:568 – 576, 2000.

[76] H. Cline, C. Dumoulin, W. Lorensen, S. Souza, and W. Adams. Volume rendering and connectivity algorithms for MR angiography. *Magnetic Resonance in Medicine*, 18:384 – 394, 1991.

[77] U. Klose, D. Petersen, and J. Martos. Tracking of cerebral vessels in MR angiography after high-pass filtering. *Journal of Magnetic Resonance Imaging*, 13:45 – 51, 1995.

[78] J. Beier, R. Siekmann, F. Muller, J. Stalke, G. Biamino, R. Felix, and E. Fleck. Three-dimensional reconstruction of implanted aortic stents usingcomputed tomography. In *Computers in Cardiology 1995*, pages 549 – 552, 1995.

[79] L. Lorigo, O. Faugeras, W. Grimson, R. Keriven, R. Kikinis, A. Nabavi, and C.-F. Westin. Curves: Curve evolution for vessel segmentation. *Medical Image Analysis*, 5 (3):195 – 206, 2001.

[80] A. Frangi, W. Niessen, R. Hoogeveen, T. van Walsum, and M. Viergever. Model-based quantitation of 3D magnetic resonance angiographic images. *IEEE Transactions on Medical Imaging*, 18 (10):946 – 956, 1999.

[81] M. Auer, R. Stollberger, P. Regitnig, F. Ebner, and G. A. Holzapfel. 3D reconstruction of tissue components for atherosclerotic human arteries using ex vivo high resolution MRI. *IEEE Transactions on Medical Imaging*, 25 (3):345 – 357, 2006.

[82] B. Verdonck, I. Bloch, H. Matre, D. Vandermeulen, P. Suetens, and G. Marchal. Accurate segmentation of blood vessels from 3D medical images. In P. Delogne, editor, *IEEE Int. Conf. Image Processing, September 1996*, volume 3, pages 311 – 314, 1996.

[83] A. Chung, J. Noble, and P. Summers. Fusing speed and phase information for vascular segmentation of phase contrast MR angiograms. *Medical Image Analysis*, 6 (2):109 – 128, 2002.

[84] D.L. Wilson and J. A. Noble. An adaptive segmentation algorithm for time of flight MRA data. *IEEE Transactions on Medical Imaging*, 18 (10):938 – 945, 1999.

[85] Sabry Hassouna M., A. Farag, S. Hushek, and T. Moriarty. Statistical-based approach for extracting 3D blood vessels from TOF-MRA data. In *Medical Image Computing and Computer-Assisted Intervention - MICCAI'03. Lecture Notes in Computer Science*, volume 2878, pages 680 – 687, 2003.

[86] J. C. Mazziotta, A. W. Toga, A. C. Evans, P. T. Fox, and J. L. Lancaster. A Probabilistic Atlas of the Human Brain: Theory and Rationale for Its Development. The International Consortium for Brain Mapping (ICBM). *NeuroImage*, 2(2a):89–101, June 1995.

[87] J. B. A. Maintz and M. A. Viergever. A survey of medical image registration. *Medical Image Analysis*, 2(1):1–36, 1998.

[88] A. Kelemen, G. Szekely, and G. Gerig. Elastic model-based segmentation of 3D neuoradiological data sets. *IEEE Transactions on Medical Imaging*, 18:828–839, 1999.

[89] D. MacDonald, N. Kabani, D. Avis, and A. C. Evans. Automated 3D extraction of inner and outer surfaces of cerebral cortex from MRI. *Neuroimage*, 12:340–356, 2000.

[90] A. Guimond, J. Meunier, and J. P. Thirion. Average brain models: a convergence study. *Computer Vision Image Understanding*, 77:192 – 210, 2000.

[91] G. Le Goualher, D. L. Collins, C. Barillot, and A. C. Evans. Automatic identification of cortical sulci using 3D probabilistic atlas. In *Proceedings of Medical Image Computing and Computer-Assisted Intervention (MICCAI 1998)*, volume 1496, pages 509 – 518, 1998.

[92] P. Thomson and A. W. Toga. Visualization and mapping of anatomic abnormalities using a probabilistic brain atlas based on random fluid transformations. *Visual. Biomed. Comput.*, 1131:383 – 392, 1996.

[93] A. W. Toga and P. M. Thomson. The role of image registration in brain mapping. *Image Vision Comput.*, 19:3 – 24, 2001.

[94] D. V. Iosifescu, M. E. Shenton, S. K. Warfield, R. Kikinis, J. Dengler, F. A. Jolesz, and R. W. McCarley. An Automated Registration Algorithm for Measuring MRI Subcortical Brain Structures. *NeuroImage*, 6:13–25, July 1997.

[95] R. Kikinis, M. E. Shenton, D. V. Iosifescu, R. W. McCarley, P. Saiviroonporn, H. H. Hokama, A. Robatino, D. Metcalf, C. G. Wible, Ch. M. Portas, R. M. Donnino, and F. A. Jolesz. A digital brain atlas for surgical planning, model-driven segmentation and teaching. *IEEE Transactions on Visualization and Computer Graphics*, 2(3):232–241, September 1996.

[96] L. M. Gao, D. G. Heath, and E. K. Fishman. Abdominal image segmentation using three-dimensional deformable models. *Invest. Radiol.*, 33:348 – 355, 1998.

[97] H. Park, P. H. Bland, and Ch. R. Meyer. Construction of an abdominal probabilistic atlas and its application in segmentation. *IEEE Transactions on Medical Imaging*, 22 (4):483–492, 2003.

[98] S. K. Warfield, M. Kaus, F. A. Jolesz, and R. Kikinis. Adaptive, Template Moderated, Spatially Varying Statistical Classification. *Medical Image Analysis*, 4(1), 2000.

[99] M. Straka, A. La Cruz, A. Köchl, L. I. Dimitrov, M. Šrámek, D. Fleischmann, and E. Gröller. Bone segmentation in CT-Angiography data using a probabilistic atlas. In *Proceedings of Vision, Modeling and Visualization 2003 Conference, Munich, Germany*, pages 505 – 512, 2003.

[100] G. Borgefors. Distance transformations in digital images. *Computer Vision, Graphics and Image Processing*, 34(3):344–371, 1986.

[101] M. E. Brummer, R. M. Mersereau, R. L. Eisner, and R. J. R. Lewine. Automatic detection of brain contours in MRI data sets. *IEEE Transactions on Medical Imaging*, 12(2):153–166, June 1993.

[102] X. Zeng, L. H. Staib, R. T. Schultz, and J. S. Duncan. Segmentation and measurement of the cortex from 3D MR using coupled surfaces propagation. *IEEE Trans. Med. Imaging*, 18(10), 1999.

[103] M. Šrámek. ISEG – A system for interactive segmentation of 3D tomographic data sets. In J. Rozman, editor, *Proc. of 12th international conference Biosignal '94*, pages 48–51, Czech Republic, 1994. Technical University Brno.

[104] M. W. Jones and R. Satherley. Shape representation using space filled sub-voxel distance fields. In *International Conference on Shape Modelling and Applications*, pages 316–325. IEEE Computer Society Press, 2001.

[105] F. L. Bookstein. Principal Warps: Thin-Plate Splines and the Decomposition of Deformations. *IEEE Transactions on Pattern Analysis and Machine Intelligence*, 11(6):576–585, June 1989.

[106] A.C. Evans, D.L. Collins, S.R. Mills, E.D. Brown, R.L. Kelly, and T.M. Peters. 3D statistical neuroanatomical models from 305 MRI volumes. In *Nuclear Science Symposium and Medical Imaging Conference*, volume 3 of *IEEE Conference Record*, pages 1813–1817, November 1993.

[107] F. Meyer. Topographic distance and watershed lines. *Signal Processing*, 38 (1):113–125, 1994.

[108] F. Meyer and S. Beucher. Morphological segmentation. *Journal of Visual Communication and Image Representation*, 1 (1):21–46, 1990.

[109] R. Lotufo and W. Silva. Minimal set of markers for the watershed transform. In *Proceedings of the ISMM2002*, 1992.

[110] S. Beucher. *Watersheds, Hierarchical Segmentation and Waterfall Algorithm*. Kluger Academic Publishers, Dordrecht, 1994.

[111] M. Šrámek and L. I. Dimitrov. Segmentation of tomographic data by hierarchical watershed transform. *Journal of Medical Informatics and Technologies*, 3:MI–161 – MI–169, 2002.

[112] M. Straka, A. Cruz, Köchl, M. Šrámek, D. Fleischmann, and E. Gröller. 3D watershed transform combined with a probabilistic atlas for medical image segmentation. In *Journal of Medical Informatics and Technologies, Szczyrk, Poland*, pages IT69 – IT78, 2003.

[113] Y. Sato, S. Nakajima, N. Shiraga, H. Atsumi, S. Yoshida, T. Koller, G. Gerig, and R. Kikinis. Three-dimensional multi-scale line filter for segmentation and visualization of curvilinear structures in medical images. *Med. Image Anal.*, 2 (2):143 –168, 1998.

[114] A. Frangi, W. Niessen, K. Vincken, and M. Viergever. Multiscale vessel enhancement filtering. In *MICCAI'98, volume 1496 of LNCS*, pages 130–137. Springer-Verlag, Germany, 1998.

[115] G. Krissian, M. Malandain, N. Ayache, R. Vaillant, and Y. Trousset. Model-based detection of tubular structures in 3D images. *Comput. Vis. Image Understand.*, 80 (2):130 – 171, 2000.

[116] C. Lorenz, I. C. Carlsen, T. M. Buzug ant C. Fassnacht, and J. Weese. A multi-scale line filter with automatic scale selection based on the hessian matrix for medical image segmentation. In *Proc. Scale-Space Theories in Computer Vision. Lect. Notes Comp. Sci. 1252*, pages 152 – 163, 1997.

[117] J. J. Koenderink. The structure of images. *Biol Cybern.*, 50:364–370, 1988.

[118] T. Lindeberg. *Scale-space Theory in Computer Vision*. Kluwer Academic Publishers, Dordrecht, Netherlands, 1994.

[119] T. Lindeberg. Edge detection and ridge detection with automatic scale selection. In *IEEE Computer Society Conference on Computer Vision and Pattern Recognition (CVPR '96), San Francisco*, page 465, 1996.

[120] H. Knutsson. Representing local structure using tensors. In *The 6th Scandinavian Conference on Image Analysis*, page 244251, 1989.

[121] J. Hladůvka. *Derivatives and Eigensystems for Volume-Data Analysis and Visualization*. PhD thesis, Technische Universität Wien, Institut für Computergraphik und Algorithmen, 2001.

[122] K. Bühler, P. Felkel, and A. La Cruz. Geometric methods for vessel visualization and quantification - a survey. In G. Brunnet, B. Hamann, and H. Müller (eds.), editors, *Geometric Modelling for Scientific Visualization*, pages 399 – 420. Kluwer Academic Publishers, 1994.

[123] D. Selle, B. Preim, A. Schenk, and H.-O. Peitgen. Analysis of vasculature for liver surgical planning. *IEEE Transactions on Medical Imaging*, 21 (11):1344 – 1357, 2002.

[124] I. Bitter, A. E. Kaufman, and M. Sato. Penalized-distance volumetric skeleton algorithm. *IEEE Transactions on Visualization and Computer Graphics*, 7(3):195–206, 2001.

[125] S. Bouix, K. Siddiqi, and A. Tannenbaum. Flux driven automatic centerline extraction. *Medical Image Processing*, 9 (3):209 – 221, 2005.

[126] J. D. Furst, S. M. Pizer, and D. Eberly. Marching cores: a method for extracting cores from 3D medical images. In *Proc. Workshop on Math. Methods in Biomed. Image Anal.*, pages 124 – 130, 1996.

[127] J. D. Furst and S. M. Pizer. Marching optimal-parameter ridges: an algorithm to extract shape loci in 3D images. Technical Report TR-98-006. Technical report, University of North Carolina, December 1998.

[128] S. Aylward and E. Bullitt. Initialization, noise, singularities and scale in height ridge traversal for tubular object centerline extraction. *IEEE Transactions on Medical Imaging*, 21 (2):61 – 75, 2002.

[129] E. Sorantin, C. Halmai, B. Erdohelyi, K. Palagyi, L. Nyul, K. Olle, B. Geiger, F. Lindbichler, G. Friedrich, and K. Kiesler. Spiral-CT-based assesment of tracheal stenoses using 3D skeletonization. *IEEE Transactions on Medical Imaging*, 21 (3):263 – 273, 2002.

[130] N. Passat, C. Ronse, J. Baruthio, J. P. Armspach, and C. Maillot. Magnetic resonance angiography: From anatomical know modeling to vessel segmentation. *Medical Image Analysis*, 10 (2):259 – 274, 2006.

[131] Y. Fridman, S. Pizer, S. Aylward, and E. Bullitt. Extracting branching tubular structures via cores. *Medical Image Analysis*, 8:169 – 176, 2004.

[132] N. Flasque, M. Desvignes, J.-M. Constans, and M. Revenu. Acquisition, segmentation and tracking of the cerebral vascular tree on 3D magnetic resonance angiography images. *Medical Image Analysis*, 5 (3):173 – 183, 2001.

[133] T. Deschamps and L. D. Cohen. Fast extraction of minimal paths in 3D images and applications to virtual endoscopy. *Medical Image Processing*, 5 (4):281 – 299, 2001.

[134] O. Wink, W.J. Niessen, and M.A. Viergever. Fast delination and visualization of vessels in 3D angiographic images. *IEEE Transactions on Medical Imaging*, 19 (4):337 – 346, 2000.

[135] A. La Cruz, M. Straka, A. Köchl, M. Šrámek, E. Gröller, and D. Fleischmann. Non-linear model fitting to parametrize diseased blood vessels. In *Proceedings of the IEEE Visualization 2004 Conference, Austin, Texas*, pages 393 – 400, 2004.

[136] P. Yan and A. A. Kassim. MRA image segmentation with capillary active contour. In *MICCAI*, pages 51–58, 2005.

[137] I. Volkau, W. Zheng, R. Baimouratov, A. Aziz, and W. L. Nowinski. Geometric modelling of the human normal cerebral arterial system. *IEEE Transactions on Medical Imaging*, 24 (4):529 – 539, 2005.

[138] G. Agam, S. G.Armato, and Ch. Wu. Vessel tree reconstruction in thoracic CT scans with application to nodule detection. *IEEE Transactions on Medical Imaging*, 24 (4):486 – 499, 2005.

[139] F. Zana and J. C. Klein. A multimodal registration algorithm of eye fundus images using vessel detection and Hough transform. *IEEE Transactions on Medical Imaging*, 24 (4):529 – 539, 2005.

[140] E. Bullitt, K. E. Muller, I. Jung, W. Lin, and S. Aylward. Analyzing attributes of vessel populations. *Medical Image Processing*, 9 (1):39 – 49, 2005.

[141] E. Bullitt, S. R. Aylward, K. Smith, S. Mukherji, M. Jiroutek, and K. Muller. Symbolic description of intracerebral vessels segmented from mra and evaluation by comparison with X-rays angiograms. *Medical Image Processing*, 5:157 – 169, 2001.

[142] C. Chalopin, G. Finet, and I. E. Magnin. Modeling the 3D coronary tree for labeling purposes. *Medical Image Processing*, 5 (4):301 – 315, 2001.

[143] L. Antiga and D. A. Steinman. Robust and objective decomposition and mapping of bifurcating vessels. *IEEE Transactions on Medical Imaging*, 23 (6):704 – 713, 2004.

[144] A. X. Falcão, J. K. Udupa, and F. K. Miyazawa. An ultra-fast user-steered image segmentation paradigm: Live-wire-on-the-fly. *IEEE Transactions on Medical Imaging*, 19 (1):55–62, 2000.

[145] A. La Cruz. *3D Modelling and Reconstruction of Peripheral Vascular Structure*. PhD thesis, Technische Universität Wien, Institut für Computergraphik und Algorithmen, 2006.

[146] M. de Bruijne, W. J. Niessen, J. B. A. Maintz, and A. M. Viergever. Localization and segmentation of aortic endografts using marker detection. *IEEE Transactions on Medical Imaging*, 22 (4):473 – 482, 2003.

[147] T. Behrens, K. Rohr, and H. S. Stiehl. Using an extended Hough transform combined with a Kalman filter to segment tubular structures in 3D medical images. In *VMV '01: Proceedings of the Vision Modeling and Visualization Conference 2001*, pages 491–498, 2001.

[148] T. Rakshe, J. Roos, M. Straka, S. Napel, and D. Fleischmann. Eigenshape based estimation of missing data from 3D curves: Application to vascular centerline restoration in CT angiography of femoropopliteal artery occlusions. In *Proceedings of the European Congress of Radiology (ECR) '06, Vienna, Austria*, 2006.

[149] S. Rossnick, G. Laub, and R. Bräckle. Three dimensional display of blood vessels in MRI. In *Proceedings of the IEEE Computers in Cardiology Conference*, pages 193–196, 1986.

[150] S. Napel, M.P. Marks, G.D. Rubin, M.D. Dake, C.H. McDonell, S.M. Song, D.R. Enzmann, and R.B. Jeffrey. Ct angiography wth spiral ct and maximum intensity projection. *Radiology*, 185:607–610, 1992.

[151] M. Levoy. Display of surfaces from volume data. *IEEE Computer Graphics & Applications*, 8 (5):29–37, 1988.

[152] R. A. Drebin, L. Carpenter, and P. Hanrahan. Volume rendering. In *Proceedings of SIGGRAPH '88*, pages 65–74, 1988.

[153] Dominik Fleischmann, Richard L. Hallett, , and Geoffrey D. Rubin. CT-Angiography of Peripheral Arterial Disease. *Journal of Vascular Interventional Radiology*, 17:3–26, 2006.

[154] I. Bitter, M. Sato, and M. A. Bender. Automatic, accurate and robust colon centerline algorithm. *Radiology*, 2000:217, 2000.

[155] D. Chen, Z. Liang, M. R. Wax, L. Li, B. Li, and A. E. Kaufman. A novel approach to extract colon lumen from CT images for virtual colonoscopy. *IEEE Transaction on Medical Imaging*, 19:1220–1226, 2000.

[156] L. Hong, A. Kaufman, Y. Wei, A. Viswambharn, M. Wax, and Z. Liang. 3D Virtual Colonoscopy. In *Proceedings of Symposium on Biomedical Visualization 1995*, pages 26–32, 1995.

[157] M. Wan, Q. Tang, A. E. Kaufman, Z. Liang, and M. Wax. Volume rendering based interactive navigation within the human colon. In *Proceedings IEEE Visualization*, pages 397–400, 1999.

[158] H. Hauser, L. Mroz, G.-I. Bischi, and E. Gröller. Two-level rendering. In *Journal IEEE Transactions on Computer Graphics and Visualization (IEEE TVCG)*, pages 242–252, 2001.

[159] J. Zhou, M. Hinz, and K. D. Tönnies. Hybrid-focal region based rendering of medical data. In *Bildverarbeitung für die Medizin 2002, Leipzig*, pages 113–116, 2002.

[160] I. Viola, A. Kanitsar, and E. Gröller. Importance-driven volume rendering. In *Proceedings of the IEEE Visualization 2004 Conference, Austin, Texas*, pages 139 – 145, 2004.

[161] S. Card, J. Mackinlay, and B. Shneiderman. *Readings in Information Visualization: Using Vision to Think*. Morgan Kaufmann Publishers, 1999.

[162] I. Viola. *Importance-Driven Expressive Visualization*. PhD thesis, Technische Universität Wien, Institut für Computergraphik und Algorithmen, 2005.

[163] C. Rezk-Salama, K. Engel, M. Bauer, G. Greiner, and T. Ertl. Interactive volume rendering on standard PC graphics hardware using multi-textures and multi-stage rasterization. In *Proc. Eurographics/SIGGRAPH Workshop on Graphics Hardware 2000 (HWWS00)*, 2000.

[164] B. Cabral, N. Cam, and J. Foran. Accelerated volume rendering and tomographic re-construction using texture mapping hardware. In *Proc. of IEEE Symposium on Volume Visualization*, pages 91 – 98, 1994.

[165] D. Fleischmann, M. Straka, M. Šrámek, A. La Cruz, A. Köchl, A. Kanitsar, T. Rakshe, S. Napel, J. Lammer, and E. Gröller. Angiovis: computer graphics for clinical visualization of peripheral arterial occlusive disease. In *Europ Radiol 15*, pages 574 – 575, 2005.

[166] B. Stroustrop. *The C++ programming language*. Addison-Wesley, 1986.

[167] Offis, Oldenburg, Germany. Dcmtk-the dicom toolkit, ver. 3.5.4. `http://dicom.offis.de`, 2005.

[168] N. Wirth. *Algorithms and data structures*. Prentice-Hall, 1985.

[169] S. Grimm. *Real-Time Mono- and Multi-Volume Rendering of Large Medical Datasets on Standard PC Hardware*. PhD thesis, Technische Universität Wien, Institut für Computergraphik und Algorithmen, 2005.

[170] S. Grimm, S. Bruckner, A. Kanitsar, and E. Gröller. A refined data addressing and processing scheme to accelerate volume raycasting. *Computers & Graphics*, 28(5):719 – 729, 2004.

[171] S. Grimm, S. Bruckner, A. Kanitsar, and E. Gröller. Memory efficient acceleration structures and techniques for CPU-based volume raycasting of large data. In *IEEE/SIGGRAPH Symposium on Volume Visualization and Graphics*, pages 1 – 8, 2004.

[172] B.F. Tomandl, T. Hammen, E. Klotz, H. Ditt, B. Stemper, and M. Lell. Bone-Subtraction CT Angiography for the Evaluation of Intracranial Aneurysms. *American Journal of Neuroradiology*, 27:55–59, 2006.

[173] R. Manniesing, B. K. Velthuis, M. S. van Leeuwen, I. C. van der Schaaf, P. J. van Laar, and W. J. Niessen. Level set based cerebral vasculature segmentation and diameter quantification in CT Angiography. *Medical Image Processing*, 10 (2):200 – 214, 2006.

Appendix C

Curriculum Vitae

Dipl.-Ing. Matúš Straka
born on the 18th of March, 1978 in Bratislava, Slovakia

Education

Feb 2003–	Ph.D. student in Computer Science, Vienna University Of Technology, Austria
2002	**Diploma in Automation (Dipl.-Ing.)**, Slovak University of Technology, Bratislava, Slovakia
2000	**Diploma in Automation (Bc.)**, Slovak University of Technology, Bratislava, Slovakia
1996–2002	Study in field of control, automation and robotics, Slovak University of Technology, Bratislava, Slovakia
1992–1996	Gymnasium Jura Hronca, Novohradska, Bratislava, Slovakia
1984–1992	Elementary schools, Bratislava, Slovakia

Profesional Experience

Sep 2004–Aug 2006	Scientific co-worker, Austrian Academy of Sciences, Commission for Scientific Visualization, Vienna, Austria
Jun 2004–Aug 2004	Research Assistant, Medical University of Vienna, Vienna, Austria
May 2002–May 2004	Scientific co-worker, Austrian Academy of Sciences, Commission for Scientific Visualization, Vienna, Austria
Jun 2000–Apr 2002	Design Engineer/Analyst at Taureus Ltd., Bratislava, Slovakia

Scientific and educational activities within recent years:

- Programming of the medical data processing software (AngioVis ToolBox)
- Research in field of medical data processing
- Supervision of students' masterthesis and praktikum

Awards

2006   **Hounsfield Award**, in Scientific Session of Society of Computed Body
            Tomography and Magnetic Resonance (SCBT/MR) 2006 April 02, 2006,
            Phoenix, Az. Knowledge-based Algorithm for Automated Centerline Inter-
            polation through Femoro-Popliteal Occlusions in Peripheral CT Angiography
            (CTA). *(J. E. Roos, D. Fleischmann, T. Rakshe, M. Straka, J. Rosenberg, M.
            Sofilos, D. Tran, S. Napel.)*

2005 3rd place **EUROGRAPHICS 2005 Medical Prize**, EUROGRAPHICS 2005
            Conference, Dublin, Ireland for **The AngioVis ToolBox** *(M. Straka, M. Šrá
            mek, A. La Cruz, E. Gröller, A. Köchl and D. Fleischmann)*

Publications

D. Fleischmann, M. Straka, M. Šrámek, A. La Cruz, A. Köchl, A. Kanitsar, T. Rakshe, S. Napel, J. Lammer, E. Gröller. **AngioVis: computer graphics for clinical visualization of peripheral arterial occlusive disease.** Europ Radiol 15 (2005), Suppl 1, 574-575

M. Straka, M. Červeňanský, A. La Cruz, A. Köchl, M. Šrámek, E. Gröller, D. Fleischmann. **The VesselGlyph Focus and Context Visualization in CT-Angiography.** In Proceedings of the IEEE Visualization 2004 Conference, Austin, Texas, 2004, p. 385-392

M. Straka, A. La Cruz, A. Köchl, L. I. Dimitrov, M. Šrámek, D. Fleischmann, E. Gröller. **Bone Segmentation in CT-Angiography Data Using a Probabilistic Atlas.** In Proceedings of Vision, Modeling and Visualization 2003 Conference, Munich, Germany 2003, p. 505-512

M. Straka, A. Cruz, A. Köchl, M. Šrámek, D. Fleischmann, E. Gröller. **3D Watershed Transform Combined With a Probabilistic Atlas For Medical Image Segmentation.** In Journal of Medical Informatics and Technologies, Szczyrk, Poland, 2003, p. IT69-IT78

T. Rakshe, J. Roos, M. Straka, S. Napel, D. Fleischmann. **Eigenshape based estimation of missing data from 3D curves: Application to vascular centerline restoration in CT angiography of femoropopliteal artery occlusions.** European Congress of Radiology, March 2006

T. Rakshe, D. Fleischmann, S. Napel, A. Pezeshkmehr, M. Straka. **Medial axis estimation of occluded peripheral arterial tree segments using a knowledge-based approach.** Biomedical Computation at Stanford, October 2004

Document version: Monday 24$^{\text{th}}$ July, 2006, 13:23